

**BEAMFORMING TECHNIQUES FOR USER
CAPACITY IMPROVEMENTS OF IS-95
CELLULAR CDMA SYSTEMS**

by

CHAN, LESTER KWOK-HUNG

B.A.Sc., The University of British Columbia, 1997

A THESIS SUBMITTED IN PARTIAL FULFILLMENT OF

THE REQUIREMENTS FOR THE DEGREE OF

MASTER OF APPLIED SCIENCE

in

THE FACULTY OF GRADUATE STUDIES

DEPARTMENT OF ELECTRICAL AND COMPUTER ENGINEERING

We accept this thesis as conforming

to the required standard

THE UNIVERSITY OF BRITISH COLUMBIA

June 2002

© Chan, Lester Kwok-Hung, 2002

In presenting this thesis in partial fulfilment of the requirements for an advanced degree at the University of British Columbia, I agree that the Library shall make it freely available for reference and study. I further agree that permission for extensive copying of this thesis for scholarly purposes may be granted by the head of my department or by his or her representatives. It is understood that copying or publication of this thesis for financial gain shall not be allowed without my written permission.

Department of Electrical & Computer Engineering

The University of British Columbia
Vancouver, Canada

Date June 12, 2002

Abstract

In this thesis, the use of adaptive beamforming antennas for enhancing the system capacity of IS-95 Code Division Multiple Access (CDMA) digital cellular systems is investigated. Adaptive beamforming is a Spatial Division Multiple Access (SDMA) technology which can be used to reduce interference in the spatial dimension. By using beamforming antennas, the signals can be transmitted and received in selective directions, giving rise to significantly reduced interference and therefore improved system capacities.

In order to estimate the capacity improvements that can be achieved, several antenna models including the omnidirectional, 3-sectored antennas and multi-element (4, 6 and 8) beamforming arrays are considered in this thesis. Furthermore, the extended Hashemi multipath model is modified explicitly for the IS-95 systems by generating multipath signals which are separated by one chip period and therefore readily resolvable by the IS-95 RAKE receivers.

A detailed IS-95 system was considered, and a bit error rate (BER) performance model was developed. In this BER model, the performance of the multipath combining RAKE receiver is investigated for the considered multipath Rayleigh fading environment by employing coherent and non-coherent maximum ratio combining for the downlink and the uplink, respectively. An important feature of the proposed model is that it ensures for each mobile communication link an average BER of 10^{-3} is maintained. This implies that, each receiver, based upon its multipath power distributions, can experience a different signal-to-interference ratio (SIR) per bit threshold.

Based upon these models, a sophisticated and very generic capacity simulation software platform was developed as an effective approach to accurately simulate the IS-95 system capaci-

ties under realistic system conditions, including more practical channel models. In this simulation platform, a 3-tier hexagonal cell structure with 19 cells is considered and the mobile users are assumed to be uniformly distributed across the 19-cell region. User voice activity and imperfect power control are modelled according to their individual statistical properties. In order to accurately simulate the capacities of the IS-95 systems, each user was introduced on an individual basis, until system saturation condition occurred during the capacity simulations. Based upon the numerous computer simulated performance evaluation results obtained, the advantages of using adaptive beamforming antennas, as compared to conventional antennas, are presented in terms of IS-95 system capacity improvements. These performance results have shown that using adaptive beamforming antennas can significantly improve the capacities of the IS-95 systems as compared to conventional antennas. In addition, the simulation results have also shown that the capacities of the IS-95 systems are heavily dependent upon the signal propagation loss index, power control performance and the urbanization characteristics of the geographical area.

Table of Contents

Abstract	ii
List of Tables	viii
List of Figures	ix
List of Abbreviations	xi
List of Symbols	xiii
Acknowledgements	xvii
Chapter 1 INTRODUCTION	1
Chapter 2 ANTENNA MODELS	6
2.1 Introduction.....	6
2.2 Omnidirectional Antenna.....	7
2.3 Directional Sectored Antenna.....	7
2.3.1 Ideal 3-Sectored Antenna.....	9
2.3.2 Cardioid 3-Sectored Antenna.....	9
2.4 Adaptive Beamforming Antenna Array.....	11
2.5 Antenna Interference Suppression Performance.....	18
2.6 Conclusions.....	20
Chapter 3 IS-95 MULTIPATH CHANNEL MODEL	21
3.1 Introduction.....	21
3.2 Large-Scale Fading Model.....	22
3.2.1 Propagation Loss.....	23
3.2.2 Shadowing Loss.....	23
3.3 Small-Scale Fading Model.....	25

3.3.1	Small-Scale Fading: Parameters and Characterization	25
3.3.2	Small-Scale Fading: Statistical Distribution Model	27
3.4	IS-95 Multipath Power Profile and Signal Scattering	28
3.4.1	Hashemi Multipath Channel Model (HMCM)	29
3.4.2	Geometrically Based Circular Model (GBCM).....	36
3.4.3	Extended IS-95 CDMA Multipath Channel Model (CMCM).....	39
3.5	Conclusions.....	46
Chapter 4	IS-95 BER PERFORMANCE MODEL	48
4.1	Introduction.....	48
4.2	Direct Sequence CDMA	49
4.3	IS-95 Signal Waveform Design	51
4.3.1	IS-95 Downlink Channel Structure.....	52
4.3.2	IS-95 Uplink Channel Structure	56
4.4	IS-95 Multipath-Combining Receiver Structure.....	59
4.4.1	RAKE Receiver Structure.....	59
4.4.2	IS-95 Receiver Structure with RAKE Combiner.....	62
4.5	The IS-95 BER Performance Model.....	64
4.5.1	Viterbi Decoder Performance	64
4.5.2	BER Performance for the One-Path Unfaded AWGN Channel	65
4.5.3	BER Performance for the Multipath Rayleigh Faded Channel	68
4.6	Conclusions.....	71
Chapter 5	IS-95 CAPACITY SIMULATION: SYSTEM MODEL, PARAMETERS AND METHODOLOGY	73
5.1	Introduction.....	73

5.2	Multi-Cell Configuration Model.....	73
5.3	Power Control and Voice Suppression.....	75
5.4	Gaussian Approximation for Interference	78
5.5	Single-Path and Multi-path Simulations.....	79
5.6	Simulation Methodology	80
5.6.1	Pre-estimation Parameter Generation	81
5.6.2	System Capacity Simulation	84
5.7	Conclusions.....	89
Chapter 6	IS-95 CAPACITY SIMULATION RESULTS	90
6.1	Introduction.....	90
6.2	Simulation Parameters	91
6.3	Single-Path Simulation Results	91
6.4	Multi-path Simulation Results	97
6.5	Comparisons With Other Publications.....	103
6.6	Conclusions.....	105
Chapter 7	CONCLUSIONS AND FUTURE RESEARCH	106
7.1	Conclusions.....	106
7.1.1	IS-95 CDMA Multipath Model	106
7.1.2	IS-95 BER Performance Model	107
7.1.3	Generic IS-95 Capacity Simulator.....	107
7.2	Suggestions for Future Research	108
7.2.1	Beamforming Adaptivity in AWGN Environments	108
7.2.2	Adaptive Null-Steering Antennas	108

7.2.3	Improved IS-95 Capacity Simulator	109
7.2.4	CDMA2000 Capacity Simulator	109
	Bibliography	111
	Appendix A. Sample Power Profiles for the Four Simulated Areas	116
	Appendix B. SIR Per Bit Thresholds for the Simulated Power Profiles	121

List of Tables

Table 2.1	Antenna Directivity for the Simulated Antenna Patterns	19
Table 3.1	Path Loss Exponents for the Simulated Areas	23
Table 3.2	Typical Delay Spread Values	25
Table 3.3	Sample Power Profiles For Downtown San Francisco	45
Table 3.4	Sample Power Profiles For Residential Berkeley	46
Table 4.5	Sample IS-95 Downlink and Uplink SIR Thresholds.....	70
Table 6.1	System Parameter Values Assumed in Capacity Simulations	91
Table 6.2	Single-Path Simulation Result Statistics (Users/Cell)	94
Table 6.3	Multi-path Simulation Result Statistics for Downtown Oakland (Users/Cell).....	99
Table 6.4	Multi-path Simulation Result Statistics for the Four Areas (Users/Cell)	102

List of Figures

Fig. 2.1	Omnidirectional Antenna Pattern	8
Fig. 2.2	Ideal 3-Sectored Antenna Pattern	8
Fig. 2.3	Cardioid 3-Sectored Antenna Pattern	10
Fig. 2.4	Wavefronts Impinging Upon a Beamforming Array	12
Fig. 2.5	Illustration of Change in Phase Along a Beamforming Array	13
Fig. 2.6	Adaptive Beamforming Antenna Structure	15
Fig. 2.7	Four-Omnidirectional-Element Array Pattern	17
Fig. 2.8	Four-Cardioid-Element Array Pattern	17
Fig. 3.1	Multipath Propagation Environment	22
Fig. 3.2	Path Arrival Generation in the HMCH	33
Fig. 3.3	Path Amplitude Generation in the HMCM	35
Fig. 3.4	Macrocell Multipath Propagation Environment	37
Fig. 3.5	Geometrically Based Circular Model I	38
Fig. 3.6	Geometrically Based Circular Model II	39
Fig. 3.7	Tapped Delay Line Model for Frequency Selective Fading Channel	41
Fig. 3.8	Vectorial Combining of Bins to Generate IS-95 Multipath Signals	43
Fig. 3.9	IS-95 Multipath Power Profile Generation in the CMCM	44
Fig. 4.1	Baseband DS/CDMA System	49
Fig. 4.2	Signal Spreading in DS/CDMA	50
Fig. 4.3	Power Spectra of Data and Spread Signals	52
Fig. 4.4	IS-95 Downlink Traffic Channel Waveform Generation	53
Fig. 4.5	IS-95 Downlink Convolutional Encoder	54

Fig. 4.6	IS-95 Uplink Traffic Channel Waveform Generation.....	57
Fig. 4.7	IS-95 Uplink Convolutional Encoder	58
Fig. 4.8	Four-Finger RAKE Receiver Structure.....	60
Fig. 4.9	IS-95 Downlink Receiver Structure.....	63
Fig. 4.10	IS-95 Uplink Receiver Structure.....	63
Fig. 4.11	IS-95 BER Performance Simulation Flow Diagram.....	69
Fig. 5.1	3-Tier Cell Structure Consisting of 19 Hexagonal Cells	74
Fig. 5.2	Flow Diagram for Pre-estimation System Parameter Generation	83
Fig. 5.3	Uplink Capacity Simulation Flow Diagram	87
Fig. 5.4	Downlink Capacity Simulation Flow Diagram	88
Figure 6.1	Single-Path Uplink Capacity as a Function of Antenna Design.....	92
Figure 6.2	Single-Path Downlink Capacity as a Function of Antenna Design	93
Figure 6.3	Single-Path Uplink Capacity as a Function of Power Control. The Considered Antenna Has Cardioid Pattern With $FTBPR = 15$ dB and HPB $= 120^\circ$	96
Figure 6.4	Single-Path Uplink Capacity as a Function of Path Loss Index. The Considered Antenna Has Cardioid Pattern With $FTBPR = 15$ dB and HPB $= 120^\circ$	97
Figure 6.5	Multi-path Uplink Capacity as a Function of Antenna Design	98
Figure 6.6	Multi-path Downlink Capacity as a Function of Antenna Design.....	100
Figure 6.7	Multi-path Uplink Capacity as a Function of Area Urbanization. The Considered Antenna Has Cardioid Pattern With $FTBPR = 15$ dB and HPB $= 120^\circ$	101
Figure 6.8	Multi-path Downlink Capacity as a Function of Area Urbanization. The Considered Antenna Has Cardioid Pattern With $FTBPR = 15$ dB and HPB $= 120^\circ$	102

List of Abbreviations

AOA	Angle of Arrival
AWGN	Additive White Gaussian Noise
BER	Bit Error Rate
BS	Base Station
CDF	Cumulative Density Function
3G	3rd Generation
CDMA	Code Division Multiple Access
CMCM	IS-95 CDMA Multipath Channel Model
CRC	Cyclic Redundancy Check
DS-SS	Direct Sequence Spread Spectrum
DS/CDMA	Direct Sequence Code Division Multiple Access
FDMA	Frequency Division Multiple Access
FEC	Forward Error Correction
FTBPR	Front to Back Power Ratio
GBCM	Geometrically Based Circular Model
GSM	Global System for Mobile Communications
GPS	Global Positioning System
HMCM	Hashemi Multipath Channel Model
HPB	Half-power Beamwidth
LOS	Line of Sight
MAI	Multiple Access Interference
MS	Mobile Station

MSE	Mean Square Error
PCS	Personal Communications Services
PDF	Probability Density Function
PN	Pseudorandom Noise
QPSK	Quadrature Phase Shift Keying
RF	Radio Frequency
RMS	Root Mean Square
SDMA	Spatial Division Multiple Access
SER	Symbol Error Rate
SHSP	Simplified Hashemi Multipath Channel Model Simulation Program
SIR	Signal to Interference Ratio
TDMA	Time Division Multiple Access

List of Symbols

bw	Half Power Beamwidth
α_{ref}	Direction of the Main Lobe
α	Direction of the Incoming Signal
$G(\alpha)$	Antenna Gain for the Incoming Signal
ω	Angular Frequency of the Signal Wave
f	Frequency of the Signal Wave
$\psi, \psi(t)$	Phase of the Signal Wave
$A(t)$	Amplitude of the Signal Wave
$R, R(t)$	Complex Representation of the Signal Wave
λ	Wavelength
p	Number of Sensors in the Antenna Array
d_i	Perpendicular Distance of the i -th Sensor from the Impinging Wavefront
β	Angle of Incidence of the Wavefront
W_i	Complex Steering Weight for the i -th Sensor
$R(\alpha, \beta)$	Combined Complex Signal of the Beamforming Array
$g(\alpha)$	Gain of the Cardioid Elements in the Beamforming Array
D	Directivity of the Antenna Pattern
T_m	Multipath Delay Spread
B_{co}	Channel Coherence Bandwidth
B_d	Doppler Spread
T_{co}	Channel Coherence Time
$h(t)$	Impulse Response of the Multipath Channel

a_k	Amplitude of the k -th Multipath
t_k	Arrival Time of the k -th Multipath
θ_k	Phase of the k -th Multipath
t_o	The LOS Path Delay
P_i	Probability of Having a Path Arrival in the i -th Bin
λ_i	Probability of Path Occurrence Parameter for the i -th Bin
K	Path Arrival Probability Modifier
x_j	Log-amplitude of the j -th Bin
μ_j	Standard Mean of the Log-amplitude of the j -th Bin
σ_j^2	Standard Variance of the Log-amplitude of the j -th Bin
μ'_j	Conditional Mean of the Log-amplitude of the j -th Bin
$\sigma_j'^2$	Conditional Variance of the Log-amplitude of the j -th Bin
$\rho_{j-1,j}$	Correlation Coefficient Between the $(j-1)$ -th and j -th Bins
$N_{j-1,j}$	Number of Empty Bins Between the $(j-1)$ -th and j -th Bins
θ	Angular Spread
R_m	Radius of the Scattering Circle in the GBCM
L	Distance Between the BS and MS
P_j	Power Level of the j -th Chip
E_b	Data Energy Per Bit
T_b	Data Sequence Period
T_c	Chip Period
$d(t)$	Data Source
$p(t)$	PN Sequence Signal

$i(t)$	Channel Interference
$r(t)$	Received Signal
$S_D(f)$	Power Spectral Density of an Infinite Random Data Sequence
B_D	Power Spectrum of the Data Signal
B_{ss}	Power Spectrum of the Spread Signal
Z_k	Output of the k -th Finger
r_k	Amplitude of the k -th Finger Signal
θ_k	Phase of the k -th Finger Signal
n_k	White Gaussian Noise in the k -th Finger Output
Z_c	Combined Output Using Maximum Ratio Combining
$\frac{N_0}{2}$	White Noise Power Spectral Density
SIR_{max}	Maximum SIR as a Result of Maximum Ratio Combining
r	Rate of the Convolutional Encoder
K	Constraint Length of the Convolutional Encoder
g_0, g_1, g_2	Generator Functions of the Convolutional Encoder
m	Root Mean Squared Value of the Rayleigh Distributed Signal Amplitude
$P(m)$	Probability Density Function of the Rayleigh Distribution
σ^2	Time Average Power of the Rayleigh Distributed Signal
P_e	Symbol Error Probability
α_l	Rayleigh Faded Amplitude of the l -th Multipath Component
R_{cell}	Radius of the Hexagonal Cell
d_L	Propagation Distance
γ	Path Loss Exponent

ξ	Gaussian Random Variable with Zero Mean and Standard Deviation σ
σ	Shadowing Standard Deviation
P_T	Transmitted Signal Power
P_R	Received Signal Power
W	Channel Bandwidth
R	Information Bit Rate
Z	Chernoff Bound for the Symbol Error Rate
E_s	Data Energy Per Symbol
E_s/I_0	SIR Per Symbol
E_b/I_0	SIR Per Bit
$(P_d)_k$	Received Signal Power of the k -th Mobile User
x_k	Voice Activity of the k -th Mobile User
$(P_i)_k$	Overall Interference Power of the k -th Mobile User
$I_{k,l}$	Interference Introduced to the k -th Mobile User by the l -th User
P_m	Pilot Signal Power Received from the m -th Base Station
M	Link Loss Matrix
$m_{k,l}$	An Entry in the Link Loss Matrix M
$(P_t)_k$	Transmitted Signal Power of the k -th Mobile User
$C(x)$	CDF Function of the System Capacity

Acknowledgments

I would like to take this opportunity to express my greatest gratitude towards my supervisor at the University of British Columbia, Dr. P. Takis Mathiopoulos, for his patient, encouraging and professional guidance throughout my graduate study. Even though I had started to work full-time for Motorola and Lucent Technologies in U.S.A. before I wrote this thesis, he continued to provide his fullest technical support and spent lots of his precious time helping me with the several revisions of this thesis remotely. I would like to thank Dr. Andrew S. Wright from Datum Telegraphics Inc., who shared his abundant technical knowledge with me without reservation and provided tremendous insights on the research of this thesis. Many thanks are also directed to Telus Mobility (formerly BCTEL Mobility) and Advanced System Institute (ASI) of BC for providing an Industrial Partnership program. I am most grateful to the late Greg Acres, formerly with Telus Mobility, for his technical support and interest in this research project. I wish to dedicate this work to his memory.

Chapter 1 INTRODUCTION

Code Division Multiple Access (CDMA) is an access technique that allows the users to share the same frequency band within one cell and among multiple cells utilizing Direct Sequence Spread Spectrum (DS-SS) technology. As compared to the narrowband technologies of Frequency Division Multiple Access (FDMA) and Time Division Multiple Access (TDMA), the inherent wideband nature of CDMA provides several important improvements including multipath fading mitigation, soft system capacity¹ (i.e. the ability to trade voice quality for system capacity and vice-versa), higher system capacity; low signal detectibility and high data security [1][2][3].

CDMA technology was mainly used in military applications until early 1990 [2], when QUALCOMM Inc., introduced the intensive system concepts and the innovative implementation approaches on commercial digital cellular CDMA systems. This CDMA system was subsequently standardized and is known as the IS-95 standard [4]. It operates in the 800 MHz cellular band as well as the 1900 MHz Personal Communication Systems (PCS) band. Since the first IS-95 cellular network was successfully launched in HongKong in 1995, the IS-95 CDMA has become a fully accepted wireless technology and competes with the TDMA-based GSM technology for dominance in the cellular world [5]. In North America, CDMA has become the most prevalent wireless technology utilized in digital cellular networks [5][6]. The number of CDMA systems and subscribers in the rest of the world is also rapidly rising. Due to these advantages, as compared to FDMA and TDMA technologies, CDMA has been selected as the multiple access technique for the 3rd Generation (3G) cellular systems [6][7].

¹ In this thesis, capacity refers to the average number of users/cell, not bits/sec/Hz.

In the past few years, the number of cellular communication users has been increasing rapidly and the demand for transmission of voice and large volumes of data such as text, images and video has grown dramatically [8][9]. However, as the available cellular bandwidth is limited, techniques to further increase the capacity of cellular networks have garnered tremendous research efforts. Among the techniques suitable for use in conjunction with CDMA systems, the employment of adaptive beamforming antennas to realize Spatial Division Multiple Access (SDMA) is an active research area [10][11][12]. Based on high resolution direction finding algorithms, such as MUSIC [13] and ESPRIT [14], the Base Station (BS) continually distinguishes between desired signals, multipaths, and interfering signals, as well as estimates their Angles of Arrival (AOA). This information is used, on the one hand, to design a beamforming antenna array that coherently combines the desired signals in the uplink, on the other hand, selectively transmit signals in the downlink. The ability to receive and transmit signals selectively in the space dimension ensures that the interference is constantly minimized and a higher Signal to Interference Ratio (SIR) is achieved for each radio channel in a CDMA system [10][17]. Thus the interference rejection capability of the adaptive beamforming system provides a significantly higher system capacity as compared to the capacities achieved employing conventional antennas.

At the time the research for this thesis began back in 1998, there were relatively few papers published in the open technical literature on the subject of adaptive beamforming antennas in conjunction with CDMA systems. These publications dealt mainly with generic and simplified CDMA systems, rather than the specific IS-95 standard. For example, although in [15], the multipath radio channel modelling of communication systems with beamforming antenna arrays is presented, it does not specifically address their use in CDMA systems. In [10], [16] - [20], there have been a variety of investigations on CDMA capacity improvements using beamforming

antenna arrays. Most of these papers have dealt with the CDMA capacity estimations based upon greatly simplified system assumptions and have not taken into account some of the important features of the CDMA radio channels, such as multipath, signal fading, imperfect power control, and Forward Error Correction (FEC) in the receiver structure. Among them, only [10] and [20] have considered some simplified channel fading conditions, but without imperfect power control. Furthermore, in these papers only simplified antenna patterns (e.g. omnidirectional) have been considered. In our research [21], we will consider more sophisticated antenna patterns (e.g. cardioid) in beamforming arrays and will accurately investigate the effects of more realistic radio channel models have on the capacity of an IS-95 system using beamforming techniques. In doing so, we have designed and developed a very generic software simulator which accurately estimates the capacity of the IS-95 systems employing beamforming techniques and using realistic antenna patterns as well as more realistic multipath channel models. More specifically the main contributions of the thesis can be summarized as follows.

- The use of cardioid antennas in a beamforming array to further reduce the interference in the IS-95 systems is proposed. Its interference mitigation performance compared with conventional antennas and beamforming arrays composed of omnidirectional antennas is presented based upon the simulated IS-95 system capacity results.
- Propose an extended IS-95 multipath model that can generate random multipath power profiles for the IS-95 radio channels and for four distinct geographical areas of different urbanization characteristics varying from, a heavily urban city to a small residential town.
- The BER performance of the IS-95 receivers with RAKE combiners is investigated for a large set of multipath power profiles in a Rayleigh fading environment through computer simulations. The SIR per bit thresholds for the simulated power profiles to maintain an

average BER of 10^{-3} in order to retain adequate call quality are obtained for both the downlink and uplink.

- Using the previously mentioned multipath channel models, the system capacities of the IS-95 systems are obtained for different antenna configurations at the BS through computer simulations. Capacity improvements using adaptive beamforming antenna arrays over that using conventional antennas are evaluated.

The thesis consists of seven chapters and 2 appendices. After this introductory chapter, the thesis is organized as follows.

Chapter 2 presents an overview of the various antenna technologies considered in this thesis, including omnidirectional, ideal 3-sectored and cardioid 3-sectored antennas, and adaptive beamforming arrays. Their antenna gain patterns are derived and their interference mitigation performance in terms of directivity is obtained and compared.

In Chapter 3, an extended multipath channel model for the IS-95 systems is proposed. The chapter begins with the introduction of slow fading and fast fading in wireless mobile radio channels. An overview of Hashemi's study on multipath radio propagation channel [22] and the Geometrically Based Circular Model (GBCM) [15] are then presented. In order to model the power distributions of multipath signals in the actual IS-95 cellular frequency band, the Hashemi model is modified by employing linear extrapolation methods. The GBCM is employed in conjunction with the modified Hashemi model to predict the AOAs of the multipath signals which will be used in the capacity estimations.

Chapter 4 includes detailed discussions on the waveform generations in the IS-95 systems.

Specifically, the spreading procedures using Walsh functions and PN codes, FEC using convolutional encoding, RAKE receiver combining and modulation schemes are examined. The BER performance of the IS-95 receivers with RAKE combining is simulated for the multipath Rayleigh faded channels. The SIR per bit thresholds required to maintain an average BER of 10^{-3} for different power delay profiles are obtained for both the downlink and uplink.

In Chapter 5, the IS-95 system capacity simulation model is presented. We describe the model for the multicell configuration and user distribution. Afterwards the important channel parameters including channel fading, power control and voice activity are discussed in detail and the Gaussian approximation for interference calculation is explained. Finally, the overall simulation methodology is presented, with discussions on the single-path and multi-path simulation approaches.

In Chapter 6, we present the IS-95 system capacity simulation results. The capacity results for various system antenna designs are depicted in Cumulative Density Function (CDF) graphs as well as given in the form of tables. The capacity improvements using beamforming antenna arrays are estimated from both the single-path and multi-path simulation approaches.

In Chapter 7, we present the conclusions of the thesis, together with suggestions for future research. Finally in Appendices A and B, the simulation results of the previously mentioned Hashemi multipath channel model and the IS-95 BER performance model are presented respectively.

Chapter 2 ANTENNA MODELS

2.1 Introduction

It is well known that the manner in which electromagnetic energy is distributed into and collected from the surrounding space has a profound influence on the efficient use of the frequency spectrum. Many cellular systems use antennas of rather omnidirectional patterns to provide a large coverage region. To mitigate interference, directional 3-sectored antennas which split a 360° region into three sectors are commonly used [1][10]. An adaptive beamforming array with digital signal processing capabilities combines multiple antenna elements to continually change the directionality of its radiation and reception patterns in response to a constantly changing mobile Radio Frequency (RF) environment. The use of spatial processing techniques using beamforming arrays has been demonstrated to be an attractive approach to further increase CDMA capacity without allocating additional frequency spectrum (see for example, [15]-[20], [23][24]).

In this chapter, we explore several different antenna configurations which can be used at the BS of the IS-95 systems and their associated coverage patterns in the azimuth direction (horizontal plane), while similar to other authors (e.g. [25]), the vertical variations of antenna gain patterns are omitted for the sake of simplicity. In Section 2.2, we describe omnidirectional antennas. Directional sectored antenna patterns are discussed in Section 2.3, which include both ideal 3-sectored antenna patterns and practical 3-sectored antennas of cardioid patterns. This is followed by a detailed discussion of adaptive beamforming arrays in Section 2.4, where the antenna gain patterns of the beamforming arrays are derived and the use of cardioid elements in beamforming arrays is proposed. In Section 2.5, we compare the interference mitigation performance

for the above antenna patterns based upon the calculated directivity and discuss their impacts on the capacity of CDMA systems. Finally, in Section 2.6, the conclusions of the chapter are presented.

2.2 Omnidirectional Antenna

Since the early days of wireless communication, there has been the simple dipole antenna [26], which radiates and receives energy equally well in all directions. This single element antenna design broadcasts omnidirectionally in a pattern resembling the ripples radiating outward in water to find its receivers. Only a small percentage of the overall energy is sent to and received from the desired receiver. As illustrated in Fig. 2.1, this type of antenna has a unity gain for signals coming from any direction and thus provides the widest possible coverage. Given this limitation, omnidirectional antennas attempt to overcome the massive energy loss by simply boosting the transmit power level of the broadcast signals. In a multi-user cellular system, this strategy adversely impacts the system capacity as the served user might receive a weak signal whereas the other users might receive strong interference.

2.3 Directional Sectored Antenna

A single-element antenna can also be constructed to have certain fixed preferential transmission and reception directions. In cellular systems, the well-known technique of cell sectorization is usually employed at the BS for both receiving and transmitting signals [1][10][20]. 3-sectored antennas which cover an approximate 120° region are commonly used. The interference sources seen by 3-sectored antennas are therefore approximately one third of those seen by omnidirectional antennas.

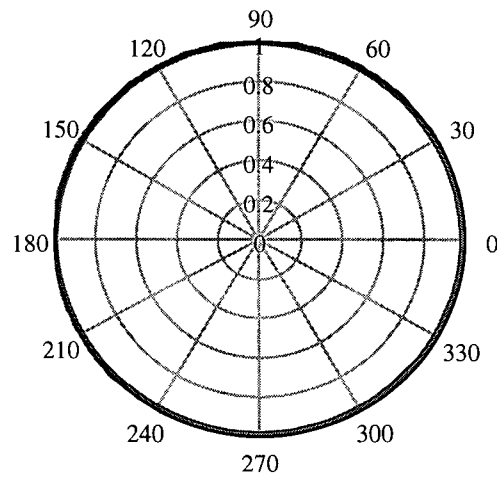


Fig. 2.1 Omnidirectional Antenna Pattern

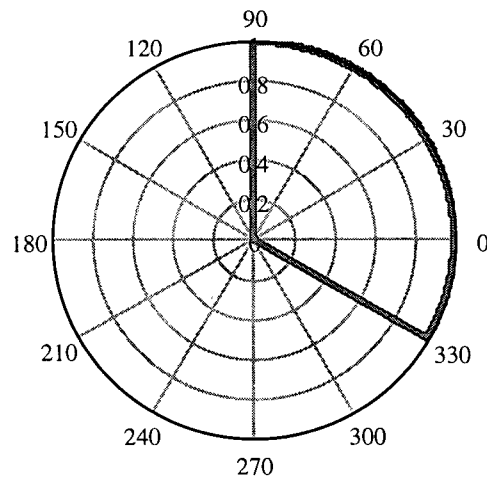


Fig. 2.2 Ideal 3-Sectored Antenna Pattern

2.3.1 Ideal 3-Sectored Antenna

In order to simplify mathematical analysis, ideal 3-sectored patterns have been widely used in existing technical publications when estimating the capacities of cellular systems (see for example, [1][3][20]). As illustrated in Fig. 2.2, the ideal 3-sectored antenna pattern has a normalized unity antenna gain for signals coming within its 120° sector and absolute zero gain within the other two sectors. While the ideal 3-sectored pattern presents a simplified model for analysis, it does not accurately model the practical 3-sectored antennas used in operational cellular network BS.

2.3.2 Cardioid 3-Sectored Antenna

The practical 3-sectored antennas used in cellular systems can be more accurately modelled by the cardioid pattern. The cardioid antenna pattern is defined using the so called “Front-to-Back-Power-Ratio” (FTBPR) and Half-Power-Beamwidth (HPB) [10][26]. The FTBPR refers to the ratio of the radiation power intensity of the maximum of the main lobe over that of the back lobe. The HPB is the angle between the two directions in which the radiation power intensity is one-half of that of the main lobe, where the main lobe is the direction of the maximum antenna gain [26]. The HPB thus defines the angular region where the signal radiation and reception are the strongest. The gain of the cardioid antenna patterns is given by [10][26]

$$\tau = \frac{\log\left(\frac{1}{\sqrt{2}}\right)}{\log\left(\frac{1 + \cos\left(\frac{bw}{2}\right)}{2}\right)}$$

$$G(\alpha) = \left(\left(\frac{1 + \cos(\alpha - \alpha_{ref})}{2} \right)^\tau + 10 \left(\frac{FTBPR}{-20} \right) \left(\frac{1 - \cos(\alpha - \alpha_{ref})}{2} \right)^\tau \right)^2 \quad (2.1)$$

where τ is an intermediate variable for representation convenience, bw is the HPB, which is equal to 120° for 3-sectored antennas, α is the direction of the signal of interest, α_{ref} is the direction of the main lobe and $FTBPR$ is the FTBPR in dB. The antenna gain defined in Eq. (2.1), ranges from a very small number in the back lobe to a maximum value of 1 in the main lobe. Fig. 2.3 illustrates the computer generated pattern of a cardioid 3-sectored antenna with $FTBPR = 15$ dB and $\alpha_{ref} = 30^\circ$. It can be seen that the transmission and reception of signals are the strongest in the main lobe ($\alpha = 30^\circ$) and weakest in the back lobe ($\alpha = 210^\circ$).

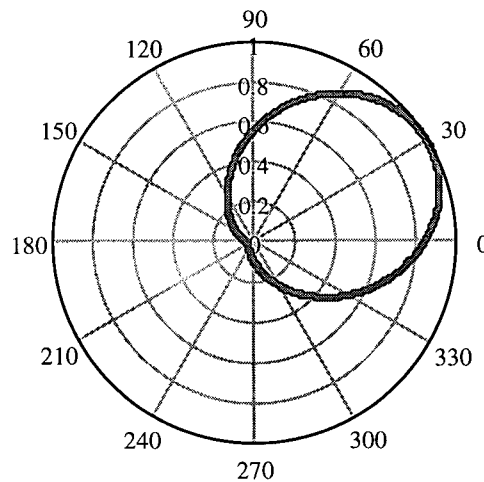


Fig. 2.3 Cardioid 3-Sectored Antenna Pattern

While 3-sectored antennas provide increased gain as compared to standard omnidirec-

tional antennas, they do not overcome the major disadvantages of the signal broadcast design. In order to further improve the capacities of cellular systems, more advanced antenna techniques, such as adaptive beamforming arrays, need to be adopted.

2.4 Adaptive Beamforming Antenna Array

Adaptive antenna arrays have been successfully used for a long time in many engineering applications, including military and commercial systems (e.g. radar and telecommunications) [27]. Using a variety of advanced digital signal processing algorithms, the adaptive antenna system takes advantage of its ability to effectively locate and track signals in order to constantly and dynamically minimize interference and maximize signal reception in a wireless communication system.

An adaptive antenna system consists of an array of spatially distributed antenna elements, which can be arranged in linear, circular or planar configurations¹. By properly phase shifting the transmitted and received signals at each of the successive antenna elements, a beam, which represents the direction of the maximum antenna gain, can be steered towards the desired user to maximize the combined transmission and reception signal strength as well as reduce interference.

The linear array considered in this thesis is the most basic and common configuration for adaptive antennas, in which all antenna elements are placed along a straight line and are equally spaced. The antenna element spacing is typically $\lambda/2$ (λ is the wavelength) since larger spacing results in the formation of grating lobes (secondary beams) and in general terms degraded perfor-

¹ It should be noted that this thesis considers only linear arrays for the sake of simplicity.

mance [28]. Thus, let us consider a linear array consisting of p number of omnidirectional elements as depicted in Fig. 2.4. It is assumed that the array is illuminated by a single RF source that is located in the far field so that the impinging wavefronts are planar and paralleled to one another upon arrival at the antenna array sensors.

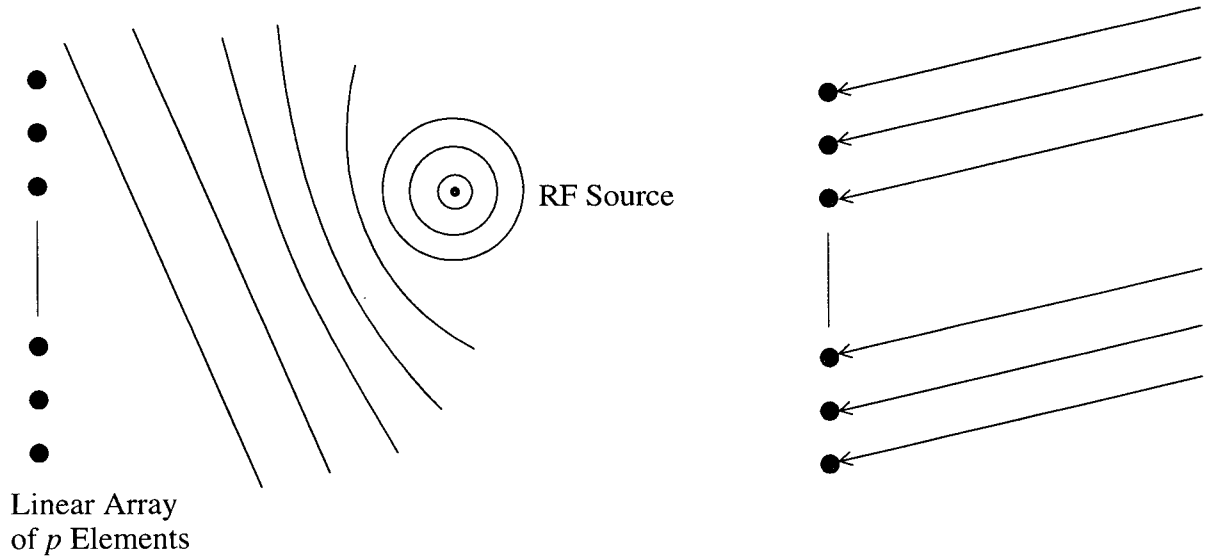


Fig. 2.4 Wavefronts Impinging Upon a Beamforming Array

The signal impinging upon a single antenna sensor is a complex waveform and can be mathematically expressed as

$$R(t) = A(t)e^{j[\omega t + \psi(t)]} \quad (2.2)$$

where $A(t)$ is the amplitude of the wave, ω is the angular frequency ($\omega = 2\pi f$ where $f = 1/\lambda$ is its frequency), and $\psi(t)$ denotes the phase of the wavefront. After normalizing the signal and performing a reduction to complex baseband, the instantaneous sensor output can also be represented as

$$R = e^{j\Psi} \quad (2.3)$$

where ψ denotes the instantaneous phase of the wavefront as $\psi(t)$. Each sensor of the array receives the signal which is phase shifted relative to the first sensor of the array, usually referred to as the phase centre, by an amount proportional to the perpendicular distance of the sensor from the impinging wavefront, as shown in Fig. 2.5.

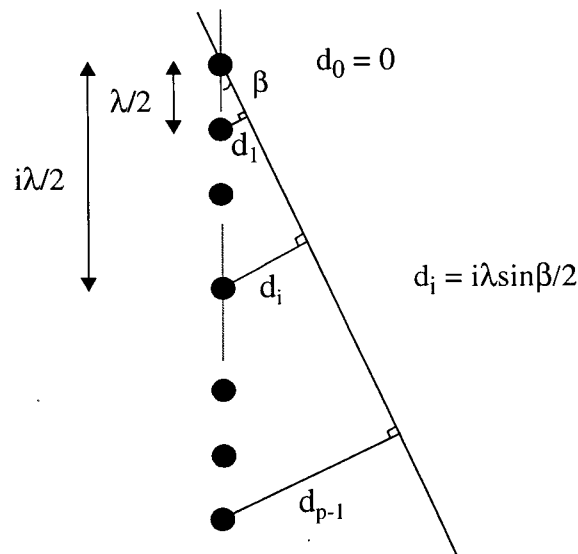


Fig. 2.5 Illustration of Change in Phase Along a Beamforming Array

The phase change associated with an increase in the distance of a wavelength λ is 2π and therefore the phase for the i -th sensor is given by

$$\psi_i = \frac{-2\pi d_i}{\lambda} = -i\pi \sin\beta \quad (2.4)$$

where β is the angle of incidence of the wavefront. Clearly, in Fig. 2.5, the distance d_0 is zero and

therefore the relative phase at the first sensor is zero. If each sensor's signal is multiplied with a complex beam steering weight $W_i = \exp(ji\pi \sin \alpha)$ and then all p signals combined, the overall signal can be mathematically expressed as

$$R(\alpha, \beta) = \sum_{i=0}^{p-1} \exp[ji\pi(\sin \alpha - \sin \beta)] \quad . \quad (2.5)$$

Clearly, the magnitude of the normalized combined signal reaches its maximum when $\alpha = \beta$. This array with steering weights W_i therefore effectively steers a beam towards the direction of the desired signal, β , while interfering signals in other directions are reduced.

At any angle, the antenna power gain of the antenna array is the square of the normalized signal magnitude. For an array pattern which steers a beam towards an angle of β , the gain for the signals impinging on the array at an angle of α is thus given by

$$G(\alpha, \beta) = \left| \sum_{i=0}^{p-1} \exp[ji\pi(\sin \alpha - \sin \beta)] \right|^2 \quad . \quad (2.6)$$

The basic structure of an adaptive digital beamforming antenna array is illustrated in Fig. 2.6. The system can be regarded as an adaptive spatial filter that effectively filters out the interfering signals [28]. With enhanced digital signal processing capabilities, the adaptive control processor can constantly and dynamically adjust the steering weights for optimal signal transmission or reception as the RF environment changes.

At each antenna element, the combined received signal is not known in terms of its indi-

vidual signals, but is received as a wavefront superposition corrupted by the Additive White Gaussian Noise (AWGN) introduced by the antenna element. In order to calculate the optimal weights of the array, the number of the incident wavefronts and their associated AOAs must be correctly identified. This is done by converting the wavefronts at each sensor to complex digital signals and using the multiple signal classification algorithms, e.g. MUSIC and ESPRIT [13][14][29]. In this thesis, we assume that perfect estimations of the number of signals and their AOA information are available for the sake of simplicity, i.e. the estimation error of the individual signal information due to the AWGN is ignored.

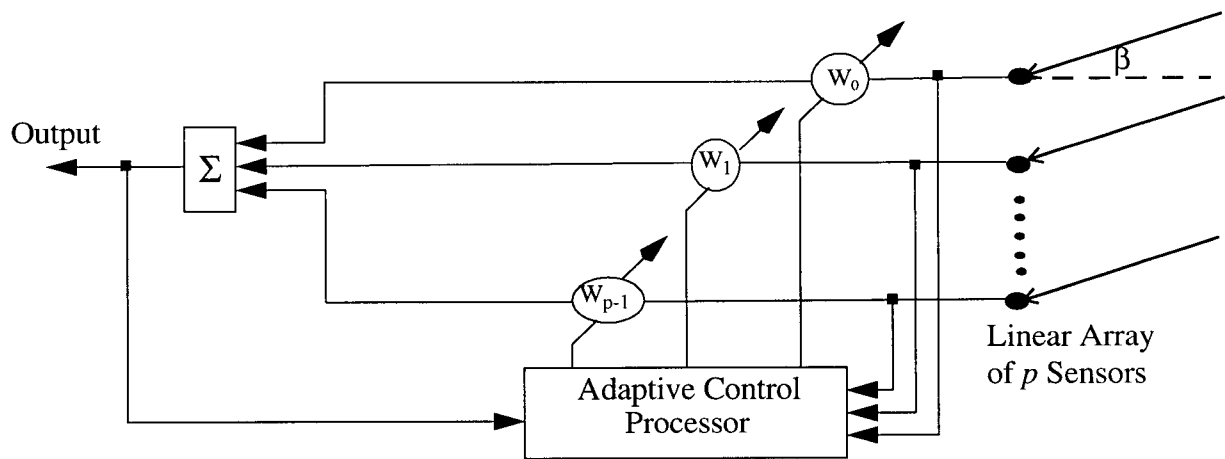


Fig. 2.6 Adaptive Beamforming Antenna Structure

Adaptive antenna arrays may also be used at the BS for transmitting signals to the mobile station (MS) receivers. Since for cellular systems the transmitter and receiver typically operate in a duplex mode using two different frequency bands that are close to each other (e.g. an IS-95 system [4]), the directivity of the transmitted and received signals is similar [30]. The adaptive

beamforming array at the BS transmitter can thus be adjusted by performing a straight transformation on the steering weights of the receiving antennas in order to steer a beam towards the MS receiver, resulting in a signal receiving pattern at the MS receiver being largely similar to that at the BS receiver [30].

For a cellular telecommunication system in which each cell is split into three sectors, the antenna elements are usually not placed along a south-north line, but along a line that is perpendicular to the centre line of the sector. Fig. 2.7 illustrates a computer generated antenna pattern for a four-omnidirectional-element array that steers a beam towards an angle of 30° . This antenna array provides signal coverage for the sector covering the region from -30° (330°) to 90° with the antenna elements being placed along the 120° line. It can be seen that the steered pattern also creates an undesired side beam at 150° , which causes the system to suffer great interference from this direction. This is a common problem for antenna arrays using omnidirectional sensors and can be mathematically explained from Eq. (2.6) as

$$G((180^\circ - \alpha), \beta) = G(\alpha, \beta) \quad (2.7)$$

In order to solve this “undesired side beam” problem in a multiple-omnidirectional-element beamforming array, we propose in this thesis that cardioid antenna elements be used instead to provide enhanced directionality. For a beamforming array using cardioid antenna elements, the main lobe of each element is placed in parallel to the centre line of the sector. In this case, the antenna gain in Eq. (2.6) needs to be modified to

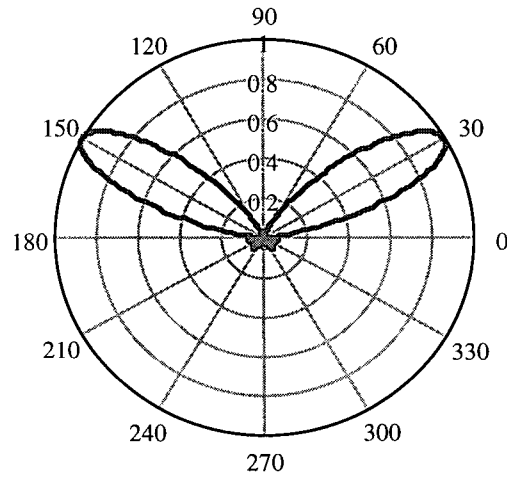


Fig. 2.7 Four-Omnidirectional-Element Array Pattern

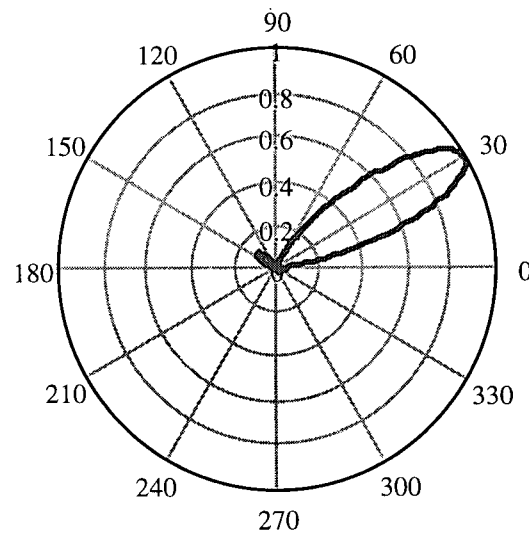


Fig. 2.8 Four-Cardioid-Element Array Pattern

$$G(\alpha, \beta) = \left| \sum_{i=0}^{p-1} \exp[ji\pi(\sin\alpha - \sin\beta)] \right|^2 g(\alpha) \quad (2.8)$$

where $g(\alpha)$ is the gain of the individual cardioid antenna element and is calculated using Eq. (2.1). As illustrated in Fig. 2.8, using equivalent (i.e. four element array) antennas with cardioid patterns, the interference previously present at 150° is now significantly suppressed.

2.5 Antenna Interference Suppression Performance

The interference suppression performance of an antenna pattern can be measured by its directivity, which is defined as [30]

$$D = \frac{2\pi}{\int_0^{2\pi} g(\alpha, \beta) d\alpha} \quad (2.9)$$

where $g(\alpha, \beta)$ is the antenna gain and is calculated using Eqs. (2.1), (2.6) and (2.8) for 3-sectored cardioid antennas and adaptive beamforming arrays. For the purpose of this thesis, we will examine the effects on the IS-95 system capacities of the following antenna configurations. These patterns are chosen because they have been previously studied for their use in generic CDMA systems [16], [18]-[20] and/or they provide enhanced interference performance.

- Omnidirectional antenna
- Ideal 3-sectored antenna
- Practical 3-sectored antenna of cardioid pattern
- Adaptive beamforming array using 4 omnidirectional sensors
- Adaptive beamforming array using 6 omnidirectional sensors
- Adaptive beamforming array using 8 omnidirectional sensors
- Adaptive beamforming array using 4 cardioid sensors

Table 2.1. lists the directivity values of the above seven antenna configurations which we will deal with in our IS-95 CDMA capacity study. It is obvious that $D = 1$ for omnidirectional antennas and $D = 3$ for ideal 3-sectored antennas. Directivity for the remaining patterns is calculated using computer numerical integration methods based upon Eqs. (2.1), (2.6), (2.8) and (2.9). It can be seen that beamforming arrays provide the highest directivity and thus the best interference suppression performance as compared to conventional omnidirectional and 3-sectored antennas. For 3-sectored antennas, the cardioid pattern has a slightly lower directivity than the ideal pattern, which suggests that using the ideal 3-sectored pattern may lead to an overestimation of the capacity performance of a cellular CDMA network [1][3]. By using more antenna elements or cardioid elements in a beamforming array, a higher directivity can be achieved.

Antenna Configuration	Directivity
Omnidirectional Pattern	1
Ideal 3-sectored Pattern	3
3-sectored of Cardioid Pattern ($FTBPR = 15$ dB, $HPB = 120^\circ$)	2.6
Four-Omnidirectional-Element Array That Steers Towards 60° (Sector Covers Region from -30° to 90°)	4.6
Six-Omnidirectional-Element Array That Steers Towards 60° (Sector Covers Region from -30° to 90°)	9.0
Eight-Omnidirectional-Element Array That Steers Towards 60° (Sector Covers Region from -30° to 90°)	11.4
Four-Cardioid-Element Array That Steers Towards 60° ($FTBPR = 15$ dB, $HPB = 120^\circ$, Sector Covers Region from -30° to 90°)	10.9

Table 2.1 Antenna Directivity for the Simulated Antenna Patterns

For a wireless communication system the use of 3-sectored antennas and beamforming antenna arrays reduces interference and thus improves capacity. Directivity represents the average interference suppression performance of the antenna system. As such, it provides an estimate of the possible capacity improvements that can be achieved since the capacity is inversely proportional to the interference in a CDMA system [1][10]. Clearly from Table 2.1, significant capacity improvements can be achieved by using beamforming antenna arrays that consist of four or more sensors.

2.6 Conclusions

In this chapter, we have discussed the conventional omnidirectional and directional 3-sectored antennas and explained their disadvantages due to the limited directionality in their antenna patterns. Following that, the cardioid antenna pattern was introduced and mathematically defined in order to accurately model practical 3-sectored antennas. We then discussed linear beamforming antenna arrays in wireless communication systems and presented their basic structures, features and benefits. To further reduce the interference level at the receiver, we proposed using cardioid instead of omnidirectional antennas in a beamforming array. Finally, the chapter was concluded by defining the directivity of the seven antenna configurations that will be dealt with in our IS-95 capacity study. Their interference mitigation performance was also compared based upon the calculated directivity.

Chapter 3 IS-95 MULTIPATH CHANNEL MODEL

3.1 Introduction

In a wireless communication system a signal transmitted into the mobile channel interacts with the environment in a complex manner. The design of wireless systems for rural open areas usually assumes a strong direct Line of Sight (LOS) signal [31]. However, in an urban environment, the assumption of a LOS transmission path between the MS and BS is no longer valid. Instead, there are reflections from large objects, diffraction of the electromagnetic waves around objects and signal scattering. The result of these complex interactions is the multipath replicas of the same signal at the receivers of the BS and MS.

A simplified picture of the multipath environment with two MSs is illustrated in Fig. 3.1. The propagating signal is reflected from different objects in the physical environments, and multiple replicas of the signal arrive at the receiver after travelling over different transmission paths. Each signal replica has a different amplitude, time delay, phase shift and AOA when arriving at the receiver. In order to accurately simulate the capacities of IS-95 systems, the multipath mobile radio channel in which the signals are transmitted must be appropriately modelled. This chapter will present the multipath channel model considered in this thesis. It will discuss the modelling of the signal fading and scattering effects, as well as the multipath channel response of the IS-95 wide-band channel. The organization of this chapter is as follows. After this introduction, Section 3.2 presents the large-scale fading model which accounts for the propagation loss and shadowing loss. Section 3.3 presents the small-scale fading model with Rayleigh distribution and discusses the parameters to categorize the small-scale fading channels. In Section 3.4, we describe the Hashemi radio channel model and the signal scattering model, then we

propose our extended IS-95 CDMA multipath model based upon the previous two models. Finally, the conclusions of this chapter will be presented in Section 3.5.

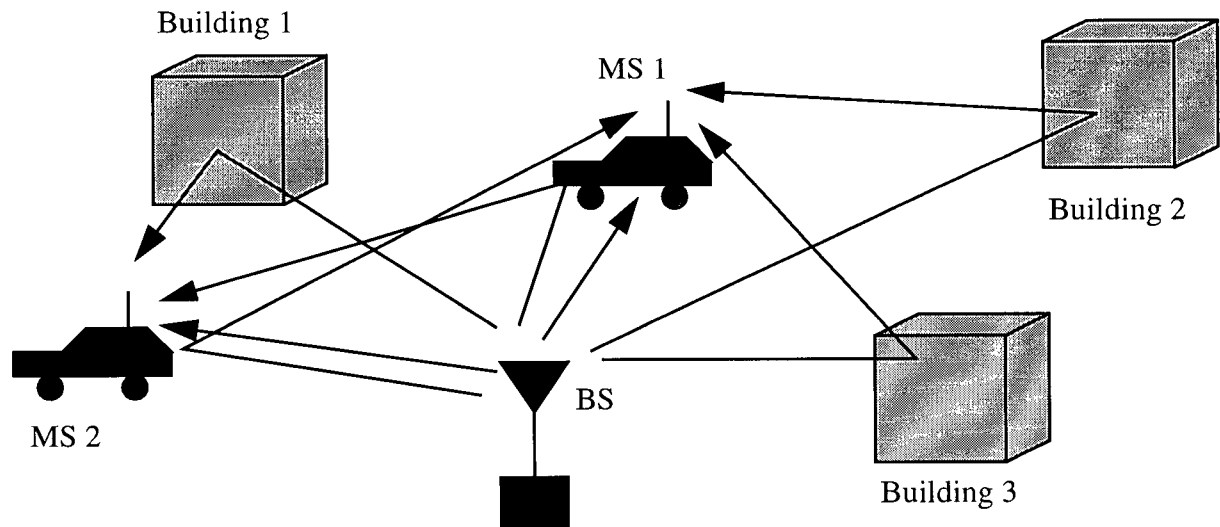


Fig. 3.1 Multipath Propagation Environment

3.2 Large-Scale Fading Model

In this section, we will describe the large-scale fading model for the mobile radio channels. Large-scale fading characterizes the effects of the propagation loss and the diffraction of signals due to the terrains and other obstructive objects which are much larger than the wavelength of the signals. The effect is the very slow change in the local mean received signal strength. The large-scale fading model is used to predict the average received signal strength over receiver movements of 5 to 40 wavelengths [32]. Large-scale fading is mainly due to two factors, namely propagation loss and shadowing [33].

3.2.1 Propagation Loss

From both theoretical and measurement-based propagation models, the average received signal strength decreases logarithmically with the distance, for both outdoor and indoor channels [33]. According to these models, the signal strength is proportional to $d_L^{-\gamma}$, where d_L is the distance between the transmitter and the receiver and γ is the path loss exponent. The value of the path loss exponent is dependent upon the characteristics of the channel environment. In fact, it may vary from an inverse square law very close to the cell site antenna to as great as the inverse 6.0 law in a very dense urban environment such as New York Manhattan [1]. In this thesis, we will use this inverse power law to model the propagation loss of the mobile radio channels.

In our capacity study, simulations are performed for four geographical areas of different urbanization characteristics (namely, downtown San Francisco represents a heavily urban city, downtown Oakland represents a small to medium sized city, downtown Berkeley represents a suburban area and residential Berkeley represents an open rural area). The power loss exponent for each of the four areas assumed in this thesis is determined based upon the values for different terrain characteristics as suggested in [1][34] and are presented in Table 3.1.

Area	Path Loss Exponent
Downtown San Francisco	4.5
Downtown Oakland	4
Downtown Berkeley	3.5
Residential Berkeley	3

Table 3.1 Path Loss Exponents for the Simulated Areas

3.2.2 Shadowing Loss

In addition to propagation loss in a mobile radio channel there is also the effect of shadow-

ing. Shadowing represents the variations in the diffraction and scattering loss caused by the terrain features such as large buildings and hills [33]. Diffraction occurs when the radio path is obstructed by an impenetrable object and secondary waves are formed behind the obstructing body. Scattering occurs when the radio path contains objects with dimensions in the order of the wavelength or less. Scattering causes energy from the transmitter to be re-radiated in many different directions. Shadowing is often modelled as being log-normal distributed [1][3][33][35]. Due to the shadowing effect, the received signal power is proportional to $10^{\xi/10}$, where ξ is a Gaussian random variable with zero mean and standard deviation σ . The value of σ depends upon a number of factors including the terrain configuration and human-made structures of the area. Measurements in macrocell environments show that it may vary from 6-10 dB [32]. In this thesis, the shadowing loss is assumed to be a log-normal random variable with a standard deviation $\sigma = 8$ dB as suggested by Lee [34].

Combining the effects of propagation loss and shadowing, the received signal power P_R is proportional to the transmitted signal power P_T and can be mathematically expressed as

$$P_R \propto P_T \left(\frac{10^{\xi/10}}{d_L^\gamma} \right) \quad (3.1)$$

where ξ is a Gaussian random variable with zero mean and standard deviation $\sigma = 8$ dB, d_L is the distance between the transmitter and receiver, and γ is the path loss exponent. Eq. (3.1) summarizes the means to model the large-scale fading in mobile radio channels in this thesis.

3.3 Small-Scale Fading Model

In this section, we will describe the small-scale fading model for the mobile radio channels. Small-scale fading model characterizes the rapid fluctuations of the received signal strength over very short travel distance (i.e. a few wavelengths) or a short time duration (a few seconds) [34]. It is caused by the interaction between two or more reflections of the transmitted signal arriving at the receiver with random phase offsets, because each reflection generally follows a different transmission path and reaches the receiver at different times. These multipath waves add as random phasors at the receiver antenna to give a resultant signal which can vary widely in both amplitude and phase depending upon the distributions of the power density and relative propagation delays of the waves and the bandwidth of the transmitted signal.

3.3.1 Small-Scale Fading: Parameters and Characterization

In order to characterize the *time dispersive* nature of a multipath channel, the multipath delay spread T_m is commonly used. It denotes the range of delays over which the powers of the multipath components of the same signal are essentially non-zero. For a transmitted impulse, when it arrives at the receiver, it is no longer an impulse but rather a pulse with a delay spread T_m . For example, the delay spread can be defined as the delay at which the power of the received pulse is 30 dB lower than the first received pulse [36]. Table 3.2 lists typical delay spread values for different environments [36].

Type of Environment	Delay Spread T_m
Open Rural Area	$< 0.2\mu s$
Suburban Area	$\geq 0.5\mu s$
Urban Area	$\geq 4.0\mu s$

Table 3.2 Typical Delay Spread Values

Closely related to the multipath delay spread T_m is the coherence bandwidth B_{co} . It denotes the range of frequencies over which two signal components exhibit a strong correlation in their amplitudes [33]. Coherence bandwidth is defined as the reciprocal of the multipath delay spread, such that $B_{co} = 1/T_m$.

For mobile communication systems, the communication channel undergoes random changes introduced as a result of the user's mobility and the relative motion of the scattering objects in the environment. These changes have the effect of shifting, or spreading, the frequency components of a signal. This time varying nature of the channel response in small-scale fading is characterized by the Doppler spread B_d . It denotes the extent of the frequency spectrum broadening caused by the time variations of the mobile radio channel [37]. Doppler spread B_d is a function of the velocity of the MS and the angle between the direction of the receiver and the AOA's of the scattered waves. The reciprocal of the Doppler spread, T_{co} , is referred to as the coherence time of the channel. It is a measure of the time duration over which the impulse response of the radio channel is essentially invariant [37]. It essentially denotes the rate at which the channel characteristics change and channel fading occurs.

When a signal is transmitted over a multipath fading channel, if B_{co} is small as compared to the bandwidth of the transmitted signal, the channel is characterized as *frequency-selective* [38], i.e. the fading due to multipath randomly affects only a portion of the overall channel bandwidth at any given time. On the other hand, if B_{co} is large as compared to the bandwidth of the transmitted signal, the channel fading thereby affects all frequencies in the signal equally and is characterized as *frequency-nonselective* or in simpler term *flat*. When T_{co} of the radio channel is short as compared to the symbol duration of the modulated signal, for example less than 10% of

the symbol duration [34], the rate at which channel characteristics change is higher than the modulated symbol rate. In this case, the small-scale fading effect of the channel is categorized as *fast fading*. Conversely, if T_{co} is long as compared to a symbol duration, the small-scale fading effect is categorized as *slow fading*.

In the IS-95 systems, the transmitted signal is modulated and spread to a signal with a large bandwidth of 1.2288 MHz [4], which is typically larger than the coherence bandwidth of the multipath channel. This is especially true for urban environments as suggested by the delay spread values in Table 3.2. The symbol rate in the IS-95 systems is often higher than the rate at which the mobile radio channel characteristics change. In this regard, the IS-95 mobile radio channel can be effectively categorized as being a *frequency selective* and *slow fading* communication channel. The *frequency selective* nature of the IS-95 CDMA signals makes it well matched to the multipath channel, as will be reviewed in Chapter 4.

3.3.2 Small-Scale Fading: Statistical Distribution Model

The problem of obtaining the statistical distribution of the fading signal amplitude coincides with the random phasor problem [38]. In an urban environment there is rarely a LOS transmission path, the small-scale fading of the channel is usually modelled by the so called Rayleigh fading, with its Probability Density Function (PDF) given by [34][38]:

$$P(m) = \begin{cases} \frac{m}{\sigma^2} \exp\left[-\frac{m^2}{2\sigma^2}\right] & (0 \leq m \leq \infty) \\ 0 & (m < 0) \end{cases} \quad (3.2)$$

where m is the instantaneous signal amplitude and σ is the Root Mean Squared (RMS) value of the received signal and σ^2 is the time-average power of the received signal. The PDF of the phase of a Rayleigh faded signal follows a uniform distribution over $[0, 2\pi)$ [34]. With Rayleigh fading, the received signal power may vary by as much as three or four orders of magnitude (30 or 40 dB) when the receiver moves even by small distances [39]. In this thesis, we will use the Rayleigh distribution to model the small-scale fading effect of the mobile radio channel.

3.4 IS-95 Multipath Power Profile and Signal Scattering

In narrow band transmissions where the multipath delay spread is much smaller than the resolution of the receiver which is equal to the reciprocal of the channel bandwidth, paths are not resolvable to the receiver. In this case, the single-path assumption is adopted. However, the delay spread in urban environments could be as long as $4 \mu\text{s}$, as indicated in Table 3.2. This corresponds to a duration of 5 chip periods in the IS-95 systems [4]. The effect is the wide-band transmission in which as many as 5 multipath signals appear at the IS-95 receiver. In order to facilitate analysis and simulation, sometimes a simplified power profile model in which these 5 multipaths have the same average power density is assumed, e.g. [40]. This is generally not true as each multipath is the result of different reflections of the transmitted signal superimposing on one another which have different time delays (therefore different phases) and signal powers.

In this section, we define the extended IS-95 CDMA Multipath Channel Model (CMCM) that we have developed in the research of this thesis. This CMCM is a new and more accurate approach to model the response of the IS-95 wide-band channel in terms of power delay profile and the multipath signal scattering in the environment. In Section 3.4.1, we describe the Hashemi

Multipath Channel Model (HMCM) [22][41] for the characterizations and modelling of the radio channel impulse response. In Section 3.4.2, the Geometrically Based Circular Model (GBCM) [15], which simulates the multipath signal scattering in a macrocell environment, is presented. In Section 3.4.3, we define the CMCM based upon the previously described HMCM and GBCM, and discuss appropriate procedures to generate multipath power profiles and AOA's for the multipath components in our capacity simulations.

3.4.1 Hashemi Multipath Channel Model (HMCM)

Back in 1977, Hashemi performed a thorough simulation of the urban radio propagation characterization in his Ph.D thesis research [41] and this resulted in the so-called Hashemi Multipath Channel Model (HMCM) [22]. The channel model used is the one originally suggested by Turin [42] in which the multipath channel is modelled as a linear filter with the complex-valued impulse response, $h(t)$, which can be mathematically expressed as

$$h(t) = \sum_k a_k \delta(t - t_k) e^{j\theta_k} \quad (3.3)$$

where the propagation medium is characterized by a set of theoretically infinite multipath components with amplitudes $\{a_k\}$, arrival times $\{t_k\}$ and phases $\{\theta_k\}$. This is a wide-band channel model which has the advantage that, because of its generality, it can be used for obtaining the response of the radio channel to the transmission of any signal $s(t)$ by convoluting $s(t)$ with $h(t)$.

In Hashemi's experiments, it is assumed that the signal phase $\{\theta_k\}$ is uniformly distributed over $[0, 2\pi)$ because a moderate change in receiver position will result in large enough phase vari-

ations to make the phases uncorrelated. Short pulses having half power width of 100 ns were transmitted at a fixed site and a mobile van equipped with an oscilloscope was driven around certain geographical areas. Samples of the envelopes of the channel impulse response were recorded in the form of photographs from the oscilloscope displays. The measurements were carried out at three carrier frequencies, namely 488 MHz, 1280 MHz and 2920 MHz, and for four geographical areas around the San Francisco Bay area with various degrees of urbanization as follows:

- A heavily built up area (downtown San Francisco)
- The downtown of a medium size city (downtown Oakland)
- The downtown of a small to medium size town (downtown Berkeley)
- The residential suburbs of a city (residential Berkeley)

For each frequency and geographical area, a total of 1000 frames of data were recorded, where each frame of data contains the samples of the received pulse envelopes for the same profile. The recorded photographs of the oscilloscope displays were later reduced on optical scanning tables and a series of $\{a_k, t_k\}$ pairs were obtained for each profile. The statistical properties of the arrival time sequence $\{t_k\}$ and the amplitude sequence $\{a_k\}$ were analyzed and derived based upon these extensive experimental measurements.

3.4.1.1 Temporal and Spatial Correlations

In the HMCM, two distinct types of correlations are considered: temporal correlations and spatial correlations. Due to the grouping properties of signal reflectors and scatterers in an urban environment, multipaths of the same signal exhibit strong correlations in their arrival times and amplitudes. This type of correlation among multipaths of the same mobile radio channel is termed

as *temporal* correlation. For closely located receiving antennas¹, the channel impulse response at each receiver also exhibits significant correlations because the principle reflectors and scatterers in the environment which result in the multipath condition would be approximately the same. This type of correlation among the different mobile radio channels is called *spatial* correlation.

The IS-95 systems considered in this thesis operate in the 800-900 MHz range. This corresponds to $\lambda \approx 0.35$ m, which is significantly shorter than the average separation between typical outdoor mobile users in a cellular network. Thus, we will neglect the spatial correlations among the mobile radio channels for the purpose of simulating the multipath channels in this thesis. All the equations used later on in this chapter to describe the HMCM have been modified to exclude spatial correlations.

Using this simplified HMCM, the arrival times, signal amplitudes and phases of the multipaths for the wide-band radio channel can be predicted based upon their statistical properties. For the remaining of this section, we will present the HMCM by describing the methodology for generating in our simulations the arrival times, amplitudes and phases of the multipath signals.

3.4.1.2 Generation of Arrival Times

If a LOS path exists, the signal in this path is the first to arrive at the receiver because of its shortest distance. In a first-order approximation [22], it is assumed that the scattering objects in an urban area are located randomly in space, giving rise to a Poisson distribution for the arrival times in which the excess delay sequence $\{t_k - t_o\}$ follows a Poisson distribution, where t_o is the LOS path delay. Turin [35] established the inadequacy of the Poisson distribution hypothesis to

¹ The distance between these antennas is approximately one wavelength.

describe the arrival times.

A second-order model was employed in the HMCM where the arrival times are approximated by a modified Poisson process (the so called $\Delta - K$ model [35][43]), which takes into account the possibility of multipath signals arriving in groups since the buildings that result in the multipath reflections are usually located in groups. It divides the time axis into intervals of 100 ns duration (so called "bins"), with the origin at the LOS path delay. For the $\Delta - K$ model, the probability, P_i , of having a path in bin i ($i \geq 1$) is given by

$$P_i = \begin{cases} \lambda_i & \text{if there was no path in the (i-1)-th bin} \\ K\lambda_i & \text{if there was a path in the (i-1)-th bin} \end{cases} \quad (K > 1) \quad (3.4)$$

where the probability of path occurrences λ_i has the following relationship with the empirical path occurrence probability² r_i :

$$\lambda_i = \begin{cases} r_1 & (i = 1) \\ \frac{r_i}{(K-1)r_{i-1} + 1} & (i > 1). \end{cases} \quad (3.5)$$

Due to the grouping properties of arrival times, it is more likely to have a path in the current bin if there was a path in the previous bin than, if there was no path in the previous bin. Thus, the grouping properties lead to $K > 1$. In Hashemi's analysis, the values of K were determined by using an optimization technique which minimizes the mean square error (MSE) between the experimental measurements and the theoretical model of Eqs. (3.4) and (3.5).

² This is the probability of having a path arrival in the i -th bin and was determined from the arrival times recorded from Hashemi's experiments.

In the model described by Eqs. (3.4) and (3.5), the possibility of having more than one path arrival in the same bin is excluded. Due to the 10 MHz bandwidth limitations of the oscilloscopes used in Hashemi's original experiments, there was a signal resolution of 100 ns: paths arriving within 100 ns would combine and in effect only one single path would be observed. The path arrival generation process for the multipath channel is illustrated in Fig. 3.2. The path arrival times generated using the $\Delta - K$ model will be utilized to generate the corresponding signal amplitudes.

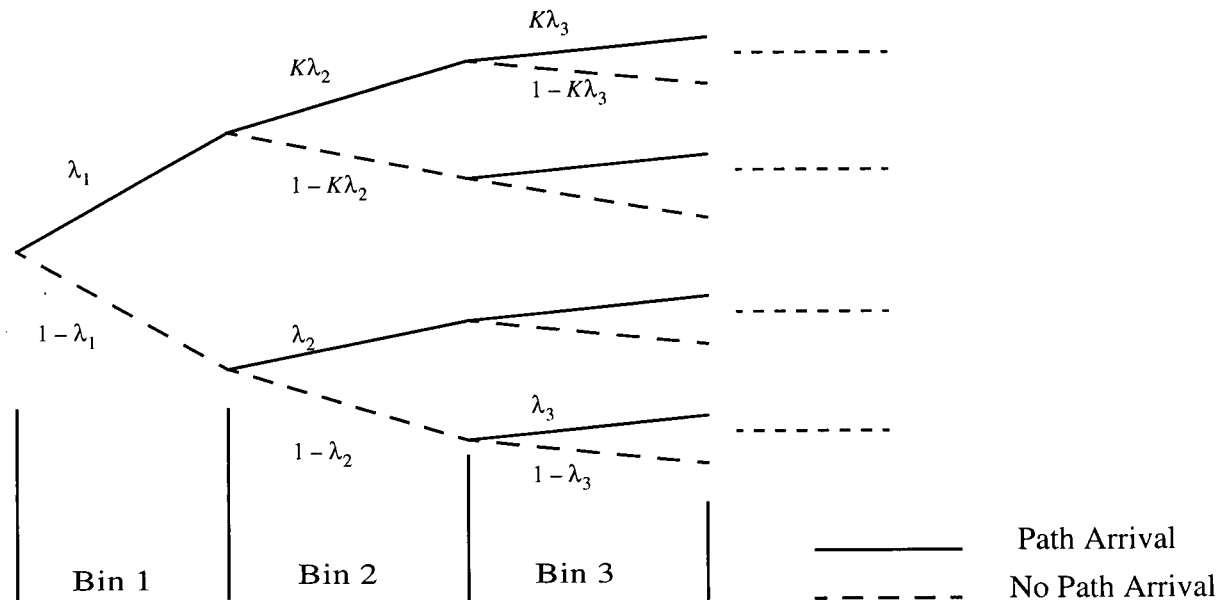


Fig. 3.2 Path Arrival Generation in the HMCH

3.4.1.3 Generation of Signal Amplitudes

Because of the inhomogeneous characteristics of the urban radio channel, the mean and variance of the signal amplitudes as well as the amplitudes themselves are random. The large-

scale fading effects give rise to signal amplitudes that follow log-normal distributions [1][33]. Turin [35] showed that the log-magnitudes of path arrivals in a profile are highly correlated with typical correlation coefficients for adjacent paths between 0.4 and 0.6. In Hashemi's analysis, Turin's findings were adopted. Signal amplitudes are generated according to log-normal distributions, while the mean and variance are approximated with bivariate normal distributions.

In the simplified HMCM, the amplitudes are generated in dB in the following manner. Firstly, the arrival times are generated using the method as previously described in Section 3.4.1.2. Each bin is given the value of 1 if a path exists, and 0 otherwise. An example of bin value assignments is illustrated in Fig. 3.3, in which an arrow represents the presence of a path arrival. In order to generate the amplitudes for all the path arrivals, the mean and variance of the log-amplitude of the path in each bin were determined from the empirical data assuming standard normal distributions. Using the means and variances calculated, the log-amplitude of the first path is generated according to a standard normal distribution. The log-amplitude of the j -th ($j = 2, 3, 4, \dots$) path is then generated according to a conditional normal distribution³, with the mean and variance being conditional on the log-amplitude, x_{j-1} , of the $(j-1)$ -th path arrival, which are mathematically expressed as [22][41]

$$\begin{aligned}\mu'_j &= \mu_j + \rho_{j-1j} \frac{\sigma_j}{\sigma_{j-1}} (x_{j-1} - \mu_{j-1}) \\ \sigma'^2_j &= \sigma_j^2 (1 - \rho_{j-1j}^2)\end{aligned}\tag{3.6}$$

where μ'_j and σ'^2_j are the conditional mean and variance for the j -th path, μ_{j-1} , μ_j and σ_{j-1}^2 ,

³ This is the same as a standard normal distribution, except that its mean and variance are conditional variables.

σ_j^2 are the standard means and variances determined from the empirical data and $\rho_{j-1,j}$ is the coefficient representing the temporal correlations between the $(j-1)$ -th and j -th paths.

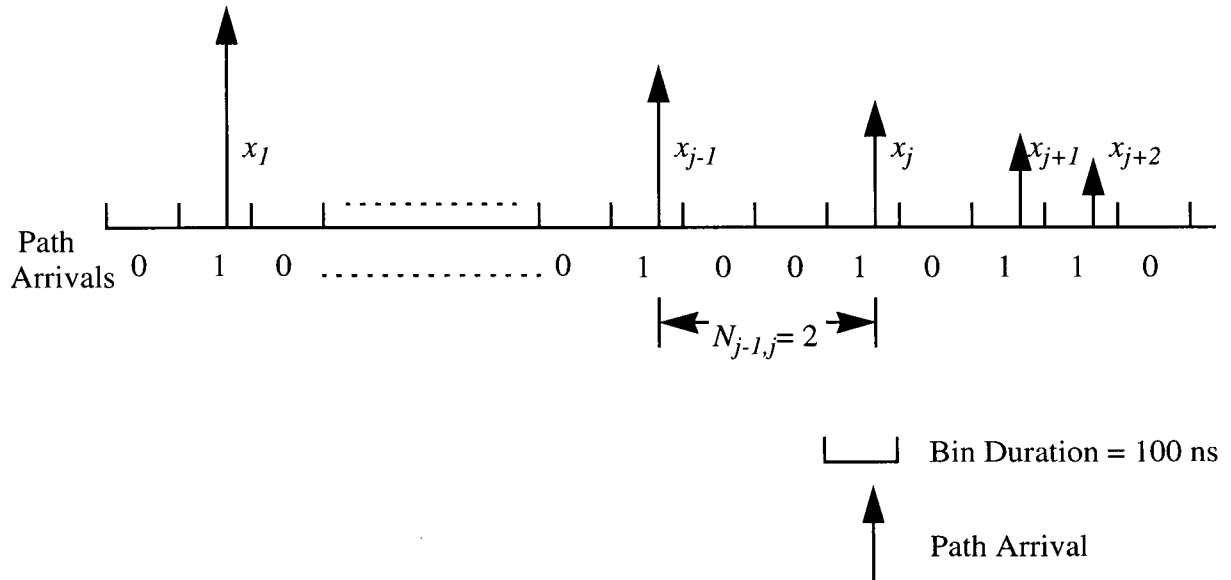


Fig. 3.3 Path Amplitude Generation in the HMCN

In order to account for the decreased temporal correlations for two path arrivals that are farther apart in time, the correlation coefficient $\rho_{j-1,j}$ was made a decreasing function of the difference in arrival times and this can be mathematically expressed as [22]

$$\rho_{j-1,j} = \exp\left(\frac{(-100)(N_{j-1,j} + 1)}{\tau_{j-1,j}}\right) \quad (3.7)$$

where $N_{j-1,j}$ represents the number of 0's, i.e. the number of bins without path arrivals, between the $(j-1)$ -th and j -th paths. For example, $N_{j-1,j} = 2$ in Fig. 3.3. The parameter $\tau_{j-1,j}$ is a variable used in the simulation in order to derive the appropriate values for $\rho_{j-1,j}$. This parameter was

obtained by starting with a reasonable value and changing it repeatedly in the simulation program until a desirable temporal correlation coefficient, $\rho_{j-1,j}$, was found by matching the experimental and simulation distributions.

The procedure to generate a power profile for the multipath channel in the HMCM involves two steps. The first step is to generate the arrival times as previously described in Section 3.4.1.2. Then the corresponding path amplitudes are generated as follows: start with the first path arrival and recursively repeat the method described above for simulating the amplitudes, until the amplitude of the last path is generated.

3.4.1.4 Generation of Signal Phases

In the HMCM, there is a minimum difference in arrival times equal to the duration of a bin (100 ns) between the path arrivals, which corresponds to a difference in propagation distance of 30 meters. At the three carrier frequencies (the worst case is the frequency of 488 MHz employed in Hashemi's experiment, which corresponds to a signal wavelength $\lambda \approx 0.6$ m), 30-meter difference in propagation distance corresponds to many folds of λ .

Since signal phase is critically sensitive to the propagation distance and changes by 2π as the distance changes by λ , the variations in the path propagation lengths in the HMCM is large enough to make the phases essentially uncorrelated. Therefore, the sequences of signal phases are generated according to an independent uniform distribution over $[0, 2\pi)$.

3.4.2 Geometrically Based Circular Model (GBCM)

For a receiver whose antenna design has a non-omnidirectional gain pattern, the AOA of

each multipath arrival can have a great impact on the overall received signal strength. In an urban macrocell environment it is usually assumed that the MS is surrounded by scatterers in proximity and its height is far lower than those of the scatterers. This implies that the received signals at the MS may arrive from all directions after bouncing off from the surrounding scatterers, as illustrated in Fig. 3.4. Therefore it is reasonable to assume that, in a macrocell environment, the AOA at the MS is uniformly distributed over $[0, 2\pi)$.

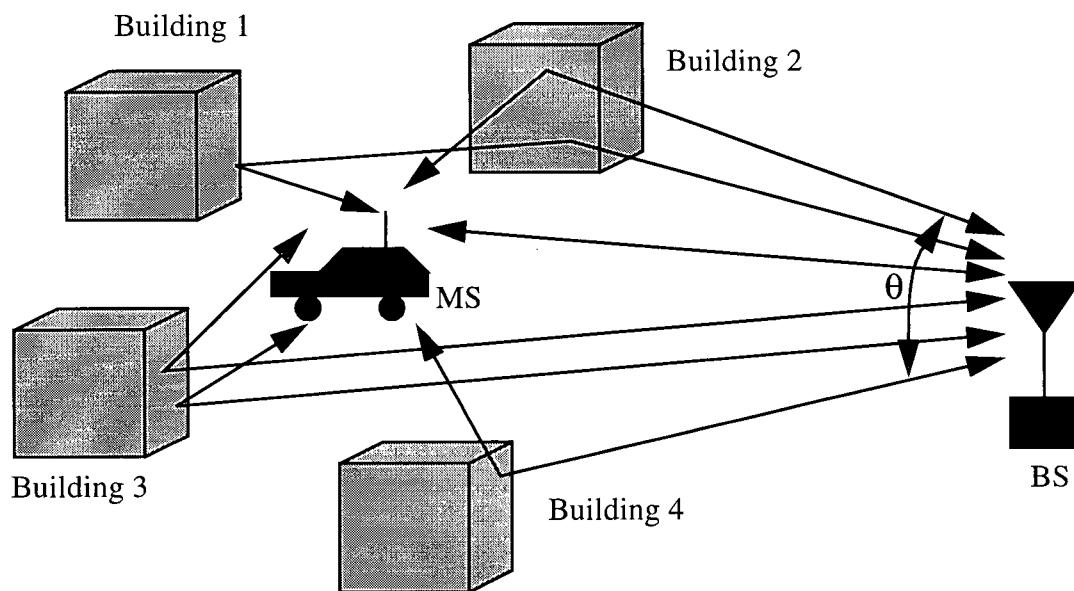


Fig. 3.4 Macrocell Multipath Propagation Environment

On the other hand, the geometrical characteristics of the AOAs of the received signals at the BS are quite different from the MS case. The BS is typically placed on a tower or building much higher than the surrounding scattering objects. Hence, as illustrated in Fig. 3.4, the received multipath signals at the BS result from the reflections of the scatterers surrounding the MS in the far field. The AOAs of the multipath components arriving at the BS are no longer uniformly

distributed on $[0, 2\pi)$, but typically restricted to a small angular spread θ [12]. Measurements reported in [44] suggest that the typical angular spreads for macrocell environments with a MS-BS separation of 1 km are approximately between 4° and 12° and are inversely proportional to the MS-BS separation.

The GBCM [15][12] is a spatial channel model that can be used to simulate the random signal AOA in an urban macrocell environment. Given the number of multipath components and the locations of the BS and MS, the GBCM can be utilized to generate the corresponding AOA for each multipath. It assumes that all the scatterers are constrained and uniformly distributed inside a “scattering circle” of radius R_m around the MS, as illustrated in Fig. 3.5. In the figure, the distance between the BS and MS is denoted as L . The idea of a circular scattering region around the MS was originally studied by Jakes [37] to investigate the correlation between the received signals of two antenna sensors. Measurements reported in [15] suggest that, in a macrocell environment, the radius of the scattering circle ranges from 30 to 200 meters.

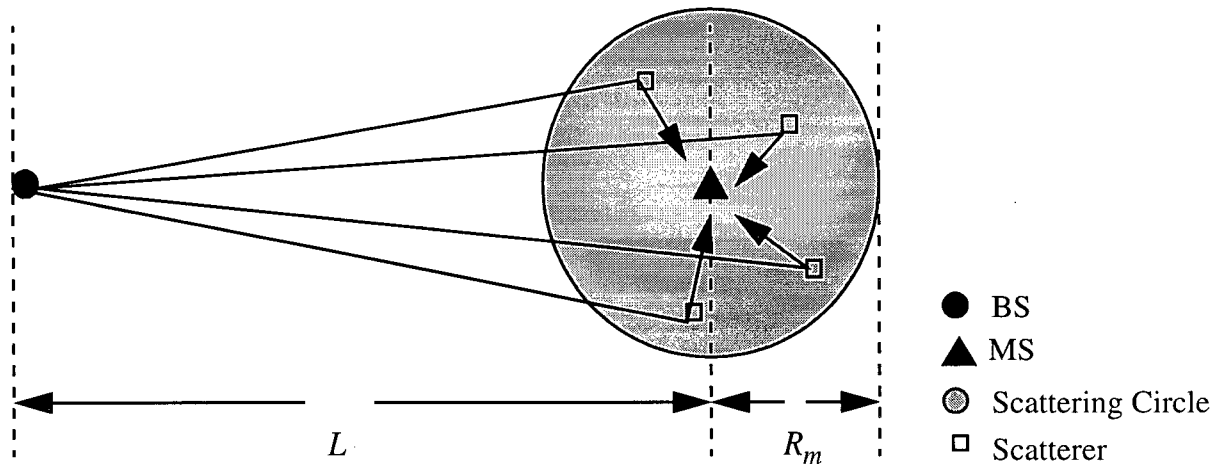


Fig. 3.5 Geometrically Based Circular Model I

In the case where the MS is very close to the BS (i.e. $R_m > L$), the AOAs of the multipath components are no longer confined to an angular region, but tend to be uniformly distributed over $[0, 2\pi)$. This situation is illustrated in Fig. 3.6.

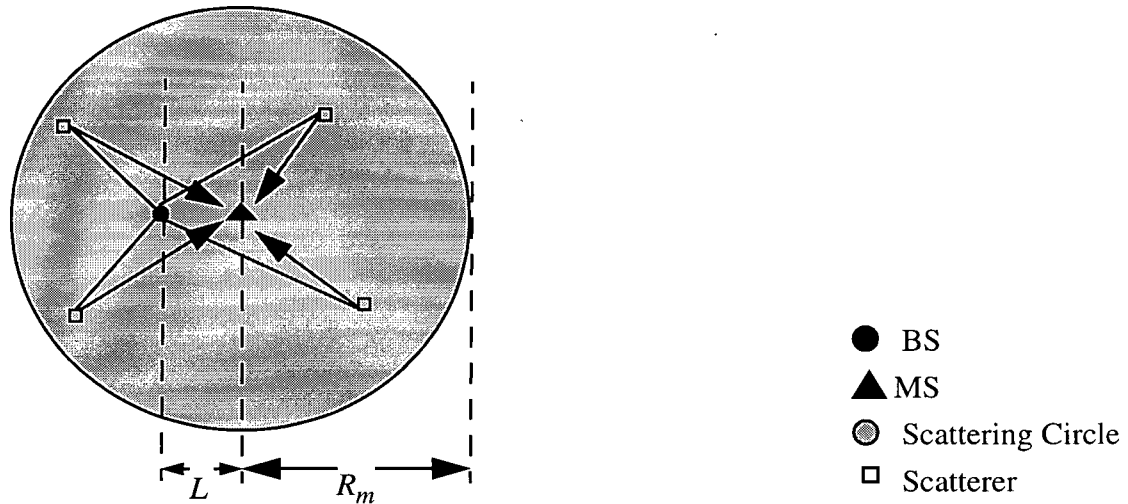


Fig. 3.6 Geometrically Based Circular Model II

3.4.3 Extended IS-95 CDMA Multipath Channel Model (CMCM)

The HMCM defines a highly accurate statistical model to simulate the impulse response of the wide-band radio channel based upon extensive empirical data collected from experiments. Hashemi established the validity of the HMCM by generating extensive sets of time arrivals and the corresponding signal amplitudes using his simulation program. The probability of observing a path in a bin and the mean and variance of the log-amplitudes of the bin paths were compared with the experimental results. The match was found to be almost perfect [41].

For the remaining of this section, we will describe the CMCM we have developed in our research by extending the HMCM specifically for the IS-95 wide-band channels. The CMCM is

employed in our capacity simulations to generate the resolvable multipath signals separated by an IS-95 chip period. For the multipath signals generated, a slightly modified version of the GBCM is further utilized to generate the corresponding AOAs. Forming its foundation on two widely accepted models which were originally developed on extensive experimental results, the CMCM can accurately simulate the multipath conditions of the IS-95 radio channels.

First, we have obtained from [41] the experimental results of the arrival times and the signal amplitudes recorded in Hashemi's experiments for the four simulated areas. We implemented the Simplified HMC simulation Program (SHSP) in software according to the model as previously described in Section 3.4.1. The SHSP was used to produce a large set of arrival times and path amplitudes. The statistics of the probability of bin path arrivals and the mean and variance of path log-amplitudes were calculated and compared with the experimental results⁴ in order to verify the correctness of the SHSP software. With a good match found between the simulated data and experimental results, an extrapolation in carrier frequencies of 488 MHz and 1280 MHz was performed so that the SHSP is able to produce multipath signals at a frequency of 850 MHz for the IS-95 systems. This was done by employing linear extrapolation techniques on the statistical parameters in Eqs. (3.4)-(3.7) based upon the experimental results collected by Hashemi for 488 MHz and 1280 MHz.

In order to include in the CMCM both urban and suburban environments, we have chosen to consider a multipath delay spread of 4 μ s, as suggested in Table 3.2. Since the IS-95 CDMA channel is frequency-selective, as previously explained in Section 3.3.1, it can be modelled by a

⁴ Since we exclude *spatial* correlation in the simplified HMC, the experimental results compared were those collected from well spatially separated locations .

tapped delay line with a set of statistical independent time-variant tap weights $\{C_n(t); n = 0, 1, 2, 3, 4\}$, as illustrated in Fig. 3.7. In the figure, the time-variant tap weights $\{C_n(t)\}$ are independent complex-valued stationary random processes with their amplitudes assumed to be Rayleigh distributed. $1/W$ is the chip period ($0.8 \mu\text{s}$ [4]), where W is the bandwidth of the modulated IS-95 CDMA signals. In the tapped delay line model, multipath signals arriving at the IS-95 receiver separated by more than a chip period can be resolved and thus provide multiple versions of the transmitted signal [32][45]. On the other hand, multipath signals within the same chip, due to the slow fading characteristics of the IS-95 channel, experience the same Rayleigh fading and appear to the IS-95 CDMA receiver as a single signal which is equal to the vectorial combination of the individual components.

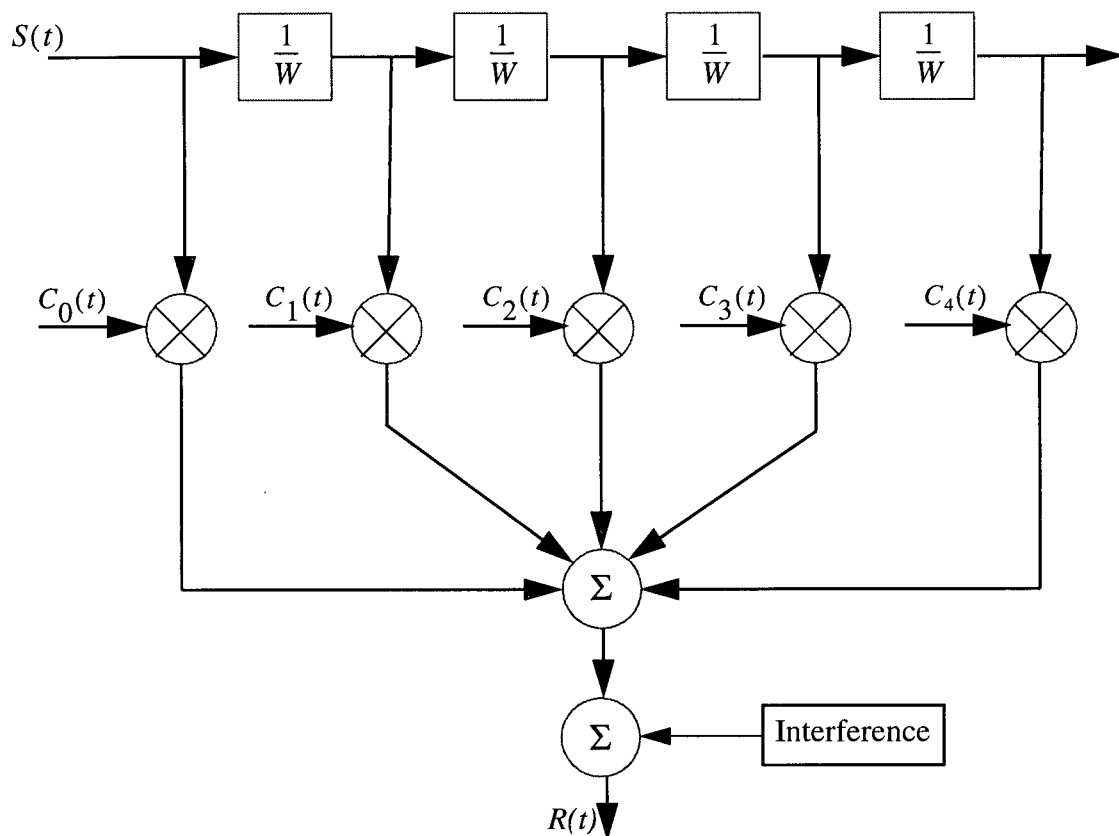


Fig. 3.7 Tapped Delay Line Model for Frequency Selective Fading Channel

To produce resolvable multipath signals in the CMCM for our capacity simulations, the SHSP is used to generate path arrivals for the delay spread of 4 μ s, which is the duration of 40 bins. Each generated path has its arrival time, signal amplitude and phase, and can be mathematically expressed as $a_i e^{j\theta_i}$, where a_i denotes the amplitude and is equal to 0 if there is no path arrival, θ_i is the signal phase and i is the bin index ($i = 1, 2, 3, \dots, 40$). The power density of the multipath component for each of the 5 chip periods is obtained by squaring the vector sum of all the paths generated for the 8 bins inside the chip and is given by

$$P_j = \left| a_{8j+1} e^{j\theta_{8j+1}} + a_{8j+2} e^{j\theta_{8j+2}} + a_{8j+3} e^{j\theta_{8j+3}} + \dots + a_{8j+8} e^{j\theta_{8j+8}} \right|^2 \quad (3.8)$$

where j is the chip index and $j = 0, 1, 2, 3, 4$. Note that P_j takes a value of 0 when there is no path arrival in every bin inside the j -th chip period, which indicates the absence of a multipath signal inside the j -th chip period. Finally, the values of P_j are normalized such that $P_0 + P_1 + P_2 + P_3 + P_4 = 1$. The vectorial combining of the bin path arrivals to form the multipath component in each chip period is illustrated in Fig. 3.8.

With knowledge of the locations of the MS and BS, the GBCM⁵ is employed to generate the AOA for each multipath component produced. For the cases of downtown and residential Berkeley, a slight modification was made to the GBCM in which the AOA of the multipath component of the largest power density is assigned the angle of the LOS path, assuming that such a path always exists in these two suburban areas. In our capacity simulations, the method described above is repeated for each IS-95 radio channel until the last profile is generated. In Fig.

⁵ In order to represent a large scattering region, we have used $R_m = 0.2$ km (see Figs. 3.5 and 3.6).

3.9, the procedures to generate multipath power profiles using CMCM are illustrated.

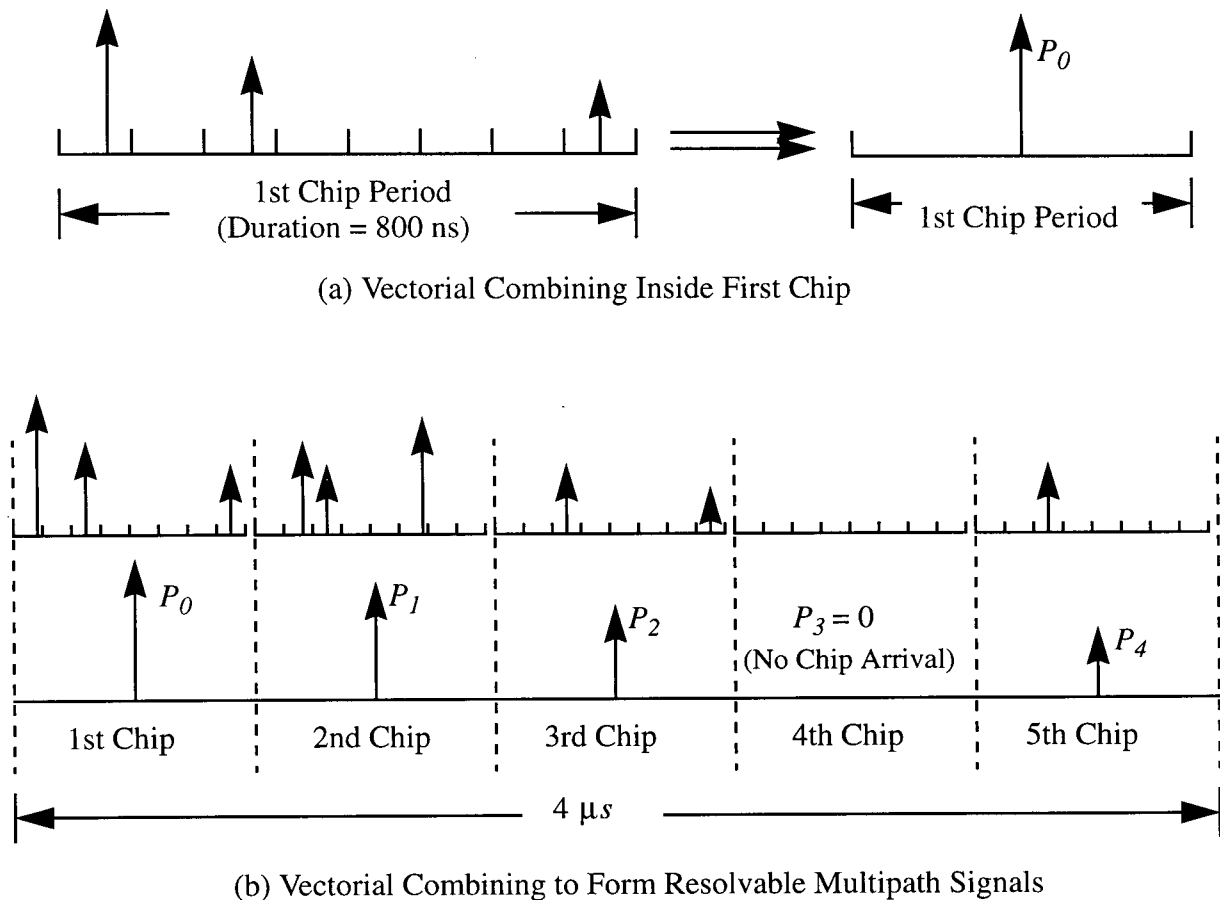


Fig. 3.8 Vectorial Combining of Bins to Generate IS-95 Multipath Signals

Tables 3.3 and 3.4 list a sample of 15 random power profiles generated using the CMCM simulation program for downtown San Francisco and residential Berkeley, respectively. Downtown San Francisco represents a heavily urban environment in which, due to the high density of large buildings, signals usually get reflected many times before arriving at the receiver, resulting in large delay spreads and a strong multipath phenomenon. Conversely, residential Berkeley represents a typical suburban area in which, due to the absence of large building

structures, a LOS path usually exists, giving rise to relatively short delay spreads.

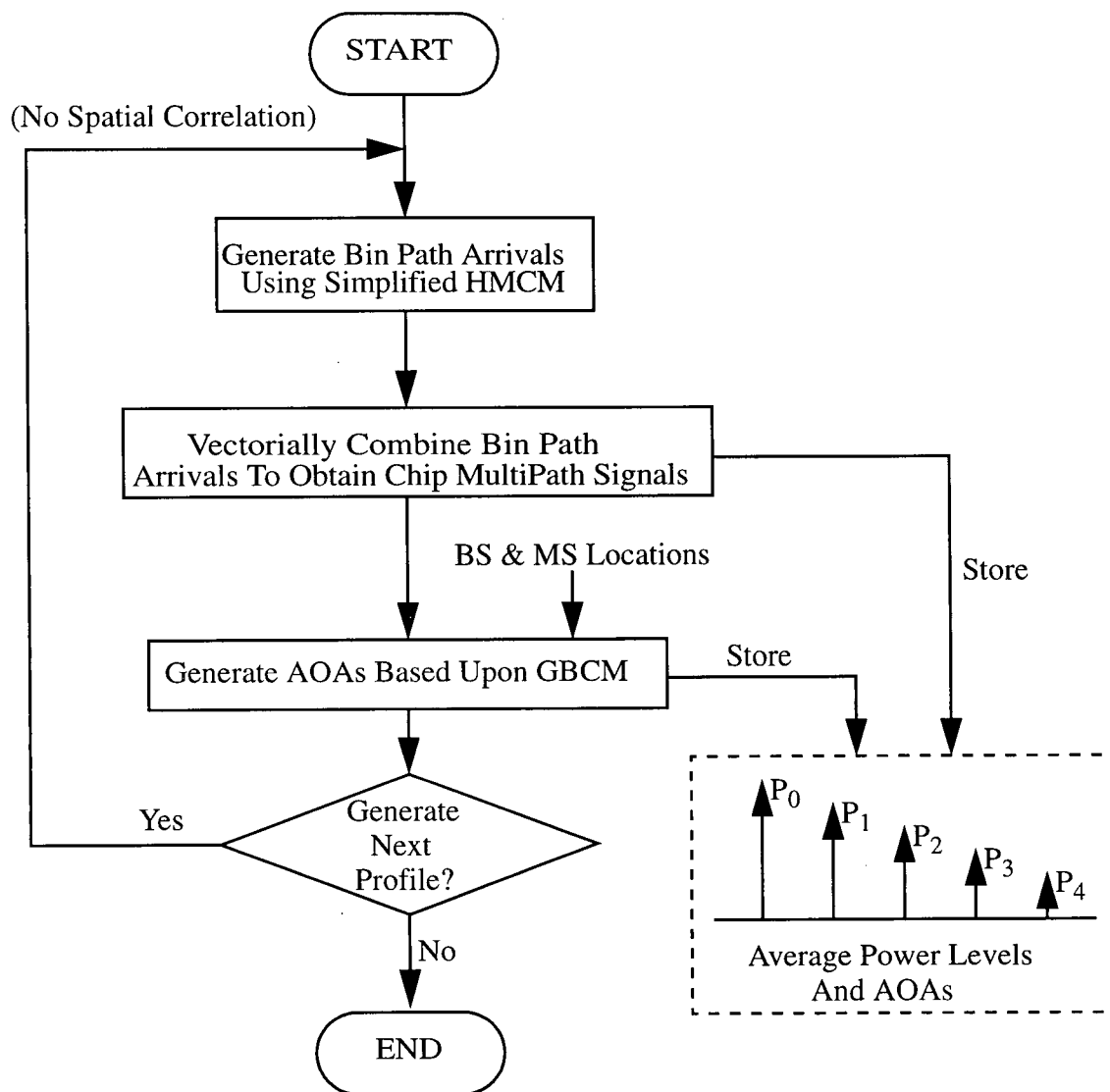


Fig. 3.9 IS-95 Multipath Power Profile Generation in the CMCM

The sample power profiles for downtown San Francisco in Table 3.3 suggest that the large majority of signal power is usually distributed over two or three multipath components at the IS-95 CDMA receiver during the first three chip periods (2.4 μ s), with multipath components in the

4th and 5th chip periods carrying only a small percentage of the total signal power. On the contrary, power profiles for residential Berkeley in Table 3.4 usually include a strong LOS path arrival carrying more than 95% of the total signal power in the first chip (0.8 μ s), while multipath components in the 4th or 5th chip are usually absent. The sample power profiles of these two areas clearly demonstrate the different multipath conditions for urban and suburban environments. In Appendix A, a sample of 30 power profiles produced using the CMCM software program for each of the four simulated areas is listed.

Profile Index	P_0	P_1	P_2	P_3	P_4
1	0.387700	0.411980	0.033376	0.154204	0.012740
2	0.012158	0.550599	0.428711	0.000538	0.007993
3	0.445239	0.553779	0.000023	0.000569	0.000390
4	0.794709	0.202732	0.002232	0.000275	0.000052
5	0.005825	0.000013	0.989615	0.003901	0.000645
6	0.184931	0.785534	0.011032	0.013554	0.004949
7	0.019693	0.245931	0.428533	0.301920	0.003924
8	0.000000	0.491405	0.429800	0.063614	0.015181
9	0.453722	0.250043	0.099600	0.181161	0.015473
10	0.292867	0.320293	0.003560	0.018367	0.364913
11	0.000000	0.757083	0.124464	0.093504	0.024949
12	0.167354	0.828988	0.002539	0.000433	0.000687
13	0.025033	0.869325	0.099302	0.005868	0.000472
14	0.039429	0.387406	0.538707	0.014654	0.019804
15	0.001096	0.050976	0.807589	0.139336	0.001004

Table 3.3 Sample Power Profiles For Downtown San Francisco

Profile Index	P_0	P_1	P_2	P_3	P_4
1	0.999985	0.000015	0.000000	0.000000	0.000000
2	0.141830	0.856831	0.001229	0.000080	0.000031
3	1.000000	0.000000	0.000000	0.000000	0.000000
4	0.999897	0.000085	0.000018	0.000000	0.000000
5	0.998895	0.001105	0.000000	0.000000	0.000000
6	0.000000	0.999247	0.000753	0.000000	0.000000
7	0.999892	0.000104	0.000004	0.000000	0.000000
8	0.737902	0.262075	0.000023	0.000000	0.000000
9	0.962433	0.037288	0.000279	0.000000	0.000000
10	0.931004	0.068844	0.000152	0.000000	0.000000
11	0.999999	0.000001	0.000000	0.000000	0.000000
12	0.999967	0.000033	0.000000	0.000000	0.000000
13	0.999930	0.000066	0.000003	0.000000	0.000000
14	0.899572	0.100346	0.000083	0.000000	0.000000
15	0.999275	0.000725	0.000000	0.000000	0.000000

Table 3.4 Sample Power Profiles For Residential Berkeley

3.5 Conclusions

In this chapter, we have described the important parameters to account for the multipath conditions of the IS-95 CDMA channels. The large-scale fading has been described for propagation loss and log-normal shadowing. The inverse power law is adopted in our propagation loss model and a standard deviation of 8 dB is assumed for log-normal shadowing. We have used the Rayleigh distribution to model the small-fading effects. In order to accurately simulate the power distributions among the resolvable multipaths at the IS-95 receiver, the frequency selective channel is represented with a tapped delay line model. The CMCM has been developed based upon the

simplified HMCM excluding spatial correlations. To include in the CMCM both urban and suburban environments, the multipath channel response is simulated for four geographical areas, namely downtown San Francisco, downtown Oakland, downtown Berkeley and residential Berkeley. A slightly modified version of the GBCM is employed as the scattering model to predict the AOAs for the multipath signals generated using the CMCM. Finally, sample power profiles for the simulated areas have been presented and compared for their different multipath characteristics.

Chapter 4 IS-95 BER PERFORMANCE MODEL

4.1 Introduction

The IS-95 CDMA spread spectrum signal waveform is well matched to the multipath radio channel. The IS-95 mobile radio channel, being frequency selective, usually results in several resolvable multipaths of the transmitted signal which can be exploited by the RAKE receiver to construct a stronger combined signal. On the other hand, the performance of the RAKE receiver is heavily dependent upon the distributions of the power density among the multipath signals and their individual fading characteristics. The purpose of this chapter is to establish an accurate BER performance model for the IS-95 RAKE receivers in multipath Rayleigh faded channels which will be used in our capacity simulations. The effects of the multipath power distributions, i.e. the power profiles, on the IS-95 BER performance are simulated for an average BER of 10^{-3} in order to maintain satisfactory voice and data call quality [1][3].

The organization of this chapter is as follows. After this introduction, in Section 4.2, we first present an overview of the Direct Sequence Spread Spectrum (DS-SS) technology used in the IS-95 systems. Section 4.3 describes the downlink and uplink system architectures of the IS-95 air interface, focusing on the traffic channel structures which are essential for our IS-95 BER performance simulations. In Section 4.4, we explain the diversity combining mechanisms of the IS-95 RAKE receiver, with discussions of coherent combining in the downlink and non-coherent combining in the uplink. In Section 4.5, the IS-95 BER performance model for the multipath Rayleigh faded channels is defined and the corresponding BER simulation results are presented. Finally, the conclusions of this chapter are given in Section 4.6.

4.2 Direct Sequence CDMA

A fundamental issue in Direct Sequence CDMA (DS/CDMA) systems, such as the IS-95, is how the user signals are separated from interference with finite power. In this section, we briefly review the basic concepts of DS/CDMA and present an overview of the spreading of information signals using the pseudorandom (PN) sequences.

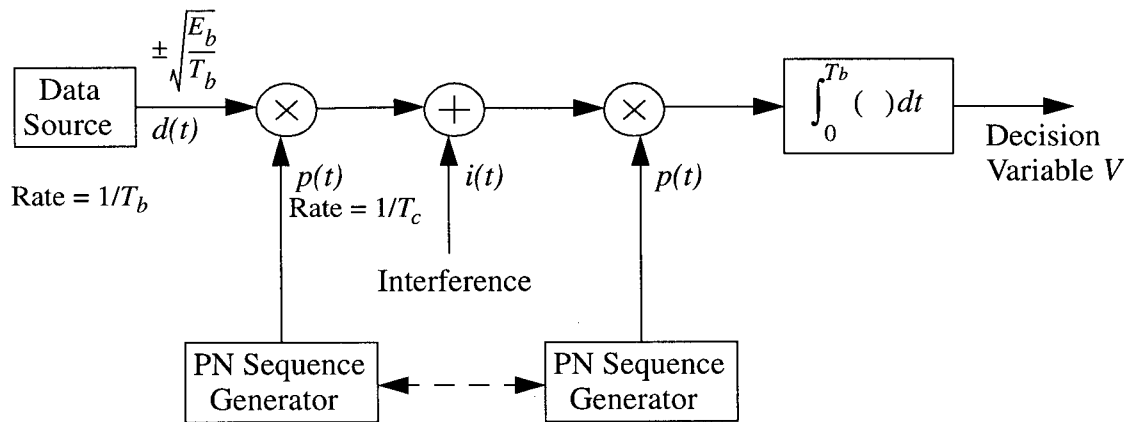


Fig. 4.1 Baseband DS/CDMA System

The basic elements of a DS/CDMA system are shown in Fig. 4.1. A single bit $\pm \sqrt{\frac{E_b}{T_b}}$ of the data source $d(t)$ is transmitted with energy E_b of duration T_b seconds. The transmitter multiplies the data bit $d(t)$ with a binary ± 1 PN sequence $p(t)$ chosen randomly with a period of T_c seconds, as illustrated in Fig. 4.2. In order to spread the information signals, the PN chip period T_c is usually several orders of magnitude smaller than the data bit period T_b [34]. The PN sequences have “random like” properties, but are produced in a deterministic manner using shift registers [34][36]. The received signal is given by

$$r(t) = d(t)p(t) + i(t) \quad (4.1)$$

where $i(t)$ is the interference plus white noise. The receiver, assuming knowledge of the PN sequence, performs the correlation

$$U = \int_0^T r(t)p(t)dt \quad (4.2)$$

and makes a decision whether $\pm \sqrt{\frac{E_b}{T_b}}$ was sent depending upon $U \geq 0$ or $U < 0$. The integral in Eq. (4.2) can be expanded as

$$r(t)p(t) = d(t)p^2(t) + i(t)p(t) = d(t) + i(t)p(t) . \quad (4.3)$$

Hence the data bit decision is made in the presence of the code modulated interference $i(t)p(t)$.

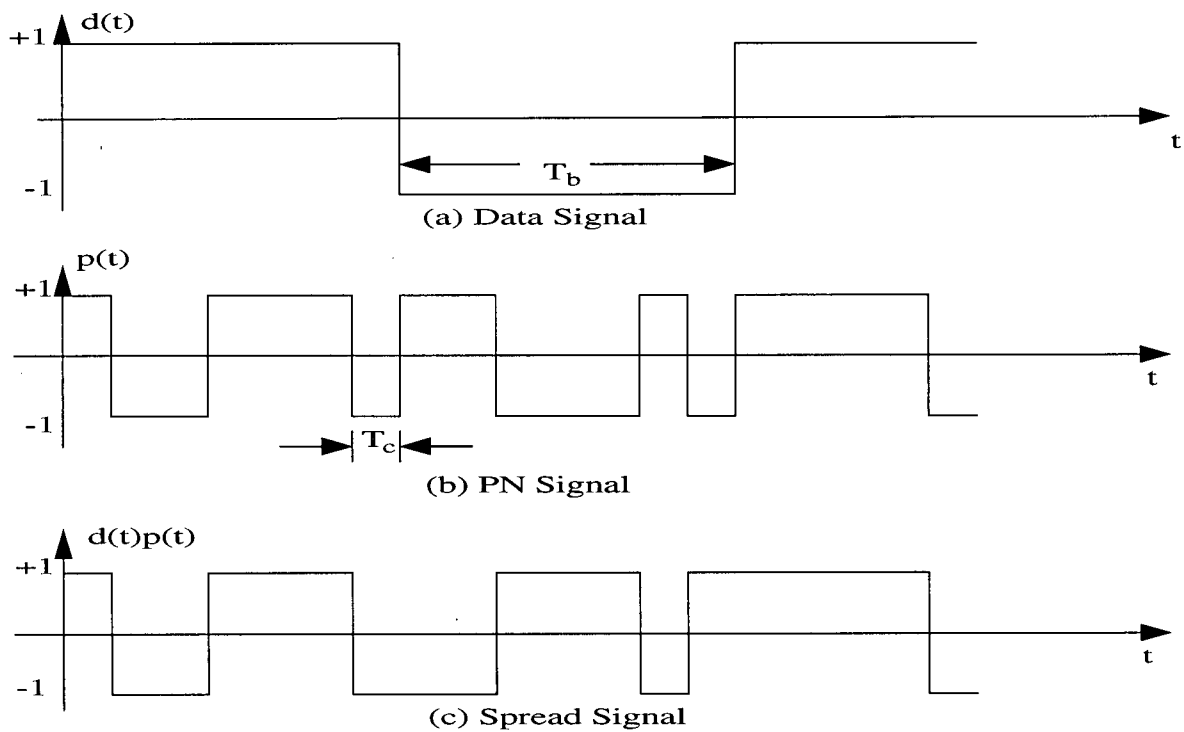


Fig. 4.2 Signal Spreading in DS/CDMA

The multiplication of the data source $d(t)$ with the PN sequence $p(t)$ serves to spread the signal spectrum. It is well known that the power spectral density of an infinite random data sequence of ± 1 with a period of T seconds is given by [38]

$$S_D(f) = T \left(\frac{\sin(\pi f T)}{\pi f T} \right)^2. \quad (4.4)$$

An example of the power spectra of the random sequences $d(t)$ and $d(t)p(t)$ is illustrated in Fig. 4.3. The data source $d(t)$, whose power spectrum is virtually constrained within the bandwidth $B_D = 1/T_b$ Hz, is spread onto a much wider bandwidth $B_{ss} = 1/T_c$ Hz after being modulated by the PN sequence $p(t)$. At the receiver, the first term $d(t)$ in Eq. (4.3) can be extracted virtually intact with a low-pass filter of bandwidth B_D Hz. The second term $i(t)p(t)$, which is the code modulated interference, remains spread over a bandwidth of B_{ss} Hz. Thus the fraction of power due to the interference is reduced by an amount proportional to B_{ss}/B_D , called the processing gain [1][36]. The processing gain gives substantial power advantage over interference to the user signals and gives DS/CDMA better capacity performance as compared to TDMA and FDMA technologies [1].

4.3 IS-95 Signal Waveform Design

The characteristics of the downlink (BS to MS) and the uplink (MS to BS) of the IS-95 CDMA channels are different. In the downlink, there is only one transmitter and many receivers. It is possible to synchronize the signals from all the users by transmitting a pilot signal with high power, thus coherent modulation is appropriate. In the uplink, there are many transmitters and only one receiver. Synchronization of all signals is not feasible as a pilot signal would be required for each channel and power inefficiency would result. Non-coherent modulation is thus employed

in the uplink. The uplink channel is more vulnerable to Multiple Access Interference (MAI) compared with the downlink, thus more robust Forward Error Correction (FEC) techniques must be implemented.

In this section, we describe the IS-95 channel structure with focus on the signal waveform design, which lays the foundation for our BER performance simulation. Major design elements such as channelization, spreading scheme, FEC encoding and modulation techniques are also briefly explained. In the following subsections, the downlink and uplink channel structures are presented separately.

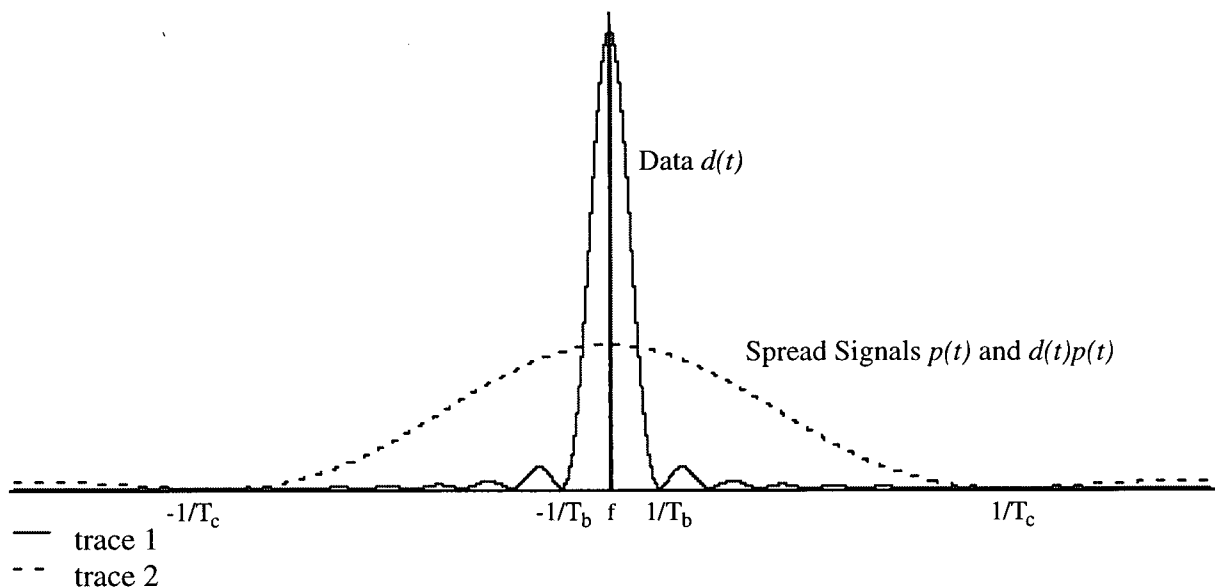


Fig. 4.3 Power Spectra of Data and Spread Signals

4.3.1 IS-95 Downlink Channel Structure

Traffic channels deliver user traffic and user-specific signalling data. The IS-95 downlink traffic channel supports four distinct data rates including 1.2, 2.4, 4.8 and 9.6 kbps [4]. This is to

take advantage of the periods of time when the voice activity is low and therefore the voice codec rate may be reduced. The signal waveform generation is illustrated in Fig. 4.4.

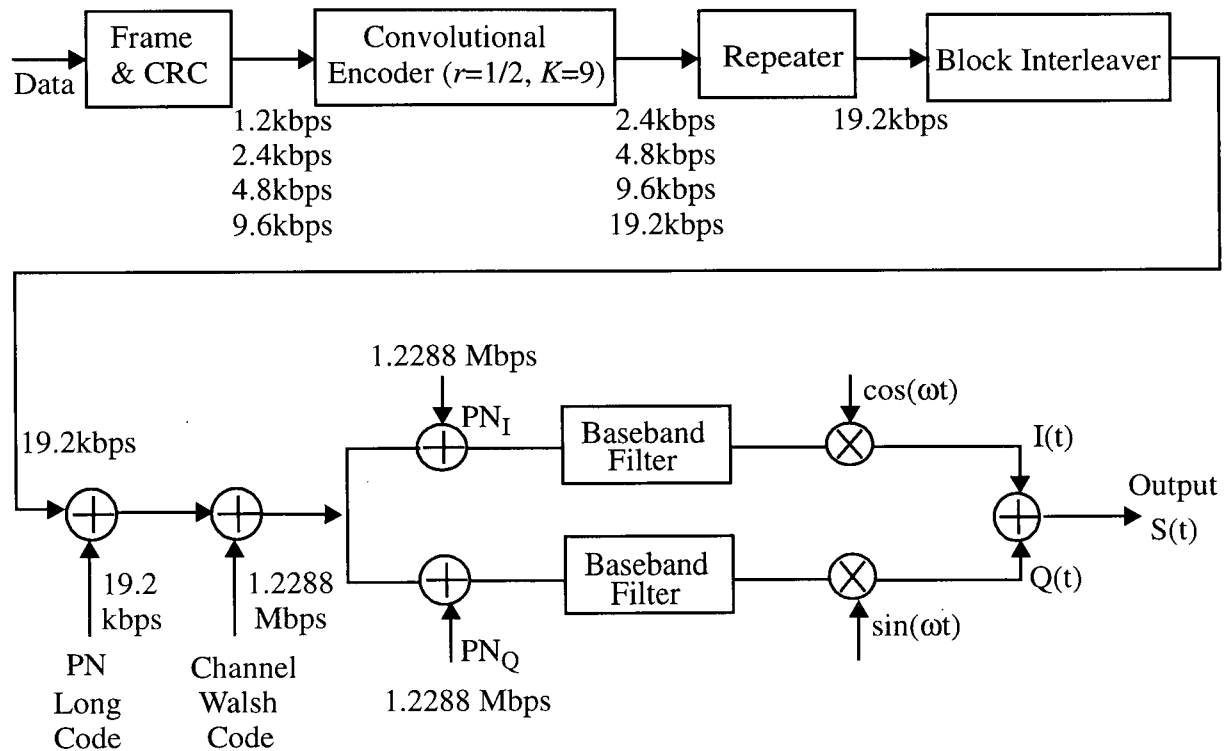


Fig. 4.4 IS-95 Downlink Traffic Channel Waveform Generation

The information bearing bit stream is first formatted by adding frame information and Cyclic Redundancy Check (CRC) bits so that the receiver can use them for error detection. The formatted frame is then encoded using a convolutional encoder of rate $r = 1/2$ and constraint length $K = 9$ [4]. The convolutional encoder, which has a generator function of $g_0 = 753$ (octal) and $g_1 = 561$ (octal) [4], is illustrated in Fig. 4.5. It generates a two bit symbol for every data bit input to the encoder. The output symbol stream of the convolutional encoder is repeated to be 19.2 kbps for bit rates lower than 19.2 kbps. After convolutional encoding and bit repetition, the

code symbols are interleaved by the block interleaver with the span of one data frame (384 bits), which is 20 ms. The interleaving serves to reduce the bursty errors in the mobile radio channels. For the purpose of data security [46], the interleaved symbols are then scrambled using a cell-specific PN long code of 19.2 kbps, which is generated using a linear shift register with a period of $2^{42} - 1$ [4].

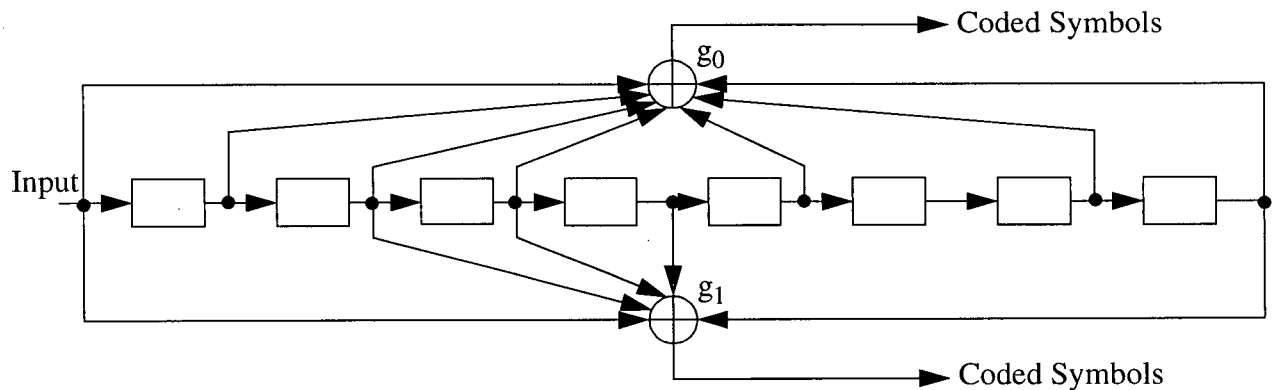


Fig. 4.5 IS-95 Downlink Convolutional Encoder

After the long code scrambling, the code symbols are orthogonally covered with one of the Walsh code sequences of order 64. The Walsh code sequences are completely orthogonal to each other, i.e. the cross-correlations among them are zero. In the absence of multipath, there is zero interference from other users of the same cell due to this code orthogonality [34][46]. Thus the Walsh code sequences are used to separate the signals from different users within a cell. In the presence of multipaths with excess delay of more than a chip period, the uncorrelated channels may contribute an effective interference level in the receiver [46]. However, the interference is significantly reduced due to the available processing gain.

Multiplexed with the Walsh codes, the code symbols are spread in quadrature by a pair of short binary PN code sequences with a period of $2^{15}-1$, PN_I and PN_Q (see Fig. 4.4). The PN_I and PN_Q sequences have different generators and low cross-correlation. The PN chip rate is 1.2288 MHz, which is 128 times the 9.6 kbps data transmission rate. All the BSs share a common pair of quadrature PN sequences, but each BS is assigned a unique time offset to identify itself from other BSs [34]. This relies on the property of the PN codes that the autocorrelation averages to zero for all time offsets greater than a single chip period. All BSs therefore must be tightly coupled to a common time reference. In the IS-95 systems, this is accomplished through the use of the Global Positioning System (GPS), a satellite broadcast system that provides information on the Greenwich Mean time, known as the *system time*. The quadrature spread data streams are finally QPSK modulated on the RF carrier to generate a band limited analog output.

An important element in the IS-95 downlink channel design is the pilot channel. The pilot signal is simply a constant-level signal that is modulo-2 added with the all-zeros Walsh code sequence (channel zero) and continually transmitted in the air interface after quadrature spreading [34]. Every BS uses the same code but a different time offset to identify itself. The MS can obtain synchronization with the BS by searching out the entire length of the PN sequence. The pilot signal is transmitted in the downlink in order to provide a reliable amplitude and phase reference for the coherent demodulation in the receiver. To achieve accurate amplitude and phase tracking, the pilot signal is transmitted with much higher power compared with the user traffic signals. Typically 20% of the radiated power in the downlink is dedicated to the pilot channel [1][3][47]. Unfortunately, the pilot signal also generates significant interference due to its high transmission power. The MS registers with the BS by detecting the pilot tone with the strongest signal power

level [1].

In addition to the pilot channel, there are two other overhead channels in the IS-95 downlink direction, including the synchronization and paging channels [4]. The information transmitted in the synchronization channel enables the MS to acquire timing parameters such as the PN timing offsets of the BS relative to the system time. The paging channel provides system parameters, voice pages, short message services and any other broadcasting messaging to users in the cell.

4.3.2 IS-95 Uplink Channel Structure

Similar to the downlink, the IS-95 uplink traffic channel can support data rates of 1.2, 2.4, 4.8 and 9.6 kbps [4]. In Fig. 4.6, the IS-95 uplink traffic channel waveform generation is illustrated. The formatted data stream is convolutionally encoded using a rate $r = 1/3$, constraint length $K = 9$ convolutional encoder with code generators $g_0 = 557$ (octal), $g_1 = 663$ (octal) and $g_2 = 711$ (octal) [4]. Fig. 4.7 shows the structure of the convolutional encoder employed. It generates a three bit symbol for every data bit input and offers more powerful FEC performance compared with the downlink convolutional encoder in Fig 4.5. The convolutionally encoded data stream is repeated to be 28.8 kbps for bit rates lower than 28.8 kbps. The data is then block interleaved in order to combat bursty errors in the mobile channel.

In the IS-95 uplink, the data stream is modulated with the 64-ary orthogonal modulator in which groups of six-bit code symbols select one of the Walsh sequences of order 64 consisting of 64 bits. Due to the difficulty in obtaining good phase reference for coherent demodulation in the uplink, the 64-ary orthogonal modulation is carried out to obtain good performance for non-coherent demodulation [48]. It should be noted that the Walsh codes are used for completely

channels. One of these channels is permanently and uniquely associated with each MS [48]. In contrast to the downlink channel, the IS-95 uplink traffic channel does not provide strict orthogonality to separate the logical channels. Rather, it uses a very long period spreading code with distinct time offsets to effectively reduce channel interference.

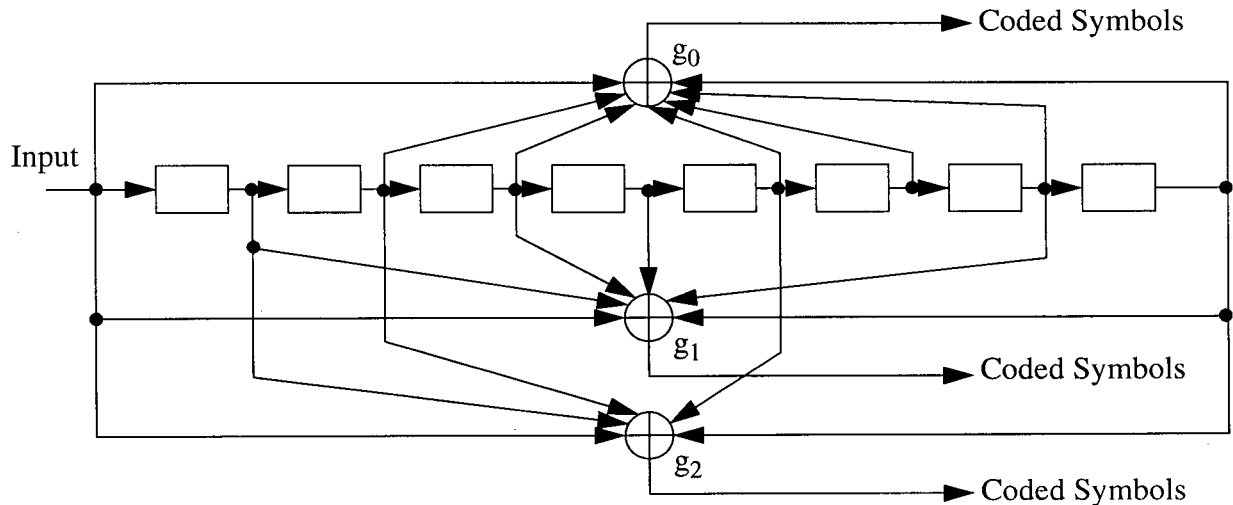


Fig. 4.7 IS-95 Uplink Convolutional Encoder

The uplink traffic channel is further spread in quadrature by a channel-unique short code with I and Q components, PN_I and PN_Q in Fig. 4.6, which is the same code used in the downlink traffic channel. The effect of combining long code and short code in signal spreading in the uplink is to provide a sequence that has an extraordinary long period, which is about 2^{57} (multiplication of the periods of the long code and short code sequences) [48]. The coded spread data stream is finally offset QPSK modulated on the RF carrier to produce a band limited analog signal, with the Q component delayed by half a chip period. The offset QPSK modulation is chosen to lower the performance requirements on the MS's power amplifier by reducing the envelope modulation of the RF analog signal [49].

In the IS-95 uplink direction, there is only one type of overhead channel: the access channel. In particular, no pilot signal is used for the sake of power efficiency, since unlike the downlink, an independent pilot signal would be required for each user in the system. The access channel is the vehicle for communication with the BS when the MS is not assigned to a traffic channel [48]. Its primary purpose is to send call originations and page responses to the BS.

4.4 IS-95 Multipath-Combining Receiver Structure

In order to improve the received signal strength and at the same time reduce the effects of multipath fading, RAKE receivers are employed at both the BS and MS to combine the multipath signals in the IS-95 systems [33]. In this section, we describe the IS-95 receiver architecture with RAKE combiners to take advantage of the radio channel multipath diversity. In Section 4.4.1, we define the RAKE receivers under consideration and the diversity combining techniques employed to combine the multipath signals. Section 4.4.2 describes the IS-95 downlink and uplink receiver structures.

4.4.1 RAKE Receiver Structure

Fig. 4.8 illustrates the structure of the considered RAKE receiver which consists of a total of 4 correlators called *fingers*. Each finger is dedicated to the reception of a multipath component except for the first correlator which continually searches for the next strongest multipath signal. Using the first correlator as the multipath searcher, the IS-95 RAKE receiver is able to capture the power of the three strongest multipath signals. In each finger, the received baseband signal is correlated by the spreading code, which is time-aligned with the delay of the multipath signal. After despreading, the signals in the fingers are weighted and combined using an appropriate diversity combining technique such as maximum ratio combining [37]. The signal is finally fed into the

symbol detector to decode the transmitted symbol.

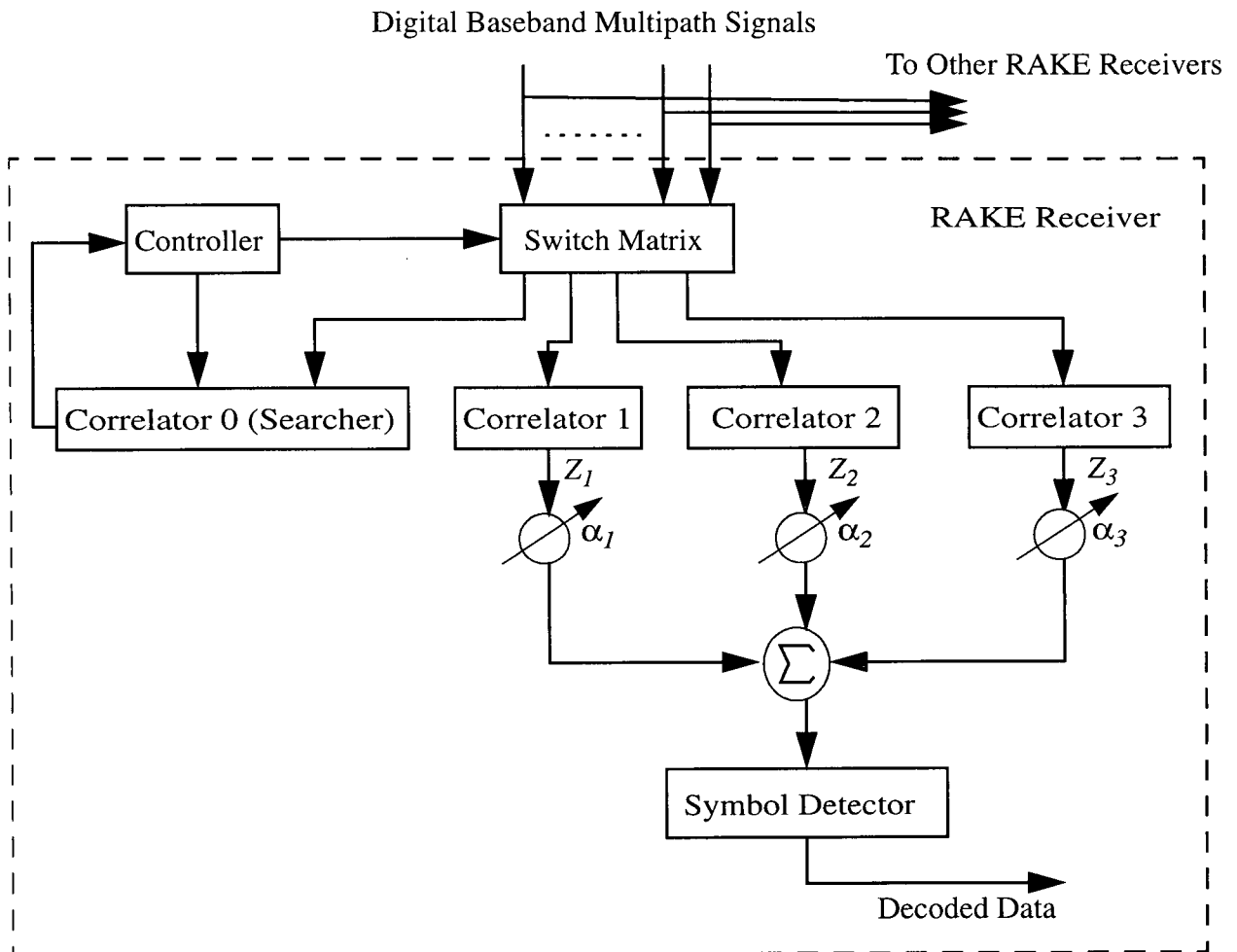


Fig. 4.8 Four-Finger RAKE Receiver Structure

In the IS-95 downlink channel structure, the pilot signal provides to the RAKE receiver an accurate estimate of the phase and amplitude of each multipath signal [1]. The information is used by the RAKE receiver to co-phase the multipath signals and coherently combine them using the optimum maximum ratio combining technique. The outputs of the RAKE receiver fingers, Z_k ($k = 1, 2$ and 3), can be mathematically expressed as

$$Z_k = r_k \sqrt{E_b} e^{j\theta_k} + n_k \quad (4.5)$$

where k is the index of the RAKE finger, r_k is the amplitude gain of the individual multipath channel, θ_k is the instantaneous phase of the signal, and n_k represents the interference treated as AWGN, with variance of $\frac{N_0}{2}$. The outputs are co-phased and weighted according to their instantaneous amplitude gains and then combined as follows [37]

$$Z_c = \sum_{k=1}^3 \left(\frac{r_k e^{-j\theta_k}}{\sqrt{r_1^2 + r_2^2 + r_3^2}} \left(r_k \sqrt{E_b} e^{j\theta_k} + n_k \right) \right) \quad (4.6)$$

The maximum ratio combining law is optimum since it maximizes the instantaneous SIR whose maximum value is given by [37]

$$SIR_{max} = \left(r_1^2 + r_2^2 + r_3^2 \right) \frac{E_b}{N_0} \quad (4.7)$$

Since in the uplink channel of the IS-95 systems no pilot signal is available, the multipath signals at the RAKE receiver are combined with no knowledge of the individual multipath signal phases. As a result, the non-coherent maximum ratio combining law is employed in which the multipath signals are weighted according to their instantaneous amplitudes and combined vector-wise. For the non-coherent maximum ratio combining law, Eq. (4.6) is modified as

$$Z_c = \sum_{k=1}^3 \left(\frac{r_k}{\sqrt{r_1^2 + r_2^2 + r_3^2}} \left(r_k \sqrt{E_b} e^{j\theta_k} + n_k \right) \right) \quad (4.8)$$

where the phase of the individual multipath signal θ_k can be assumed to be uniformly distributed over $[0, 2\pi)$. Compared with receivers that capture only the power of one multipath signal, the non-coherent IS-95 RAKE combiner results in improved SIR performance.

4.4.2 IS-95 Receiver Structure with RAKE Combiner

Fig. 4.9 illustrates the block diagram of the IS-95 downlink receiver considered in this thesis. The receiver contains a total of four RAKE fingers, where the first finger used as the multipath searcher is not shown in the figure. The received signal is downconverted and sampled to the digital baseband. In each RAKE finger, the signal is despread by multiplying with the short PN code which is time-shifted by an amount proportional to the multipath delay estimated from the pilot tone. In order to capture the power of a resolvable multipath signal, the short PN code in each finger is delayed for at least one chip period from the other fingers. The time-shifted Walsh code corresponding to the desired channel is then correlated with the despread signal. The correlated signal from each of the three combining fingers is combined with the other two signals according to the coherent maximum ratio combining law and passed to the decision device. Finally, the symbols are decoded with a hard-decision Viterbi decoder which uses maximum likelihood decoding algorithm.

Fig. 4.10 illustrates the receiver structure for the IS-95 uplink. Since the pilot signal is not available, non-coherent detection technique is employed in the receiver. The received signal is downconverted and sampled to the digital baseband. The baseband signal in each RAKE finger is despread by multiplying with the time-shifted user short and long PN codes which are delayed by more than a chip period from the other fingers. The despread signal is correlated with each of the 64 time-shifted Walsh functions, giving rise to 64 correlated Walsh values. Each of the correlated

Walsh values is combined with the estimated Walsh values in the other two combining fingers using non-coherent maximum ratio combining algorithm. The transmitted Walsh function is selected to be the one with the largest combined Walsh value. The estimated Walsh function sequence is then demodulated and the output is passed to a hard-decision Viterbi decoder to decode the transmitted data stream.

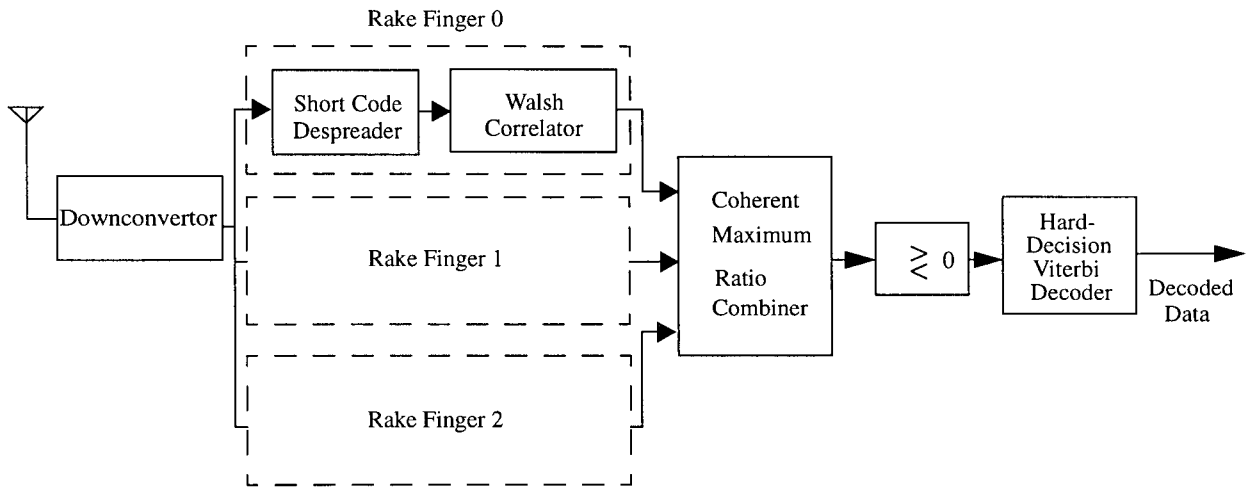


Fig. 4.9 IS-95 Downlink Receiver Structure

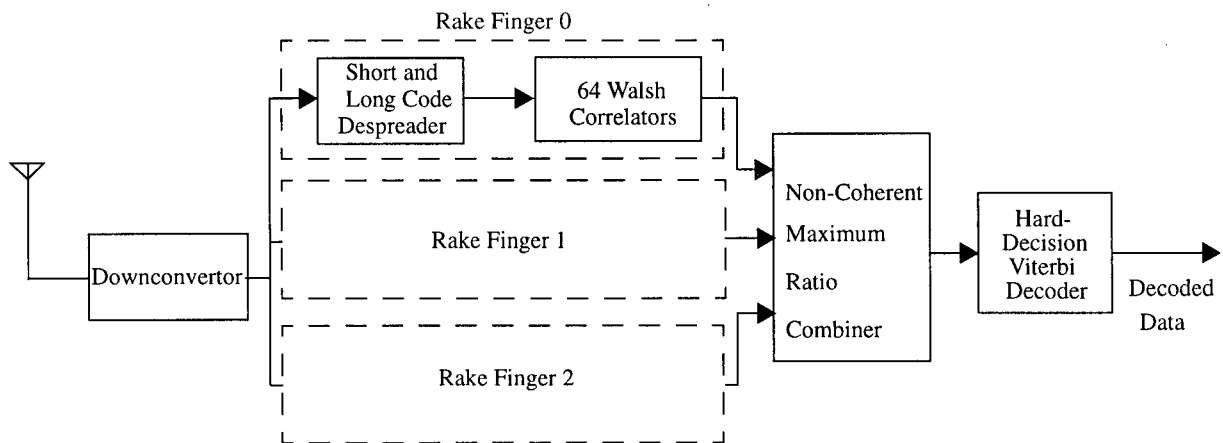


Fig. 4.10 IS-95 Uplink Receiver Structure

4.5 The IS-95 BER Performance Model

This section presents the IS-95 BER performance model for the multipath Rayleigh faded channel. The downlink and uplink receivers considered are those illustrated in Figs. 4.9 and 4.10. In order to improve the BER performance in the uplink that employs non-coherent detection, we have assumed dual antenna diversity in which two receivers at the BS are used to combine and decode the received signals [1]. The IS-95 BER performance model is used in our capacity simulations to estimate the downlink and uplink SIR thresholds at a BER of 10^{-3} for different multipath power profiles.

4.5.1 Viterbi Decoder Performance

Both the IS-95 downlink and uplink utilize convolutional encoders to provide FEC capability, and block interleavers to combat bursty bit errors in the mobile channel. In the receiver, each successive demodulated code symbol¹ is fed into the convolutional decoder to derive the original data bits transmitted. Assuming ideal interleaving, the random impact of the fading channel on the code symbols is independent from symbol to symbol, thus the channel is *memoryless*. The optimal convolutional decoder for the memoryless channel was analyzed by Viterbi [50] based upon the maximum likelihood decoding algorithm, which is also well known as the Viterbi algorithm.

In [50], the interference from other users on the demodulated code symbols was treated as AWGN and the channel was assumed to be unfaded. The BER value of the decoded data bits was derived as a function of the monotonic function $\ln(1/Z)/r$, where Z is the Symbol Error Rate (SER)

¹ In the IS-95 systems, each symbol contains 128 chips or $1/r$ bits, where r is the rate of the convolutional encoder in the transmitter.

of the evaluated code symbols before decoding through the Viterbi decoder. As it will be presented in Section 4.5.2, the monotonic function $\ln(1/Z)/r$ is also mathematically equal to the Chernoff bound on the corresponding SIR per bit (E_b/I_0) for the unfaded IS-95 downlink channel employing coherent QPSK modulation. For the average BER² of 10^{-3} considered in this thesis, the required $\ln(1/Z)/r$ value was evaluated to be 3.20 dB for the IS-95 downlink Viterbi decoder and 2.85 dB for the uplink decoder, respectively [50].

4.5.2 BER Performance for the One-Path Unfaded AWGN Channel

For the IS-95 downlink channels that utilize coherent QPSK modulation, the pilot-aided demodulator previously described in Section 4.4.2 provides optimal performance. Viterbi analyzed this demodulator structure and mathematically derived the Chernoff bound Z , on the SER³ for the one-path unfaded AWGN channel, which is given by [50]

$$P_e < Z = \exp\left[-\frac{E_s}{I_0}\right] \quad (4.9)$$

where E_s is the energy per symbol and E_s/I_0 denotes the SIR per symbol. Since $E_s = rE_b$, it follows from Eq. (4.9) that

$$P_e < Z = \exp\left[-\frac{rE_b}{I_0}\right] \quad (4.10)$$

$$\frac{\ln(1/Z)}{r} = \frac{E_b}{I_0} \quad (4.11)$$

² This is the BER of the data stream after the Viterbi decoding stage in Figs 4.9 and 4.10.

³ This is the SER of the evaluated code symbols before the Viterbi decoding stage in Figs 4.9 and 4.10.

Thus the monotonic function $\ln(1/Z)/r$ used to determine the BER performance function of the Viterbi decoder in Section 4.5.1 is equal to the required E_b/I_0 of the QPSK demodulated symbols for the one-path unfaded AWGN channel.

For the downlink receiver shown in Fig. 4.9 which employs coherent maximum ratio combining for the three combining RAKE fingers, the overall SIR that results is equal to the sum of the SIR of each multipath component. Thus for the 3-multipath Rayleigh faded channel, Eq. (4.9) is modified to

$$P_e < Z = \exp \left(\sum_{l=1}^3 \left[-\alpha_l^2 \frac{E_s}{I_0} \right] \right)$$

$$\text{with } \sum_{l=1}^3 E[\alpha_l^2] = 1 \quad (4.12)$$

where the PDF of the Rayleigh faded amplitude α_l was defined in Eq. (3.2), α_l^2 is its relative path gain and $E[\alpha_l^2]$ denotes its average power.

Viterbi also analyzed the non-coherent IS-95 uplink demodulator previously described in Section 4.4.2 and derived the Chernoff bound equation for the SER of the one-path unfaded AWGN channel [50]. The equation is mathematically expressed as the product of two complex integrals and numerical integration methods must be employed to obtain the corresponding SER value. By calculating a large set of SER results using numerical integration methods we found that the log-values of the SER and E_s/I_0 showed strong linearity. Therefore we derived the log-

linear equation by minimizing the MSE between the calculated results and the equation. The approximated log-linear equation for the Chernoff bound of the SER for the one-path unfaded AWGN channel is given by

$$P_e < Z \approx \exp \left[10 \left(1.975 \log \left(\frac{E_s}{I_0} \right) - 0.242 \right) \right]. \quad (4.13)$$

Assuming non-coherent combining of the RAKE finger outputs in Fig. 4.10 and dual antenna diversity in the IS-95 uplink channel, the receiver at the BS effectively combines a total of six multipath signals. The SER for the multipath Rayleigh faded uplink channel is thus modified to

$$P_e < Z \approx \exp \left[10 \left(1.975 \log \left(\left| \sum_{n=1}^2 \sum_{l=1}^5 -\frac{E_s}{I_0} \alpha_{n,l}^2 e^{j\theta_{n,l}} \right| \right) - 0.242 \right) \right]$$

$$\text{with } \sum_{l=1}^5 E[\alpha_{n,l}^2] = 1. \quad (4.14)$$

where n is the index of the two receiving antennas at the BS, $\alpha_{n,l}$ is the Rayleigh faded signal amplitude whose distribution is given in Eq. (3.2). $\theta_{n,l}$ denotes the phase of the individual multipath component and is uniformly distributed over $[0, 2\pi)$.

4.5.3 BER Performance for the Multipath Rayleigh Faded Channel

In order to estimate the average BER performance of the IS-95 receivers for the multipath Rayleigh faded channel, we have used computer simulation methods to generate the SIR thresholds for both the downlink and uplink channels. For the purpose of our simulation in which an average BER of 10^{-3} is considered, the target average SER value Z corresponding to the required value⁴ of the monotonic function $\ln(1/Z)/r$ is simulated. In our simulation model, the signal in each of the three combining RAKE fingers of the receiver is generated according to the Rayleigh distribution defined by Eq. (3.2). For the downlink simulation, the generated multipath signals are combined coherently as shown in Eq. (4.12). For the uplink, the phase of each multipath signal in Eq. (4.14) is generated according to uniform distribution over $[0, 2\pi)$ and the multipath signals are vectorially (non-coherently) combined.

In each simulation run, the downlink and uplink SER results are mathematically calculated using Eqs. (4.12) and (4.14), respectively. To ensure accuracy, the average SER results for each SIR value are calculated over a total of 90000 runs. All combinations of power levels being multiples of 0.02 are simulated, giving rise to a total of 234 profiles. For each of the 234 power profiles, the simulation program starts with a reasonable low E_b/I_0 value, i.e. 3.0 dB, and keeps simulating higher values in increments of 0.01 dB until the target average SER value Z is achieved. Fig. 4.11 illustrates the procedures to simulate the IS-95 BER performance for the multipath Rayleigh faded channel.

⁴ As previously mentioned in Section 4.5.1., these values are 3.20 dB for the downlink and 2.85 dB for the uplink, respectively.

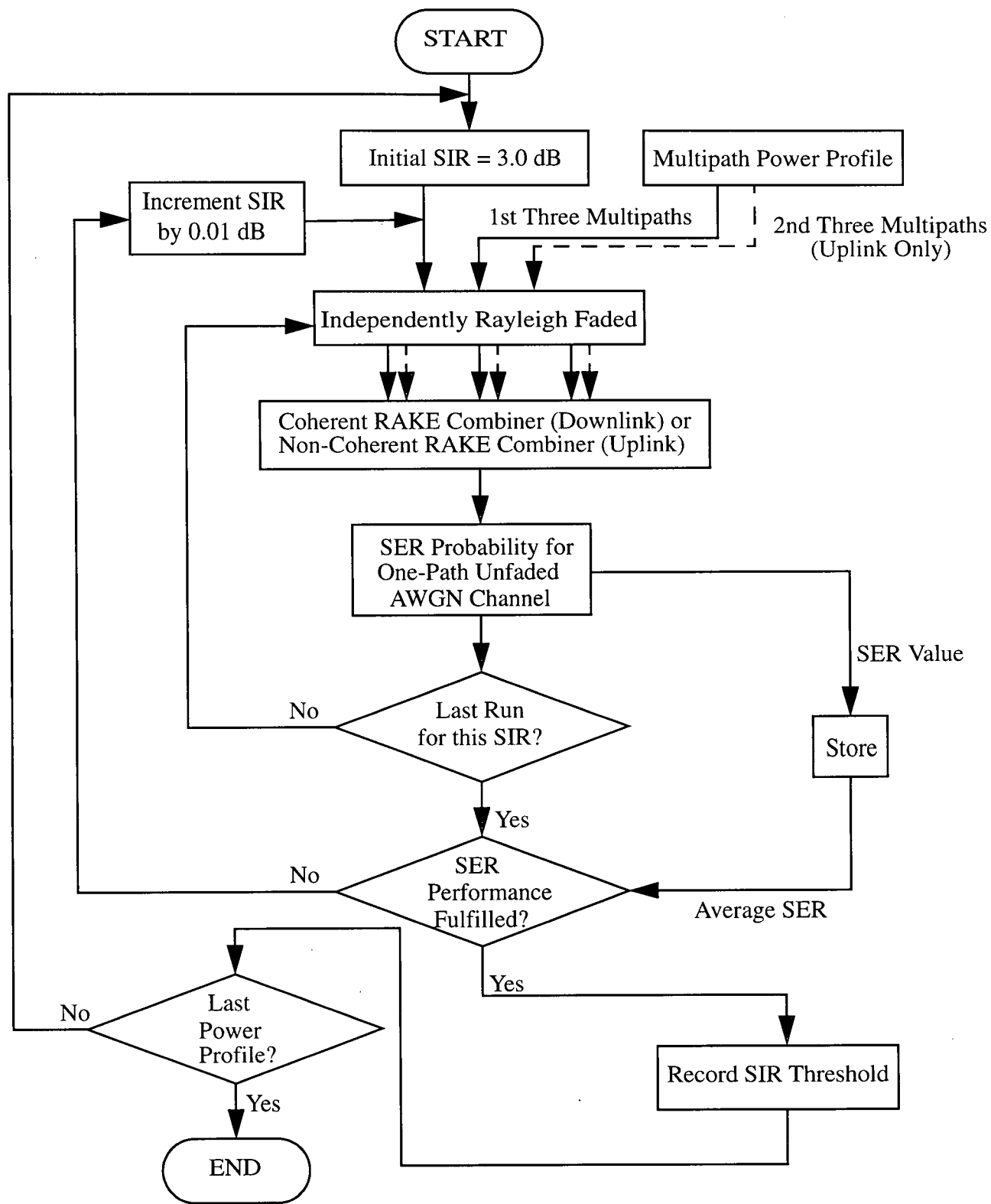


Fig. 4.11 IS-95 BER Performance Simulation Flow Diagram

Using the simulation program, the downlink and uplink E_b/I_0 values required to maintain the target average SER values Z are obtained for the 234 simulated power profiles. For each power profile, the corresponding excess energy is calculated by subtracting the E_b/I_0 value⁵ (in dB) required for the one-path unfaded QPSK channel from the E_b/I_0 value (in dB) obtained for the multipath Rayleigh faded channel through simulation. Thus the excess energy represents the additional energy required by the degraded multipath Rayleigh faded channel to achieve the same performance as the one-path unfaded QPSK channel. The overall downlink and uplink E_b/I_0 thresholds for an average BER of 10^{-3} are obtained by adding the excess energy to the required values of the monotonic function $\ln(1/Z)/r$. As a typical example, Table 4.5 lists the downlink and uplink values of the excess energy and the corresponding E_b/I_0 thresholds for six of the 234 simulated profiles. In Appendix B, the required E_b/I_0 thresholds for all the 234 simulated power profiles are listed.

P_0	P_1	P_2	Downlink Excess Energy (dB)	Overall Downlink E_b/I_0 Threshold (dB)	Uplink Excess Energy (dB)	Overall Uplink E_b/I_0 Threshold (dB)
1.00	0.00	0.00	2.48	5.68	1.05	3.90
0.84	0.08	0.08	1.60	4.80	1.79	4.64
0.64	0.26	0.10	1.08	4.28	2.60	5.45
0.50	0.50	0.00	1.19	4.39	2.36	5.21
0.44	0.36	0.20	0.84	4.04	3.15	6.00
0.34	0.34	0.32	0.77	3.97	3.32	6.17

Table 4.5 Sample IS-95 Downlink and Uplink SIR Thresholds

⁵ This value is calculated using Eq. (4.10).

From the downlink and uplink E_b/I_0 thresholds in Table 4.5, it is interesting to notice that for the one-path Rayleigh faded channel, which is the first profile, the IS-95 uplink performs better than the downlink. This is due to the use of orthogonal block coding scheme and dual antenna diversity in the uplink. The orthogonal block coding in the uplink provides better symbol separation as compared to the QPSK modulation in the downlink, while dual antenna diversity provides enhanced diversity gain. This suggests that in a remote area where there is a lack of scatterers so that there is always a strong LOS path, the IS-95 downlink may be the limiting direction of communication instead of the uplink. When the energy of the signal is carried by two or more multipaths, the uplink BER performance is degraded while the downlink performance is greatly improved. This is due to the non-coherent combining loss in the uplink RAKE combiner and the enhanced coherent combining gain in the downlink. The result confirms the well accepted observation made by many other researchers that the CDMA capacity is limited by the uplink [1][3][10][20].

With the simulated BER performance results, each channel can be assigned accurate downlink and uplink E_b/I_0 thresholds for an average BER of 10^{-3} based upon the multipath power distributions in our capacity simulation. This is done by matching the power profile of the channel to one of the 234 simulated profiles.

4.6 Conclusions

In this chapter, we briefly reviewed the DS-SS technology and described the downlink and uplink channel coding structures for the IS-95 systems. We presented Viterbi's analytical results on the optimal Viterbi decoder and the BER performance of the one-path unfaded AWGN channel for both the IS-95 downlink and uplink. Based upon these results, we studied the BER perfor-

mance for the multipath Rayleigh faded channels through computer simulation methods. The required E_b/I_0 thresholds to maintain an average BER of 10^{-3} were obtained for a large set of multipath power profiles. The simulated BER performance results enable us to accurately model the IS-95 receiver performance for the multipath Rayleigh faded channels in our capacity simulation. Lastly, the sample downlink and uplink E_b/I_0 thresholds were presented and compared. The different BER performance of the IS-95 downlink and uplink channels was explained based upon the modulation schemes, RAKE receiver structure and the antenna diversity employed.

Chapter 5 IS-95 CAPACITY SIMULATION: SYSTEM MODEL, PARAMETERS AND METHODOLOGY

5.1 Introduction

This chapter presents the system model for evaluating the capacity performance of IS-95 systems. The antenna models, IS-95 multipath channel model and the BER performance model previously presented in Chapters 2-4 are incorporated into the system simulation. The organization of the chapter is as follows. After this introductory section, in Section 5.2 we define the multiple-cell configuration under consideration and user distribution in each cell region. In Section 5.3, we introduce two important interference control schemes in cellular CDMA systems, namely power control and voice suppression. The modelling of these two features is incorporated into our simulation model. In Section 5.4, we discuss the Gaussian approximation for interference calculation and justify its validity in our multi-cell configuration. The single-path and multi-path capacity simulation approaches are presented in Section 5.5. In Section 5.6, we describe the overall simulation model for the IS-95 system capacity estimations. The system parameters and the simulation methodology employed are presented for both the downlink and uplink capacity estimations. Finally, the conclusions of this chapter are presented in Section 5.7.

5.2 Multi-Cell Configuration Model

In order to evaluate the capacity of a cellular system, the geometry of the cell region must first be defined. Fig. 5.1 illustrates the idealized 3-tier cell structure considered in our capacity simulation, which consists of a total of 19 hexagonal cells numbered from cell 0 to cell 18.

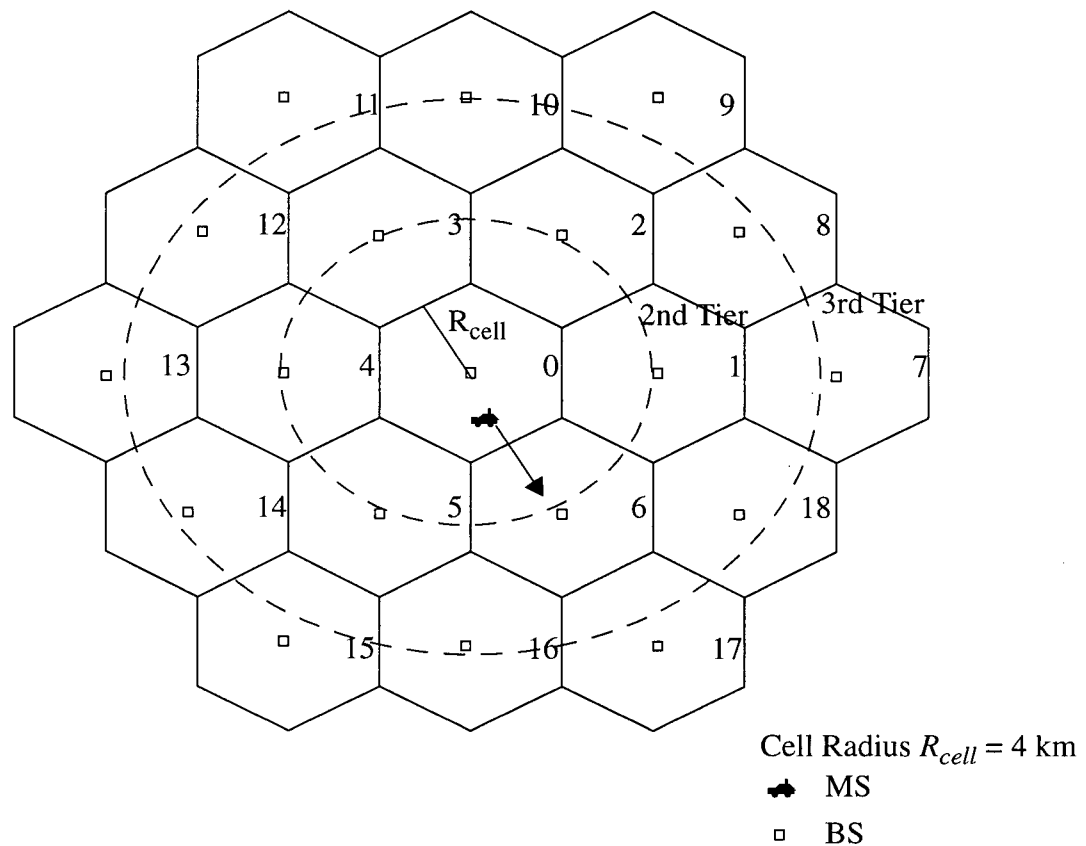


Fig. 5.1 3-Tier Cell Structure Consisting of 19 Hexagonal Cells

In this 3-tier cell model, each hexagonal cell has a radius of R_{cell} where $R_{cell} = 4$ km for simulating the macrocell environments. The BS is located at the centre of each cell. For these BSs, the cases of omnidirectional, 3-sectored and adaptive beamforming antennas are considered and simulated. For the MSs, only omnidirectional antennas are considered for practical reasons. The physical location of each MS in the system is independently generated according to uniform distribution across the whole 19-cell region. In our capacity simulation, the physical location of the MS just provides the information so that the channel path loss can be calculated, but it does not necessarily determine the BS to which the MS subscribes. In fact, each MS in the system

always subscribes to the BS from which the MS receives the strongest pilot signal [1][34], i.e. the propagation loss between the MS and its subscribed BS is the smallest compared with the other BSs. As an example shown in Fig. 5.1, a MS is physically located in cell 0, but it subscribes to the BS of cell 6 instead because the mobile channel between the MS and the BS of cell 0 suffers high signal power loss, possibly due to a large building located in the propagation path.

For each downlink and uplink channel, the receiver receives MAI from the other users in the same cell (intracell interference) as well as interference from the other 18 cells (intercell interference). The interfering signals from cells farther away are neglected in our capacity study. This is justified by the fact that they suffer significant signal attenuation due to the path loss so that the interference can be legitimately neglected. In our capacity simulation, the seven inner cells, i.e. cells 0-6 in Fig. 5.1, are the reference cells¹. The receiver BER performance of all users subscribing to the reference cells is monitored to determine the system capacity.

5.3 Power Control and Voice Suppression

In cellular CDMA systems, power control is essential because of the MAI. Since all users in the system share the same bandwidth, they interfere with each other when transmitting signals at the same time. Due to the propagation mechanism, the signal received by the BS from a MS close to the BS is much stronger than the signal received from another MS at the cell boundary, giving rise to the so called *near far* effect [1][34][36]. In order to achieve the desired system capacity levels, the transmit power of all signals must be controlled so that they arrive at the BS with the same mean power level [1][3], irrespective of the propagation distances.

¹ Due to the cell structure geometry, including the 3rd-tier cells as reference cells would result in an over-optimistic system capacity. This will happen because the users in these cells receive less interference compared with the users in the inner cells.

In contrast to the uplink, the signals and interference from the same BS propagate through the same channel and undergo the same attenuation when received at the MS. Thus the near far problem does not exist in the downlink. Instead, power control is required to minimize the interference to the users in the other cells and to compensate against the interference received from the BSs of the other cells. It takes the form of smart power allocation at the BS transmitter according to the needs of individual users in the given cell [1].

There exist two types of power control mechanisms: open loop and closed loop [4][34][36]. In the open loop power control, the interference conditions of the mobile channel are continuously measured and the transmit power is adjusted accordingly. In case of sudden signal degradation or improvement in the channel, the open loop power control mechanism provides a very rapid response over a period of a few microseconds by adjusting the transmit power [32]. However, the small-scale fading is not strongly correlated between the downlink and the uplink since the signals are transmitted in two distinct bands, which are separated by exactly 45 MHz in the IS-95 systems [4]. The open loop power control can only compensate for the large-scale fading effect, namely the path loss and shadowing loss. Thus the tighter closed loop power control is also required. In the closed loop power control, the SIR performance of the receiver is constantly measured and commands are sent to the transmitter at the other end to adjust the transmit power up or down by about one dB over a time interval of 1.25 ms [4][32]. The received power adjustment command is combined with the open loop estimate to determine the final value of the transmit power. While open loop power control only compensates for large-scale fading, closed loop power control may not be fast enough to match the fast fading environment. Power measurement error at the receiver and the finite step sizes in the control process also contribute to imperfect power control [36][51]. Measurements in large-scale tested systems showed that the

combination of open loop and closed loop power control results in power control errors which are approximately log-normal distributed, with a standard deviation of about 2 dB [51][52][53].

Another important interference control mechanism in cellular CDMA systems is the voice suppression. Extensive studies show that human voice is active only 35% to 40% of the time [54]. In digital vocoders, the voice activity is continuously monitored and transmission is suppressed for the channel when no voice is present. In the IS-95 systems, voice suppression is particularly advantageous in that the mobile user does not contribute interference to other users in this silent period, giving rise to enhanced system capacity.

In our capacity simulation, the above two interference control techniques, namely power control and voice suppression, are carefully considered and simulated. Unlike other research contributions (see for example [1][3][10]) which usually assume the same received power for all the mobile users, the received power is made proportional to the E_b/I_0 threshold assigned to the downlink or uplink channel. This gives a rather optimal system capacity since the transmit power is always kept minimum and also large enough to maintain the required BER performance, giving rise to minimized interference power in the system. For simulating imperfect power control, the received desired signal power of the k -th user, $(P_d)_k$, is further modified by a power control error random variable with a log-normal distribution, as given by

$$(P_d)_k \propto \left(\frac{E_b}{I_0} \right)_k 10^{\xi_k/10} \quad (5.1)$$

where ξ_k is a normal distributed variable with standard deviation of 2 dB. The voice suppression in the transmitter vocoders is included in our study so that the voice activity of user k , x_k , is an independent binomial random variable and is active with a probability of $\delta = 3/8$ [1], which is

mathematically expressed as

$$x_k = \begin{cases} 1 & \text{with probability } \delta \\ 0 & \text{with probability } 1-\delta. \end{cases} \quad (5.2)$$

5.4 Gaussian Approximation for Interference

In cellular CDMA systems, each user receives MAI from all the other users in the system. In the downlink channels, there exists an additional interfering signal, which is the pilot signal transmitted at relatively high power as compared to the user signals. Studies in many publications, e.g. [46][55][56][57], demonstrate that the interfering signals can be closely approximated as Gaussian noise in a system with a large number of mobile users. The approximation is quite accurate since powerful FEC convolutional codes are employed in the IS-95 systems, the symbol decisions are based upon PN long code sequences over which the interfering signal contributions are effectively the sums of a large number of binomial variables, which closely approximate the distribution of a Gaussian random variable [36]. This is particularly true in the IS-95 system under consideration, where a large number of users are generated in the 19-cell region.

Because of the large number of users in the multiple-cell system that give rise to an interference level much larger than the receiver noise, in this thesis we assume that the effects of the AWGN in the receiver are negligible [1][3]. Furthermore, for each BS, 20% of the total transmit power is assumed to be devoted to the pilot signal in order to provide a reliable reference for coherent demodulation in the downlink [1][58]. Since the Gaussian approximation holds for the interference in the considered IS-95 system, the overall interference received by the k -th mobile user, $(P_i)_k$, is calculated by adding the interference from all the other $n-1$ users in the system with a total of n users. If the channel is in the downlink direction, the power of the

received pilot signals is also added to the interference. Thus, the overall interference is mathematically calculated as

$$(P_i)_k = \begin{cases} \sum_{l=1}^n I_{k,l} x_l & (k \neq l) \quad \text{uplink} \\ \sum_{l=1}^n I_{k,l} x_l + \sum_{m=1}^{19} P_m & (k \neq l) \quad \text{downlink} \end{cases} \quad (5.3)$$

where $I_{k,l}$ denotes the interference received from the l -th user, x_l is the voice activity variable as defined in Eq. (5.2) and P_m denotes the power of the pilot signal received from the m -th BS.

Of great importance for maintaining reliable channel performance is the E_b/I_0 parameter. It is obtained by dividing the received desired signal power $(P_d)_k$ by the information bit rate R and dividing the interference $(P_i)_k$ by the total bandwidth W of the IS-95 CDMA channel and mathematically this can be expressed as

$$\left(\frac{E_b}{I_0}\right)_k = \frac{(P_d)_k/R}{(P_i)_k/W} = \frac{(P_d)_k W}{(P_i)_k R} \quad (5.4)$$

where $(P_d)_k/(P_i)_k$ denotes the SIR of the k -th user in which $(P_i)_k$ is calculated using Eq. (5.3)

and $W/R = 128$ is the processing gain of the IS-95 systems.

5.5 Single-Path and Multi-path Simulations

In order to reduce simulation time and also for comparison purposes, some of our simulations adopt the single-path approach. For such simulations, every user in the system is assigned a downlink E_b/I_0 threshold of 5 dB and uplink E_b/I_0 threshold of 7 dB in order to maintain an

average BER of 10^{-3} for adequate digital communication performance [1]. For the multi-path approach, 10^4 power profiles are pre-generated for each of the four simulated areas using the CMCM software program and stored in a database. Each profile contains the power distributions of 5 resolvable multipaths for simulating a delay spread of 4 μ s. Assuming 3-finger combining in the RAKE receiver previously described in Section 4.4, the downlink and uplink E_b/I_0 thresholds are determined based upon the simulation results of the IS-95 BER performance model, which are listed in Appendix B. This is done by matching the three strongest of the 5 multipaths in the profile to one of the simulated profile given in Appendix B.

The E_b/I_0 thresholds are the SIR requirements that must be maintained by each link in the system. System saturation occurs when a certain percentage (failure link percentage) of the users in the reference cells fail to fulfill their assigned SIR requirements. In the capacity simulations, we shall assume a failure link percentage of 1% [1]. When system saturation occurs, the number of mobile users in the system is recorded as the system capacity and another simulation run may start.

5.6 Simulation Methodology

In this section, we present our software simulation model used for the capacity evaluation of IS-95 systems. The basic idea behind the simulation model is to generate a large number of random deployments of mobile users in the 19-cell region under realistic system loading conditions and channel environments. The capacity performance of the system is obtained by analyzing a large set of capacity results obtained through simulations.

5.6.1 Pre-estimation Parameter Generation

For efficient capacity simulation, the individual parameters for each mobile user are generated at the beginning of each simulation run prior to capacity estimation. The physical location of each user is first generated assuming uniform distribution across the 19-cell region (see Fig. 5.1). Using the CMCM to model the multipath mobile radio channel, a power profile is generated for each MS-BS link by randomly selecting one of the pre-generated 10^4 profiles and the AOA is calculated for each of the 5 multipaths based upon the user's physical location. Since in the GBCM, the scatterers are confined to a small circular region as previously described in Section 3.4, the scattering objects that result in the shadowing effects for the multipath signals would be approximately the same. Thus, we assume the same shadowing loss for the multipaths of the same transmitted signal in our capacity simulation. The large-scale fading loss, namely the path loss plus the shadowing loss, for each MS-BS link is calculated using Eq. (3.1). The user is then subscribed to the BS to which the large-scale fading loss is the smallest as the user receives the strongest pilot signal from this BS.

With the knowledge of the BS subscription and the sector in which the user is physically located, the antenna models described in Chapter 2 are used to determine the antenna reception pattern based upon the system antenna design employed (omnidirectional, 3-sectored or beamforming array configuration). For the beamforming array configuration, the beam is assumed to be directed straight towards the strongest multipath of the desired signal. For each profile, which is generated for every MS-BS link, the antenna gain for each multipath of the desired signal is calculated according to its incoming AOA using the antenna models. The antenna gain is further combined with the large-scale fading loss to obtain the *desired multipath*

link loss, which essentially denotes the relative multipath power distributions of the desired signal. At the RAKE receiver with 3 combining fingers, the three strongest of the 5 multipath components are combined based upon their relative powers derived from their individual *desired multipath link loss* values. Using the IS-95 BER performance model, the user's E_b/I_0 threshold is then determined by matching the power distributions of the combined multipaths to one of the simulated profiles in Appendix B. For each user in the system, the overall *signal strength loss* is calculated by combining the *desired multipath link loss* of all the multipath signals.

In addition to the link loss for the desired signals, in our capacity simulations there also exists the link loss for the interfering signals. For each user, its antenna pattern is used to calculate the *interfering multipath link loss* by combining with the large-scale fading loss of the corresponding MS-BS link. This calculation is carried out for each of the 5 multipaths of the interfering signal, based upon the AOAs of the multipath signals. For each interfering signal, the 5 *interfering multipath link loss* values are further combined to obtain the overall *interference strength loss*. In the system with n mobile users, a total of $n-1$ *interference strength loss* values are thus calculated for each user. The calculated *signal strength loss* and *interference strength loss* values in the simulated system can be conveniently represented by a $n \times n$ *link loss* matrix M . An entry $m_{k,l}$ ($k \leq n, l \leq n$) in the matrix denotes the *interference strength loss* for the interference introduced to the k -th user by the l -th user when $k \neq l$, and denotes the *signal strength loss* when $k = l$.

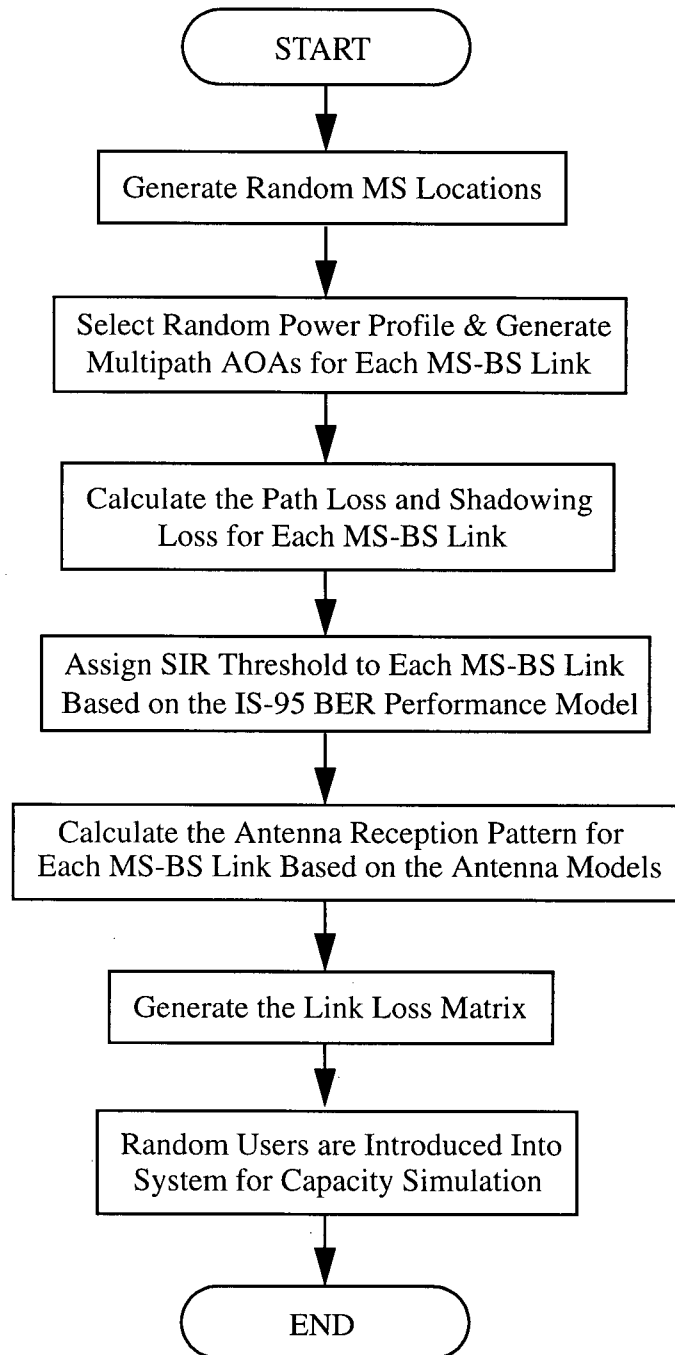


Fig. 5.2 Flow Diagram for Pre-estimation System Parameter Generation

In order to compare the capacity performance between the downlink and the uplink operations in the IS-95 systems, the same set of user locations are used for both the downlink and uplink capacity evaluations in each simulation run. However, all the other user parameters are generated independently for the downlink and uplink simulations since the mobile radio channels are virtually uncorrelated in the two directions of communications as they operate in separate frequency bands for the IS-95 systems [4]. Thus two separate *link loss* matrices exist in each simulation run, one for the downlink simulation and the other for the uplink simulation.

The pre-estimation parameter generation for the single-path simulations is much simpler as compared to the multi-path simulations described above. In the single-path simulations, the CMCM and IS-95 BER performance model are not invoked. The propagation path between the user and the BS is assumed to be LOS. The downlink and uplink E_b/I_0 thresholds are 5 dB and 7 dB respectively, as previously described in Section 5.5. The *signal strength loss* and *interference strength loss* parameters are calculated by combining the antenna gain and the large-scale fading loss of the one-path mobile channel.

Fig. 5.2 illustrates the overall simulation flow diagram for the initial system parameter generation prior to the capacity estimation. After all the system parameters are generated at the beginning of a simulation run, the mobile users are then introduced randomly into the schedule queue for later capacity simulations.

5.6.2 System Capacity Simulation

For the uplink simulations, the received power of the desired signal for the k -th user, $(P_d)_k$, is assumed to be proportional to its target E_b/I_0 requirements due to power control. Thus for the

single-path simulations, the received signal power is the same for each link, as assumed in [1]. The received power is modified by multiplying it with a log-normal distributed variable in order to simulate the errors due to imperfect power control. The transmission power, $(P_t)_k$, at the MS transmitter of the k -th user is then determined based upon the *signal strength loss* of the link, which is calculated as

$$(P_t)_k = \frac{(P_d)_k 10^{\xi_k/10}}{m_{k,k}} \quad (k \leq n) \quad (5.5)$$

where $m_{k,k}$ denotes the k -th diagonal entry in the *link loss matrix* M and $10^{\xi_k/10}$ represents the adjustments due to the imperfect power control as defined in Eq. (5.1).

For the downlink simulations, the modelling of the smart power allocation among the mobile users is much more involved as compared to the uplink simulations. The basic idea is to define an effective approach to accurately simulate the principle of equal BER performance for all the users in the IS-95 systems. First, an *interference parameter* needs to be calculated for each mobile user in the system by combining the interference from each of the 19 BSs, assuming that they transmit the same total power. Power control is simulated in the downlink communication so that the total transmit power of the BS is proportional to the number of mobile users that subscribe to it. The transmit power allocated to the individual mobile user by the BS is made proportional to the product of the E_b/I_0 threshold and the calculated *interference parameter* and inversely proportional to the *signal strength loss* of the link. As in the uplink simulations, the transmit power of the downlink channel is multiplied by a log-normal distributed variable in order to simulate the imperfect power control. With the transmit power of each link determined, the received signal

power, $(P_d)_k$, is calculated by multiplying the transmit power with the *signal strength loss*, which is mathematically expressed as

$$(P_d)_k = (P_t)_k 10^{\xi_k/10} m_{k,k} \quad (k \leq n) . \quad (5.6)$$

At the beginning of the each simulation run, the system is not loaded with any mobile users. The simulation proceeds by repeatedly introducing random users one-by-one from the schedule queue into the system, until the condition for system saturation occurs. After a new user is loaded into the system, the overall received interference of each mobile user in the system is calculated using Eq. (5.3), where the interference received from the l -th user, $I_{k,l}$, is calculated as

$$I_{k,l} = (P_t)_l m_{k,l} \quad (k \leq n, l \leq n, k \neq l) . \quad (5.7)$$

For the case of downlink capacity simulation, the transmit powers of all the users that subscribe to the same BS as the newly added user need to be re-adjusted since the total transmit power of this BS is increased after the addition of one new subscribing user.

The actual E_b/I_0 values of all the mobile users are calculated using Eq. (5.4) and then compared with their individual target E_b/I_0 thresholds. The number of users in the reference cells that fail to fulfill their individual target SIR performance is counted and the condition for system saturation is examined. If system saturation occurs, the current total number of users in the system is recorded as the system capacity and another simulation run may start, otherwise the simulation continues by introducing another user into the system from the schedule queue.

Figs. 5.3 and 5.4 depict the overall simulation flow diagrams for the uplink and downlink capacity simulations, respectively. In order to produce a large set of random system loading conditions, a total of 4000 simulation runs are performed for each system design. The obtained capacity results are stored in a database for later statistical analysis.

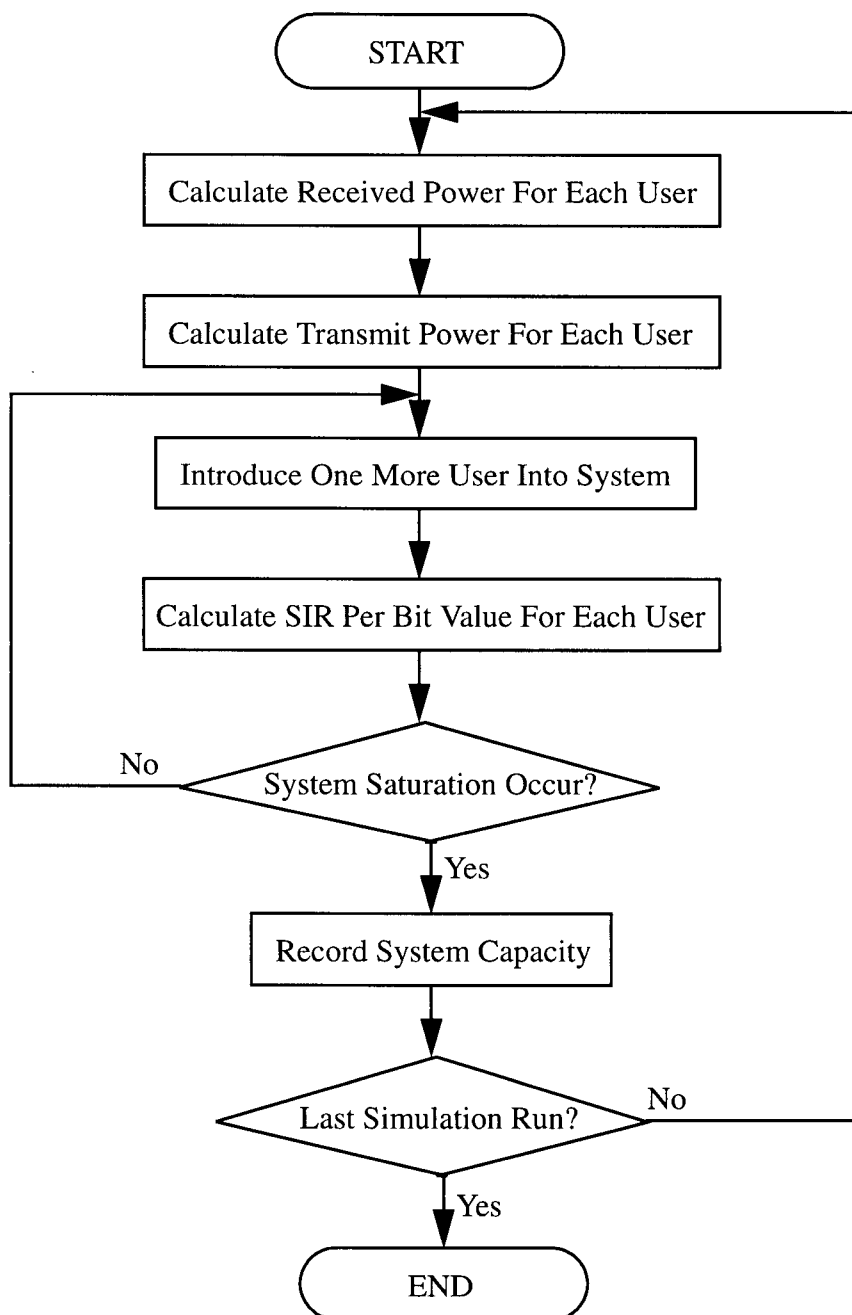


Fig. 5.3 Uplink Capacity Simulation Flow Diagram

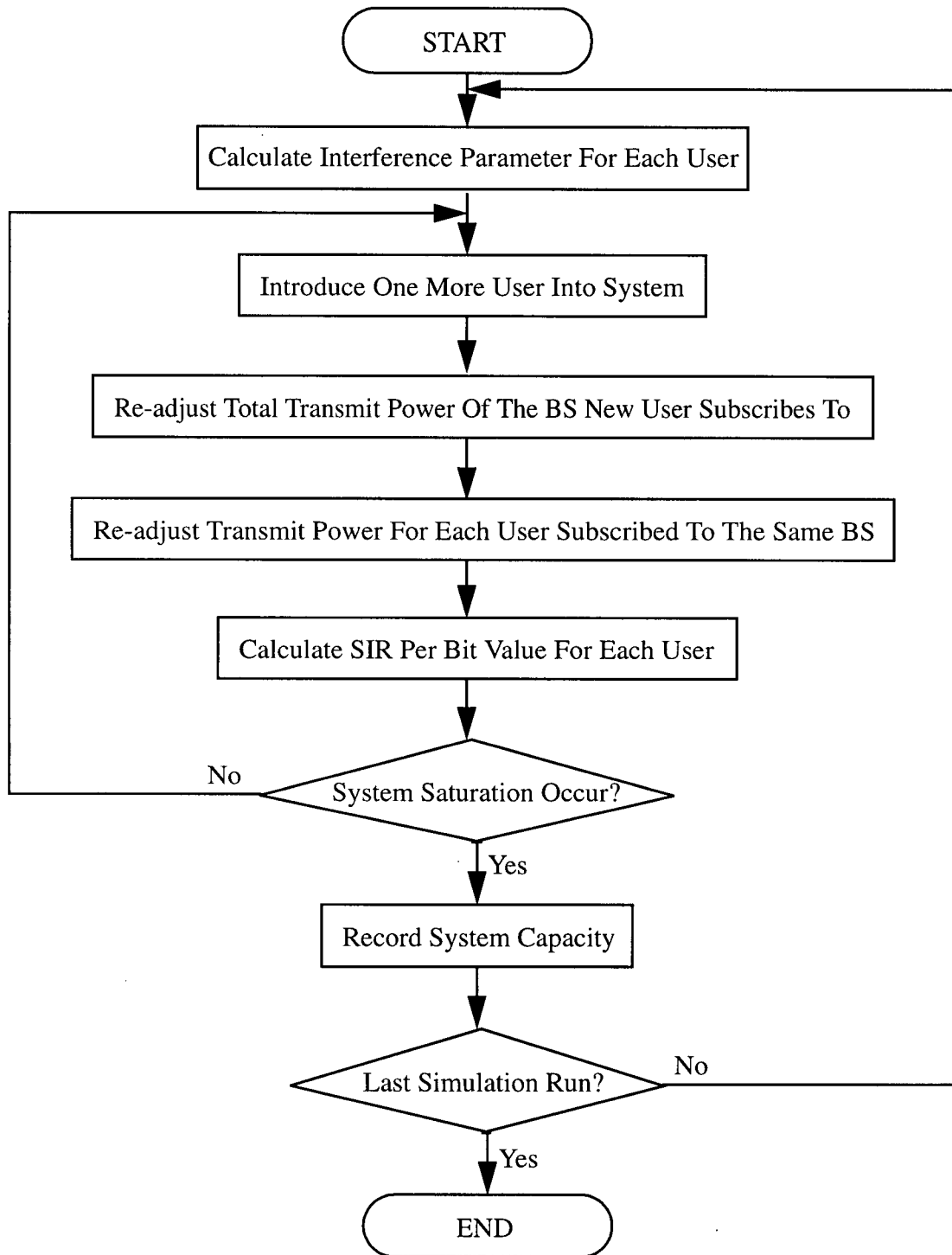


Fig. 5.4 Downlink Capacity Simulation Flow Diagram

5.7 Conclusions

In this chapter, we have described the overall simulation model for the IS-95 system capacity estimations. The multiple-cell configuration and user distribution of the communication system under consideration were defined. The power control and voice suppression features in cellular CDMA systems were modelled. For the simulated system in which a large number of mobile users were accommodated, the Gaussian approximation was employed to effectively calculate the interference level of the mobile users. For representation convenience, the *link loss* matrix was defined to represent the attenuations of the desired signals as well as the interfering signals. Using the *link loss* matrix, the powers of the received desired signals and the received interference were easily calculated and the E_b/I_0 value for the individual user was obtained. In order to accurately simulate the smart power allocation among the mobile users, an effective simulation approach with the principle of equal BER performance for all the users was employed. Finally, we illustrated the overall simulation flow diagrams for both the uplink and downlink capacity estimations.

Chapter 6 IS-95 CAPACITY SIMULATION RESULTS

6.1 Introduction

In this chapter, we will present the capacity performance results of the IS-95 systems obtained by using the simulation methodology previously described in Chapter 5. Both the uplink and downlink capacity results are simulated for system designs using omnidirectional, 3-sectored and adaptive beamforming antennas at the BS. Since the system capacity depends upon the number and the kind of sensors forming the beamforming system, we have also included the capacity results for using adaptive beamforming arrays consisting of 4, 6 and 8 omnidirectional as well as 4 cardioid sensors. For the multi-path simulations, the four different geographical areas considered in the HMCM, namely downtown San Francisco, downtown Oakland, downtown Berkeley and residential Berkeley are simulated. The capacity results obtained from both the single-path and multi-path simulations are presented in terms of the number of users in each cell. The associated mean, median and standard deviation of the capacity results are computed and given in the form of tables. For concise presentations, the Cumulative Density Function (CDF) of the capacity results, $C(x)$, is also plotted, where $C(x)$ is mathematically calculated as

$$C(x) = \frac{N_x}{N_T} \quad (6.1)$$

where N_x is the number of capacity results that are smaller than or equal to the capacity value x and N_T is the total number of simulation runs.

The organization of this chapter is as follows. After this introduction, Section 6.2 summarizes the values of the system parameters assumed in the simulations. In Sections 6.3 and 6.4, the

single-path and multi-path simulation results for various system antenna designs are presented and analyzed. The capacity results are further compared with those from other publications in Section 6.5. Wherever possible, qualitative explanations about these results are also included. Finally, the conclusions of this chapter are given in Section 6.6.

6.2 Simulation Parameters

Unless otherwise stated, the values for the various system parameters used in our capacity simulations are summarized in Table 6.1.

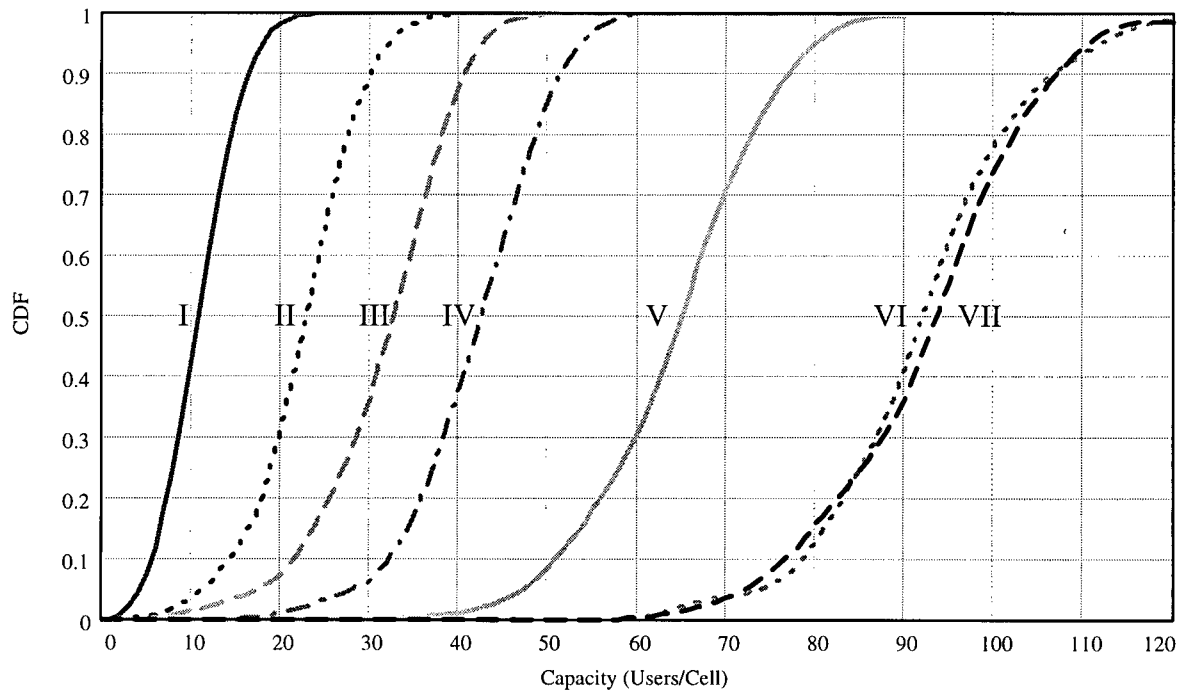
System Parameter	Parameter Value
Path Loss Index	Single-Path Simulation: 4 Multi-path Simulation: Given in Table. 3.1
Shadowing Standard Deviation	8 dB
Processing Gain	128
E_b/I_0 Thresholds For Mobile User	Single-Path Simulation: 5 dB for Downlink; 7 dB for Uplink Multi-path Simulations: Determined Based Upon Appendix. B
Power Control Error Standard Deviation	2 dB
Mobile User Voice Activity	3/8
Pilot Signal Power Proportion of Base Station	20%
Failure Link Percentage For System Saturation	1%
Hexagonal Cell Radius	4 km
Scattering Circle Radius	0.2 km

Table 6.1 System Parameter Values Assumed in Capacity Simulations

6.3 Single-Path Simulation Results

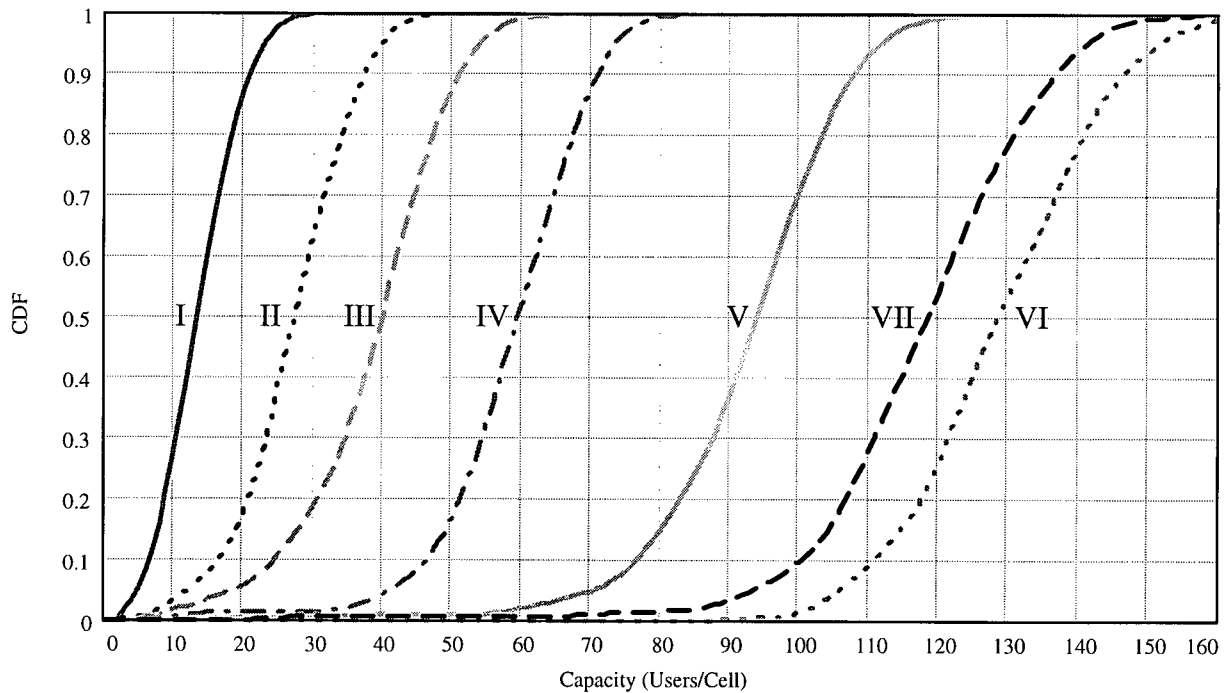
The CDF functions of the IS-95 uplink capacity for the simulated antenna designs obtained through single-path simulations are plotted in Fig. 6.1. As a comparison, the CDF func-

tions for the downlink results are plotted in Fig. 6.2. The statistics of the system capacity results are summarized in Table 6.2.



- I: Single Omnidirectional Sensor
- II: Single Cardioid Sensor, $FTBPR = 15$ dB, $HPB = 120^\circ$
- III: Single Ideal 3-Sectored Sensor
- IV: Beamforming Array, 4 Omnidirectional Elements
- V: Beamforming Array, 6 Omnidirectional Elements
- VI: Beamforming Array, 8 Omnidirectional Elements
- VII: Beamforming Array, 4 Cardioid Elements, $FTBPR = 15$ dB, $HPB = 120^\circ$

Figure 6.1 Single-Path Uplink Capacity as a Function of Antenna Design



- I: Single Omnidirectional Sensor
- II: Single Cardioid Sensor, $FTBPR = 15$ dB, $HPB = 120^\circ$
- III: Single Ideal 3-Sectored Sensor
- IV: Beamforming Array, 4 Omnidirectional Elements
- V: Beamforming Array, 6 Omnidirectional Elements
- VI: Beamforming Array, 8 Omnidirectional Elements
- VII: Beamforming Array, 4 Cardioid Elements, $FTBPR = 15$ dB, $HPB = 120^\circ$

Figure 6.2 Single-Path Downlink Capacity as a Function of Antenna Design

The results presented in Figs. 6.1 and 6.2 indicate that the capacity for the ideal 3-sectored antenna pattern is, as expected, approximately three times of that for the omnidirectional pattern. However, the net capacity improvement needs to be reduced to about two times when the more practical 3-sectored antennas of cardioid pattern are considered. For the case of adaptive beamforming arrays, the results for the antenna arrays consisting of 1, 4, 6 and 8 omnidirectional elements suggest that the capacity value can be closely approximated as a linear function of the

number of elements in the arrays. The results also show that the beamforming antennas with 8 omnidirectional elements and 4 cardioid elements result in comparable system capacity performance. This is consistent with the earlier observation that using the cardioid antenna can achieve double the capacity as compared to the omnidirectional antenna for the single sensor configuration. Clearly, the simulation results demonstrate that a many-fold increase in the overall system capacity can be achieved by using adaptive beamforming arrays in the IS-95 systems.

Antenna Type	Uplink Mean	Uplink Median	Uplink Standard Deviation	Downlink Mean	Downlink Median	Downlink Standard Deviation	Probability of Capacity Limited by Uplink
I	11.0	10.8	3.05	13.6	12.9	4.12	82.9%
II	22.6	23.1	5.42	27.1	27.1	7.26	84.4%
III	31.7	33.3	7.22	38.6	39.7	9.97	87.5%
IV	42.0	42.2	7.86	58.6	59.7	10.36	96.3%
V	64.4	64.9	9.57	92.5	93.9	13.33	97.4%
VI	92.0	91.9	11.04	128.9	128.2	13.37	99.3%
VII	92.7	94.3	11.42	117.8	118.7	16.01	97.8%

Table 6.2 Single-Path Simulation Result Statistics (Users/Cell)

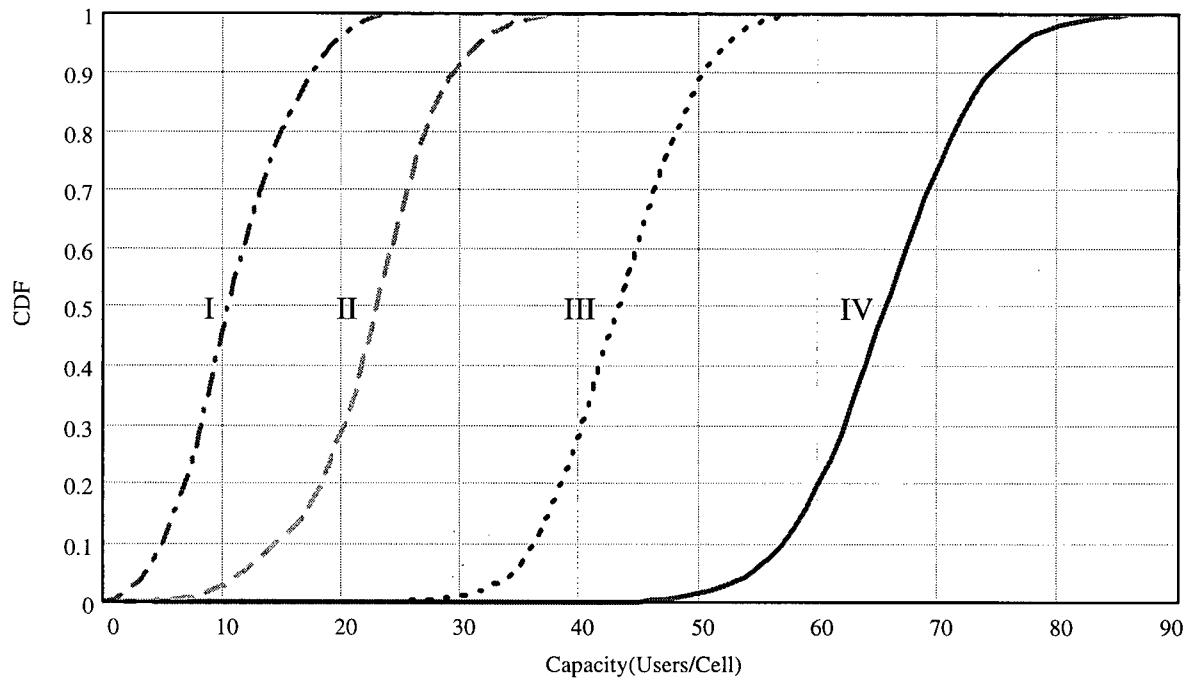
From Table 6.2, it is observed that the capacity of IS-95 systems is limited by the uplink with a probability of 82.9% for the single omnidirectional sensor and as high as 99.3% for the adaptive beamforming antennas. The lower probability for the single omnidirectional sensor configuration is due to its lower system capacity, thus it is more likely that some quasi-optimal uplink parameters can lead to a system capacity larger than that for the downlink. In general, the simulation results confirm that the capacity of cellular CDMA systems is limited by the uplink

communication [1][3][10].

Because of the importance of power control in cellular CDMA systems, we have also simulated the effects of power control performance on the system capacity. The considered system design uses the single 3-sectored antenna of cardioid pattern with $FTBPR = 15$ dB and $HPB = 120^\circ$ to model the common sectored antennas used in existing IS-95 CDMA networks. Since the uplink is the limiting direction, we have simulated only the uplink operation. The CDF functions are depicted in Fig. 6.3 for system operations with various standard deviations for power control errors. It is observed that the system capacity for power control error with standard deviation of 2 dB is approximately one third of that for perfect power control. The results clearly demonstrate that the capacity of cellular CDMA systems is highly sensitive to power control performance. This suggests that tighter power control mechanisms need to be carefully considered for future system design.

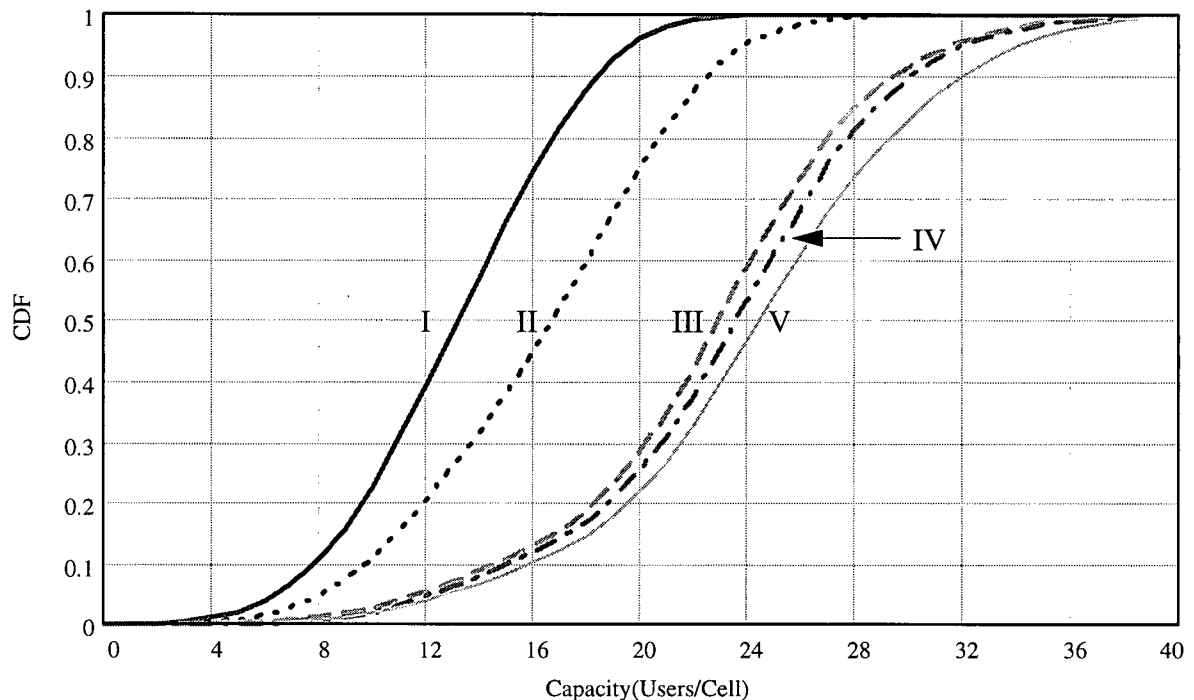
In addition to power control, the system capacity of cellular CDMA systems is also a function of the path loss index of the propagation channel. In Fig. 6.4, the uplink system capacity for the single cardioid antenna with $FTBPR = 15$ dB and $HPB = 120^\circ$ for the path loss index of 2.0, 3.0, 4.0, 5.0 and 6.0 is illustrated. The simulated path loss indices represent various signal propagation environments from the ideal free space where the path loss index is 2.0, to heavily urban city centres such as New York Manhattan where the path loss index can be as high as 6.0 [1]. The obtained capacity performance evaluation results indicate that the path loss indices of 2.0 and 3.0 yield the lowest capacity. This is due to the fact that the users in neighbouring cells contribute a significant level of interference relative to the user signal. For the path loss indices of 4.0, 5.0 and 6.0, the capacity results do not differ significantly among themselves, but are signifi-

cantly higher as compared to the case for the lower indices of 2.0 and 3.0. Because of the large path loss index, the interference from the users in neighbouring cells is heavily faded and thus is negligible as compared to the interference from the users within the same cell as well as the user signal, giving rise of higher system capacity. In addition, the desired user signal and the interference from the users within the same cell tend to fade together independently of the path loss index. This results in similar capacity results for the path loss indices of 4.0, 5.0 and 6.0 in our simulations.



- I: Power Control Error Standard Deviation = 3 dB
- II: Power Control Error Standard Deviation = 2 dB
- III: Power Control Error Standard Deviation = 1 dB
- IV: Power Control Error Standard Deviation = 0 dB (Perfect Power Control)

Figure 6.3 Single-Path Uplink Capacity as a Function of Power Control. The Considered Antenna Has Cardioid Pattern With $FTBPR = 15$ dB and $HPB = 120^\circ$



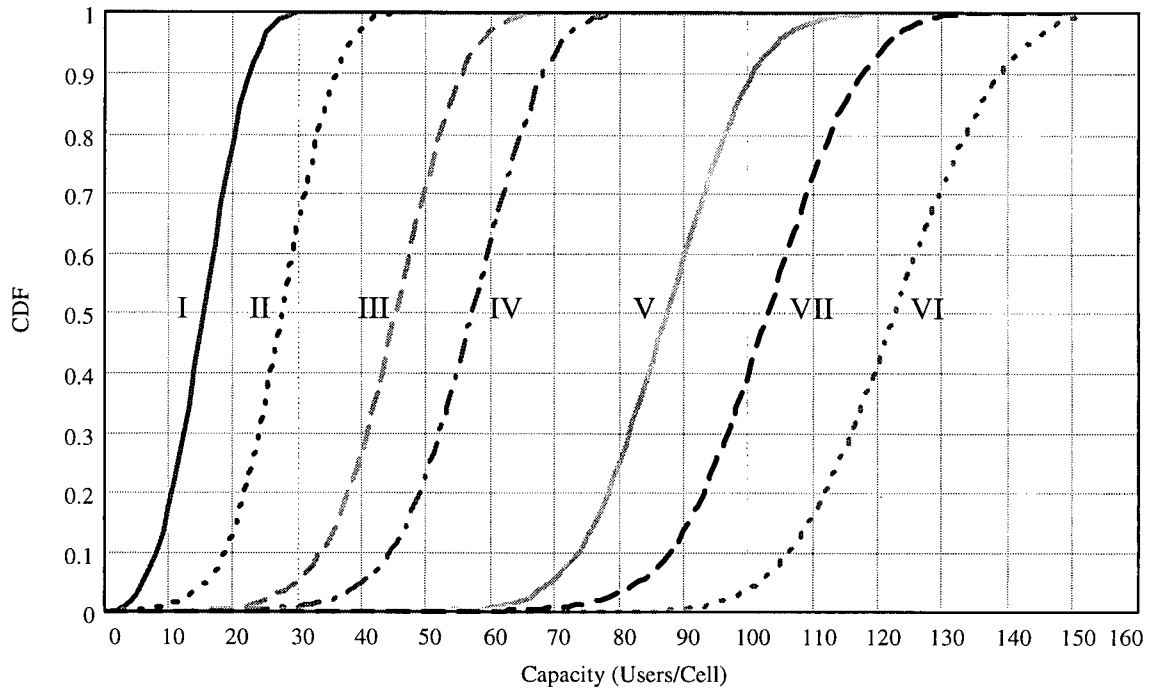
- I: Path Loss Index = 2.0
- II: Path Loss Index = 3.0
- III: Path Loss Index = 4.0
- IV: Path Loss Index = 5.0
- V: Path Loss Index = 6.0

Figure 6.4 Single-Path Uplink Capacity as a Function of Path Loss Index. The Considered Antenna Has Cardioid Pattern With $FTBPR = 15$ dB and $HPB = 120^\circ$

6.4 Multi-path Simulation Results

We have also performed multi-path simulations for the same system antenna designs whose capacity performance results were illustrated in Figs. 6.1 and 6.2 for the single-path simulations. The simulated area is downtown Oakland, which represents the downtown centre of a small to medium size city. The corresponding uplink and downlink capacity results are depicted in Figs. 6.5 and 6.6, respectively. The statistics of the system capacity results are further summa-

rized in Table 6.3.



- I: Single Omnidirectional Sensor
- II: Single Cardioid Sensor, $FTBPR = 15$ dB, $HPB = 120^\circ$
- III: Single Ideal 3-Sector Sensor
- IV: Beamforming Array, 4 Omnidirectional Elements
- V: Beamforming Array, 6 Omnidirectional Elements
- VI: Beamforming Array, 8 Omnidirectional Elements
- VII: Beamforming Array, 4 Cardioid Elements, $FTBPR = 15$ dB, $HPB = 120^\circ$

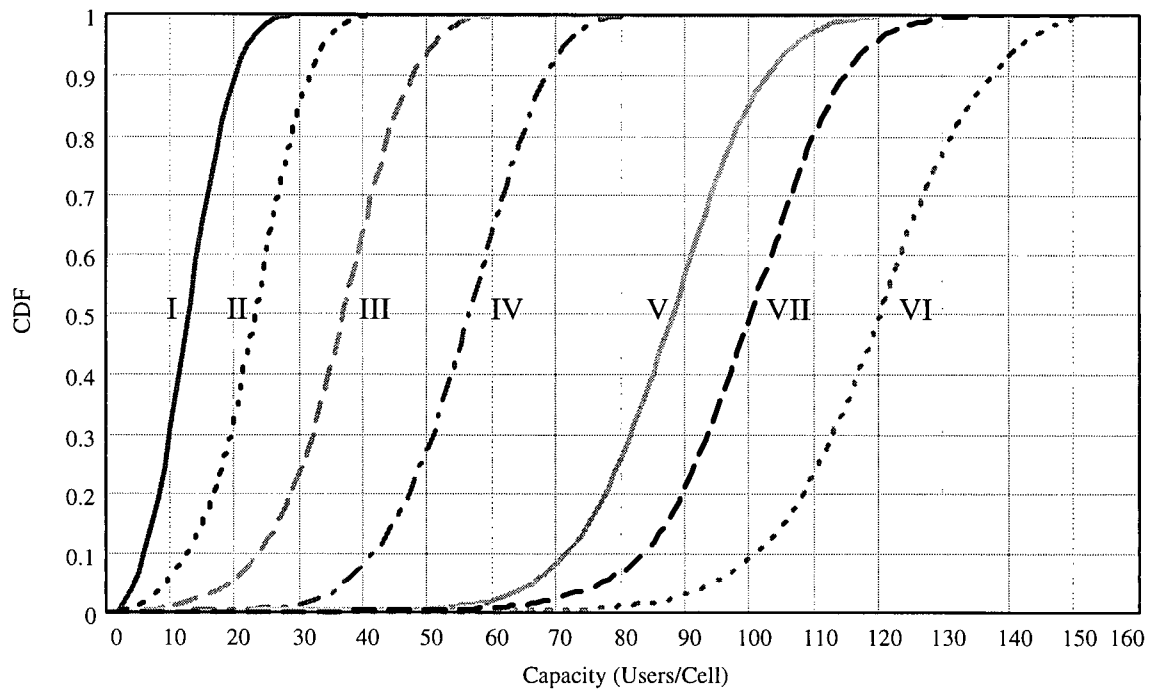
Figure 6.5 Multi-path Uplink Capacity as a Function of Antenna Design

From the capacity results obtained through the multi-path simulations for downtown Oakland, it is interesting to note that they do not differ significantly from equivalent results for the single-path simulations. The multi-path simulation results also confirm that using adaptive beamforming antennas can increase the system capacity by many folds. In Table 6.3, it is shown that for the single-sensor configurations, namely the omnidirectional, ideal 3-sector and cardioid

patterns, the system capacity is limited by the uplink with a probability of 24.7% or less. For the adaptive beamforming arrays, the system capacity is limited by the uplink with a probability ranging from 39.2% to 46.0%. This is quite different from the statistics of the single-path results in which the uplink is almost always the limiting link. In Appendix A, it can be seen that for downtown Oakland, the signals usually arrive at the receiver in two or three multipaths and one of the paths carries a large proportion of the signal power. In the IS-95 BER performance model previously described in Chapter 4, we have shown that the BER performance of the uplink is better than that of the downlink for the one-path Rayleigh fading channel, or a multipath Rayleigh fading channel where a path carries most of the signal power. This leads to our multi-path simulation results which suggest that the system capacity can be limited by the downlink in not severely urban areas.

Antenna Type	Uplink Mean	Uplink Median	Uplink Standard Deviation	Downlink Mean	Downlink Median	Downlink Standard Deviation	Probability of Capacity Limited by Uplink
I	15.3	15.6	4.13	12.9	12.3	3.99	24.7%
II	27.3	27.1	5.74	22.7	23.4	6.25	20.1%
III	44.8	45.3	7.84	36.1	37.1	8.66	11.8%
IV	56.5	57.1	8.78	55.6	56.6	9.92	46.0%
V	87.7	88.5	9.19	88.5	89.2	11.70	43.3%
VI	122.5	122.2	12.04	119.2	120.3	14.27	39.9%
VII	103.0	103.7	11.10	99.8	100.3	11.59	39.2%

Table 6.3 Multi-path Simulation Result Statistics for Downtown Oakland (Users/Cell)

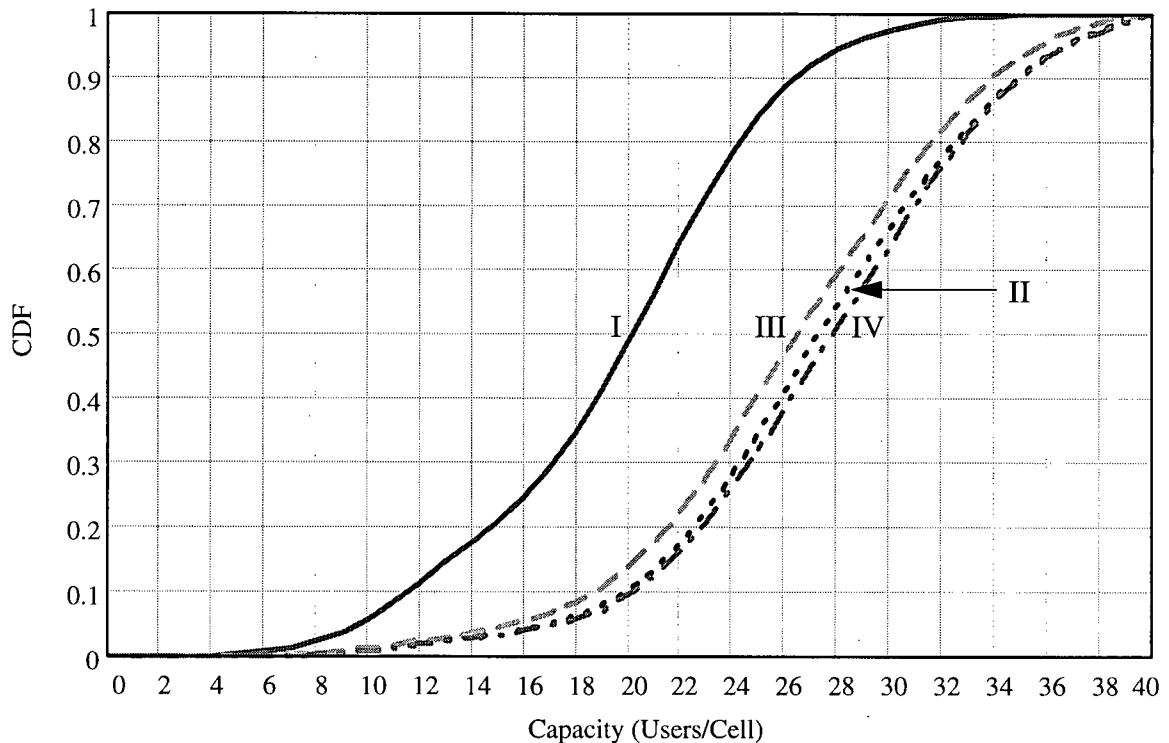


- I: Single Omnidirectional Sensor
- II: Single Cardioid Sensor, $FTBPR = 15$ dB, $HPB = 120^\circ$
- III: Single Ideal 3-Sectored Sensor
- IV: Beamforming Array, 4 Omnidirectional Elements
- V: Beamforming Array, 6 Omnidirectional Elements
- VI: Beamforming Array, 8 Omnidirectional Elements
- VII: Beamforming Array, 4 Cardioid Elements, $FTBPR = 15$ dB, $HPB = 120^\circ$

Figure 6.6 Multi-path Downlink Capacity as a Function of Antenna Design

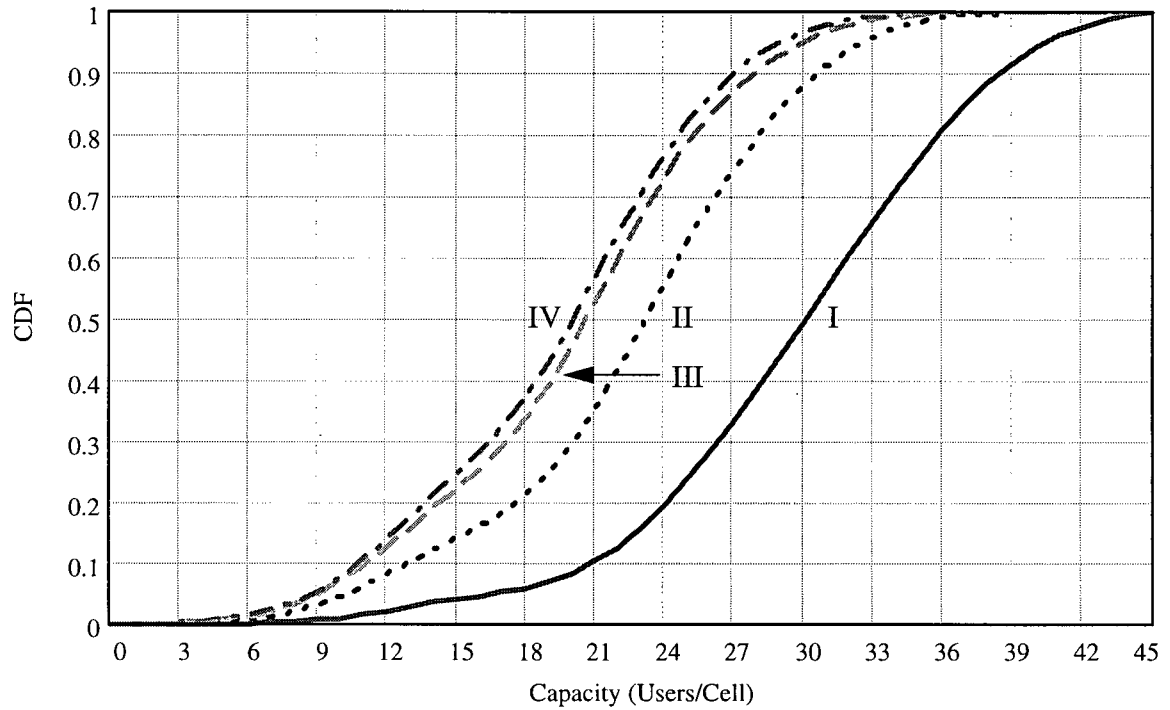
In order to investigate the effects of the multipath channel characteristics, which is a function of the geographical area urbanization, the system capacities for the four areas, namely downtown San Francisco, downtown Oakland, downtown Berkeley and residential Berkeley, are obtained through multi-path simulations. The system antenna design considered is the single cardioid sensor configuration with $FTBPR = 15$ dB and $HPB = 120^\circ$. For the simulation of each geo-

graphical area, the power profile of each link in the system is randomly selected from its individual pre-generated profile database containing a total of 40000 profiles, as previously described in Chapter 5. In addition, a different path loss index, as given in Table 3.1, is used for each area to account for the various degrees of urbanization in these four areas. The uplink and downlink capacity results are illustrated in Figs. 6.7 and 6.8, respectively. The statistics of the obtained capacity results have been calculated and are summarized in Table 6.4.



- I: Downtown San Francisco
- II: Downtown Oakland
- III: Downtown Berkeley
- IV: Residential Berkeley

Figure 6.7 Multi-path Uplink Capacity as a Function of Area Urbanization. The Considered Antenna Has Cardioid Pattern With $FTBPR = 15$ dB and $HPB = 120^\circ$



- I: Downtown San Francisco
- II: Downtown Oakland
- III: Downtown Berkeley
- IV: Residential Berkeley

Figure 6.8 Multi-path Downlink Capacity as a Function of Area Urbanization. The Considered Antenna Has Cardioid Pattern With $FTBPR = 15$ dB and $HPB = 120^\circ$

Area	Uplink Mean	Uplink Standard Deviation	Downlink Mean	Downlink Standard Deviation	Probability of Capacity Limited by Uplink
Downtown San Francisco	19.7	5.24	29.7	6.87	97.7%
Downtown Oakland	27.3	5.74	22.7	6.25	20.1%
Downtown Berkeley	26.3	5.79	20.1	5.98	9.9%
Residential Berkeley	27.6	5.89	19.5	5.85	4.8%

Table 6.4 Multi-path Simulation Result Statistics for the Four Areas (Users/Cell)

From Figs. 6.7 and 6.8, it can be seen that the capacity results for downtown Oakland, downtown Berkeley and residential Berkeley are largely similar. This can be explained by the similarity of their power profiles in which a strong multipath component carrying most of the signal power usually exists (see Appendix A). Furthermore, significant difference in the capacity results between these three areas and downtown San Francisco is also observed. Unlike the other three areas, the signal power for downtown San Francisco is usually evenly spread over two or three multipaths where a dominant multipath signal is usually absent (see Appendix A). For the uplink, downtown San Francisco has lower capacity since the BER performance is severely degraded in the multipath channel due to non-coherent combining in the RAKE receiver. For the downlink, on the contrary, downtown San Francisco has higher capacity since the multipath channel results in improved BER performance because of the significant diversity combining gain as a result of coherent combining. From Table 6.4, it can be seen that the system capacity for downtown San Francisco is limited by the uplink with a probability as high as 97.7%, while the probability is lower than 20.1% for the other three areas. These results further demonstrate that the capacity of IS-95 systems is limited by the uplink in urban areas and is limited by the downlink in suburban areas.

6.5 Comparisons With Other Publications

For the single-path simulations, our results indicate that the average uplink and downlink system capacity for the ideal 3-sectored pattern is 31.7 and 38.6 users/cell respectively, as given in Table 6.2. This is significantly lower than the analytical results of 108 users/cell for the uplink and 114 users/cell for the downlink derived by Gilhousen *et al.* [1]. The factors that result in this difference are two folds. Firstly in our simulations, realistic power control is considered in which a standard deviation of 2 dB is assumed for the error in the power control process, whereas ideal

power control is assumed in [1]. As shown in Fig. 6.3, the standard deviation of 2 dB for the power control error results in a system capacity which is approximately 1/3 of that for ideal power control. Secondly, in [1], the capacity is determined assuming that each user has a probability of 1% that its SIR drops below the target SIR threshold of 5 dB for the downlink and 7 dB for the uplink. However, the call admission criterion in the cellular networks is not dependent upon the individual user outage probability, but upon the ratio of the users meeting the outage conditions in the whole system. This call admission principle is appropriately modelled in our capacity estimation with the failure link percentage previously described in Chapter 5.

For the case of beamforming systems, our results indicate that an average uplink capacity of 42.0 users/cell can be achieved by using the 4 omnidirectional-element arrays. It is also shown that the system capacity can be further improved approximately linearly as a function of the number of antenna elements for the case of 6 and 8 elements. Liberti [10] has shown that by using beamforming antennas consisting of 2 and 4 omnidirectional elements, the system has an approximate capacity of 60 users/cell and 120 users/cell for the uplink. This is again significantly higher than our results because ideal power control is assumed in [10]. However, if we extrapolate our capacity results for ideal power control based upon the effects of power control performance on the system capacity depicted in Fig. 6.3, they seem to agree with Liberti's results. In addition, Liberti's results for the beamforming systems with 2 and 4 omnidirectional elements establish the same linear relationship between the system capacity and the number of antenna elements suggested by our capacity results.

6.6 Conclusions

In this chapter, we have presented the system capacity results of IS-95 systems obtained through both the single-path and multi-path simulations. As a conclusion, many folds of system capacity can be achieved by using adaptive beamforming arrays at the BS. The use of cardioid elements in beamforming systems results in further enhanced capacity which is approximately twice the capacity for using omnidirectional elements. Based upon the multi-path simulation results, it is shown that the system capacity of IS-95 systems is limited by the uplink in urban areas and limited by the downlink in rural areas.

Chapter 7 CONCLUSIONS AND FUTURE RESEARCH

7.1 Conclusions

In this thesis, we have investigated the beamforming antenna technique and evaluated its performance in terms of capacity improvements for IS-95 cellular CDMA systems under various channel conditions and employing different antenna patterns. The major contribution of the thesis is the development and software realization of a sophisticated and very generic simulation platform, which can be used to accurately estimate the capacity of such IS-95 systems employing adaptive antennas. The merits of the overall simulation platform, which includes various system models, can be summarized as follows.

7.1.1 IS-95 CDMA Multipath Model

We have implemented in software an extended multipath channel model for the IS-95 systems. This model is defined based upon two well established multipath channel models with their own accuracy and validity built upon extensive experimental data. Our multipath channel model is very useful because it can be used to generate random power profiles for four geographical areas of different urban characteristics, namely downtown San Francisco, downtown Oakland, downtown Berkeley and residential Berkeley. In addition, the model is tailored explicitly for the IS-95 systems by generating multipath signals readily resolvable by the RAKE combiner in the IS-95 receiver structure. The directions of arrival for the multipath signals are randomly generated with the assumption of a circular scattering region. Using the multipath model, realistic signal propagation conditions for both urban and rural areas can be accurately simulated for the IS-95 mobile radio channels.

7.1.2 IS-95 BER Performance Model

We have simulated the IS-95 receiver BER performance in multipath Rayleigh fading environments based upon Viterbi's analysis on the BER performance for the one-path unfaded Gaussian channel. Our simulation model considers a cellular CDMA system employing modulation and FEC schemes as defined in the IS-95 standard. The multipath signal combining performance of the IS-95 RAKE receiver is simulated for the coherent signal detection in the downlink, as well as the non-coherent detection in the uplink. The SIR per bit thresholds are obtained through computer simulations for a large set of power profiles in order to maintain an average BER of 10^{-3} in the IS-95 receivers. The BER performance model is very useful as it readily predicts the SIR requirements for a certain set of multipath signals arriving at the receiver.

7.1.3 Generic IS-95 Capacity Simulator

We have implemented in software a very generic capacity simulator in order to estimate the system capacity performance of IS-95 systems. Using the simulator, the performance of various system antenna designs at the BS can be simulated for both the uplink and downlink system capacities. In the simulation model, realistic channel models and various system imperfections are considered and simulated, such as the multipath conditions and imperfect power control. The 19-cell layout model is defined to include the effects of interference from neighbouring cells for generating accurate capacity results. Realistic call admission control principle and system loading conditions are employed to determine the system capacity. Based upon the simulation results, we have shown that using adaptive beamforming antennas in IS-95 systems can increase the system capacity many folds. In addition, an important observation has been made that the IS-95 system capacity is limited by the uplink in highly denser urban areas, and is limited by the downlink in

rural areas. Another merit of the IS-95 simulator is that it can be easily configured to evaluate the effects of different system parameters on the system capacity, e.g. power control performance and the path loss index.

7.2 Suggestions for Future Research

7.2.1 Beamforming Adaptivity in AWGN Environments

In the steering weight calculation, we have assumed that the estimation of the number of incoming signal waves and the corresponding AOAs are perfect. In reality, it is a highly computation intensive process [13][14][15], which may not be fast enough to match the rapidly changing signal propagation environments in the mobile radio channel. In addition, the estimation is performed based upon the received signals which are corrupted by the AWGN in the receivers in practical systems. These two factors negatively impact the adaptivity of the beamforming arrays and give rise to imperfect steering weight calculations. In CDMA systems, an inaccurate steering weight for the beamforming array results in degraded system capacity. In order to generate more accurate capacity results, it is worthwhile to extend the antenna model in our simulator for modelling the adaptive steering weight calculation process in practical systems. This, for example, could take the form of a statistical model characterizing the weight estimation errors by studying an extensive set of experimental results generated in a test beamforming system.

7.2.2 Adaptive Null-Steering Antennas

One of the interesting topics for future research would be the use of null-steering antenna arrays for enhancing the system capacity. Null-steering is a more advanced antenna technique compared with beamforming. Unlike adaptive beamforming arrays which maximize the gain of

the desired signals, null-steering arrays steer null patterns towards the interfering signals, virtually eliminating the interference. It would be an interesting project to compare the performance of adaptive beamforming and null-steering antennas in terms of the system capacity.

7.2.3 Improved IS-95 Capacity Simulator

Even though various system imperfections have been considered in our capacity simulator, it can be further enhanced if the necessary computer resources become available. In particular, finite power dynamic range is not considered in this thesis because it would require adjusting the power of each user in the system numerous times and the simulation would take an extremely long time. Instead, the n th power loss model is adopted, assuming that the transmit power of each user in the system is virtually unconstrained. However, this assumption is generally not true in practical systems. As a result, the evaluation of the effects of finite power dynamic range is a worthwhile task for future research. In addition, cell layout, user distribution and call traffic conditions are not uniform in practical cellular systems, it would be a promising project to incorporate a realistic geographical and traffic model in order to obtain even more accurate system capacity results.

7.2.4 CDMA2000 Capacity Simulator

Since CDMA2000, which is designed as an evolution of the IS-95 standard for the global 3G wireless services, has been standardized [7], it is valuable to extend our simulator for estimating the capacity of cellular CDMA2000 systems. In particular, the multipath channel model and BER performance model in our simulator need to be modified for the new designs of channel bandwidth, chip period, modulation techniques, the use of pilot signal for coherent detection in the uplink and the optional use of turbo codes for enhanced FEC performance [7].

Since it is expected that wireless data services will be popular in 3G cellular systems [6], the new capacity simulator needs to consider a CDMA2000 system where a large number of voice-service and data-service users co-exist, which may also have distinct BER performance requirements. The capacity results will be extremely useful to service providers in the system planning of the 3G cellular networks.

Bibliography

- [1] K. S. Gilhousen, I. M. Jacobs, R. Padovani, A. J. Viterbi, L. A. Weaver and C. E. Wheatley, "On the capacity of a cellular CDMA system," *IEEE Trans. Vehicular Tech*, vol. 40, no. 2, pp. 303-312, May 1991.
- [2] R. L. Peterson, R. E. Ziemer and D. E. Borth, *Introduction to Spread Spectrum Communications*. New Jersey: Prentice Hall, 1995.
- [3] P. Newson and M. R. Heath, "The capacity of a spread spectrum CDMA system for cellular mobile radio with consideration of system imperfections," *IEEE J. Select. Areas Commun.*, vol. 12, no. 4, pp. 673-684, May 1994.
- [4] EIA/IS-95, "Dual mode mobile station-base station wideband spread spectrum compatibility standard," PN-3119, Electronics Industries Association, Engineering Department, Dec. 1992.
- [5] A. Pursiainen and J. Viitanen, "The impact of U.S. cellular operators' CDMA decisions on the stock prices of cellular telephony producers," *Swedish School of Economics and Business Administration, Working Paper 315*, 1999.
- [6] D. N. Knisely, Q. Li and N. S. Ramesh, "Cdma2000: a third-generation radio transmission technology," *Bell Labs Tech. J.*, vol. 3, no. 3, pp. 63-78, July-Sept. 1998.
- [7] "Harmonized global 3G (G3G) technical framework for ITU IMT-2000 CDMA proposal (Rev. 21 June 1999)," International Telecommunication Union.
- [8] C. Webb, H. Huang, S. Brink, S. Nanda and R. Gitlin, "IS-95 enhancements for multimedia services," *Bell Labs Tech. J.*, vol. 1, no. 2, pp. 60-87, Oct-Dec. 1996.
- [9] N. Morinaga, M. Nakagawa and R. Kohno, "New concepts and technologies for achieving highly reliable and high-capacity multimedia wireless communications systems," *IEEE Communications Magazine*, vol. 35, no. 1, pp. 34-40, Jan. 1997.
- [10] J. C. Liberti and T. S. Rappaport, "Analytical results for capacity improvements in CDMA," *IEEE Trans. Vehicular Tech*, vol. 43, no. 3, pp. 680-690, Aug. 1994.
- [11] J. S. Thompson, P. M. Grant and B. Mulgrew, "Analysis of CDMA antenna array receivers with fading channels," *IEEE International Symposium on Spread Spectrum Techniques and Applications*, vol. 1, pp. 297-301, Feb. 1996.
- [12] J. C. Liberti and T. S. Rappaport, "A geometrically based model for line of sight multipath

- radio channels,” *Proc. Vehicular Tech. Conf.*, vol. 2, pp. 844-848, 1996.
- [13]R. O. Schmidt, “A signal subspace approach to multiple emitter location and spectral estimation,” PhD thesis, Stanford University, 1982.
- [14]R. Roy, “ESPRIT: Estimation of signal parameters via rotational invariance techniques,” PhD thesis, Stanford University, 1987.
- [15]R. B. Ertel and P. Cardieri, “Overview of spatial channel models for antenna array communication systems,” *IEEE Personal Communications*, vol. 5, no.1, pp. 10-22, Feb. 1998.
- [16]G. V. Tsoulos, M. A. Beach and S. C. Swales, “Adaptive antennas for third generations DS-CDMA cellular systems,” *Proc. 9th ICAP*, Apr. 1995, Eindhoven, the Netherlands.
- [17]Y. Wang and J. R. Cruz, “Adaptive antenna arrays for cellular CDMA communication systems,” *Proc. International Conference on Acoustics, Speech, and Signal Processing*, May 1995, Detroit, USA.
- [18]S. Anderson, M. Millnert, M. Viberg and B. Wahlberg, “An adaptive array for CDMA systems,” *IEEE Trans. Vehicular Tech.*, vol. 40, no. 1, pp. 230-236, Feb. 1991.
- [19]T. Ihara and R. Yamaguchi, “Effects of element pattern for adaptive array in CDMA mobile radio,” *IEEE-APS Conference on Antenna and Propagation for Wireless Communications*, vol. 30, 1998.
- [20]C. K. Kim and Y. S. Cho, “Capacity improvement of a MC-CDMA cellular system with antenna arrays in a fading channel,” *Proc. Vehicular Tech. Conf.*, vol. 3, pp. 2032-2036, May 1998.
- [21]L. K. H. Chan, A. S. Wright, P. T. Mathiopoulos, “Capacity improvements using beamforming antennas in IS-95 cellular CDMA systems,” *Proc. Vehicular Tech. Conf.*, vol. 2, pp. 1057-1061, May 1999.
- [22]H. Hashemi, “Simulation of the urban radio propagation channel,” *IEEE Trans. Vehicular Tech.*, vol. 28, no.3, Aug. 1979.
- [23]M. A. Jones and M. A. Wickert, “Direct-sequence spread spectrum using directionally constrained adaptive beamforming to null interference,” *IEEE J. Select. Areas Commun.*, vol. 13, no. 1, pp. 71-79, Jan. 1995.
- [24]A. K. Djedid and M. Fujita, “Adaptive array sensor processing applications for mobile telephone communications,” *IEEE Trans. Vehicular Tech.*, vol. 45, no. 3, pp. 405-416, Aug. 1996.

- [25]A. Hansson and T. M. Aulin, "On antenna array receiver principles for space-time-selective Rayleigh fading channels," *IEEE Transactions on Communications*, vol. 48, no. 4, pp. 648-656, Apr. 2000.
- [26]J. D. Kraus, *Antennas*. McGraw-Hill Book Company, 1988.
- [27]S. Haykin, *Array Signal Processing*. Prentice-Hall Book Company, 1985.
- [28]B. Widrow, K. M. Duvall, R. P. Gooch, and W. C. Newman, "Signal cancellation phenomena in adaptive antennas: causes and cures," *IEEE Trans. on Antenna and Propagation*, AP-30, 1982.
- [29]G. Tsoulos, M. Beach and J. McGeehan, "Wireless personal communications for the 21st century: European technological advances in adaptive antennas," *IEEE Communication Magazine*, vol. 35, no. 9, pp. 102-109, Sept. 1997.
- [30]R. T. Compton, *Adaptive Antennas*. New Jersey: Prentice Hall, 1988.
- [31]W. C. Y. Lee, *Mobile Cellular Telecommunications: Analog and Digital Systems*. McGraw Hill International Editions, 1995.
- [32]J. E. Padgett, C. G. Gunther and T. Hattori, "Overview of wireless personal communications," *IEEE Communications Magazine*, vol. 33, no. 1, pp. 28-41, Jan. 1995.
- [33]T. S. Rappaport, *Wireless Communications: Principles & Practice*. New Jersey: Prentice Hall, 1996.
- [34]W. C. Y. Lee, "Overview of cellular CDMA," *IEEE Trans. Vehicular Tech*, vol. 40, no. 2, pp. 291-302, May 1991.
- [35]G. L. Turin, "A statistical model of urban multipath propagation," *IEEE Transactions on Vehicular Technology*, vol. 21, no. 4, pp. 1-9, Feb. 1972.
- [36]R. Prasad, *CDMA for Wireless Personal Communications*. Artech House Book Company, 1996.
- [37]J. C. Jakes, *Microwave Mobile Communications*. New York: Wiley, 1974.
- [38]J. G. Proakis, *Digital Communications*. New York: McGraw Hill, 1989.
- [39]R. Steele, J Whitehead and W. C. Wong, "System aspects of cellular radio," *IEEE Communications Magazine*, vol. 33, no. 1, pp. 80-87, Jan. 1995.
- [40]A. F. Naguib and A. Paulraj, "Performance of wireless CDMA with M-ary orthogonal modulation and cell site antenna arrays," *IEEE J. Select. Areas Comm.*, vol. 14, no. 9, Dec. 1996.

- [41]H. Hashemi, "Simulation of the urban radio propagation channel," PhD thesis, University of California, Berkeley, 1977.
- [42]G. L. Turin, "Communication through noisy, random multipath channels," *IRE Convention Record*, part 4, 1956.
- [43]H. Suzuki, "A statistical model for urban radio propagation," *IEEE Trans. on Communication*, vol. 25, no. 1, pp. 673-680, July 1977.
- [44]D. Aszetyl, "On antenna arrays in mobile communication systems: fast fading and GSM base station receiver algorithms," PhD dissertation, Royal Inst. Technology, Mar. 1996.
- [45]C. Kchao and G. L. Stuber, "Analysis of a direct-sequence spread-spectrum cellular radio system," *IEEE Trans. on communications*, vol. 41, no. 10, pp. 1507-1517, Oct. 1993.
- [46]M. H. Fong, V. K. Bhargava, and Q. Wang, "Concatenated orthogonal/PN spreading sequences and their application to cellular DS-CDMA systems with integrated traffic," *IEEE J. Select. Areas Commun.*, vol. 14, no. 3, pp. 547-558, Apr. 1996.
- [47]A. J. Viterbi and R. Padovani, "Implications of mobile cellular CDMA," *IEEE Communications Magazine*, vol. 30, no. 12, pp. 38-41, Dec. 1992.
- [48]R. Padovani, "Reverse link performance of IS-95 based cellular systems," *IEEE Personal Commun.*, vol. 1, no. 3, pp. 28-34, July-Sept, 1994.
- [49]A. Baier, U. C. Fiebig, W. Granzow, W. Koch, P. Teder and J. Thielecke, "Design study for a CDMA-based third-generation mobile radio system," *IEEE J. Select. Areas Commun.*, vol. 12, no. 4, pp. 733-743, May 1994.
- [50]A. J. Viterbi, *CDMA-Principles of Spread Spectrum Communication*. Reading, MA: Addison-Wesley, 1995.
- [51]G. E. Corazza, G. D. Maio and F. Vatalaro, "CDMA cellular systems performance with fading, shadowing, and imperfect power control," *IEEE Trans. Vehicular Tech*, vol. 47, no. 2, pp. 450-459, May. 1998.
- [52]F. D. Priscoli and F. Sestini, "Effects of imperfect power control and user mobility on a CDMA cellular network," *IEEE J. Select. Areas Commun.*, vol. 14, no. 9, pp. 1809-1817, Dec. 1996.
- [53]M. A. Mokhtar and S. C. Gupta, "Power control considerations for DS/CDMA personal communication systems," *IEEE Trans. Vehicular Tech*, vol. 41, no. 4, pp. 479-487, Nov. 1992.

- [54]P. T. Brady, "A statistical analysis of on-off patterns in 16 conversations," *Bell Syst. Tech. J.*, vol 47, no. 1, pp. 73-91, Jan. 1968.
- [55]M. B. Pursley and D. V. Sarwate, "Performance evaluation for phase-coded spread-spectrum multiple-access communication - part II: code sequence analysis," *IEEE Trans. Comm.*, vol. 25, no. 8, Aug. 1977.
- [56]J. S. Lehnert and M. B. Pursley, "Error probabilities for binary direct-sequence spread-spectrum communications with random signature sequences," *IEEE Trans. Comm.*, vol. 35, no. 1, Jan. 1987.
- [57]J. M. Holtzman, "A simple, accurate method to calculate spread-spectrum multiple access error probabilities," *IEEE Trans. Comm.*, vol. 40, no. 3, pp. 461-464, Mar. 1992.
- [58]A. J. Viterbi, A. M. Viterbi and E. Zehavi, "Performance of power-controlled wideband terrestrial digital communication," *IEEE Trans. on Communications*, vol. 41, no. 4, pp. 559-569, Apr. 1993.

Appendix A. Sample Power Profiles for the Four Simulated Areas

This appendix lists 30 sample power profiles generated using the CMCM software program for the four simulated geographical areas, including downtown San Francisco, downtown Oakland, downtown Berkeley and residential Berkeley. By comparing the listed profiles, it is obvious that downtown San Francisco exhibits the strongest multipath phenomenon. In residential Berkeley, there is usually a strong LOS path and its multipath phenomenon is the lightest as compared to the other three areas.

Profile Index	P_0	P_1	P_2	P_3	P_4
1	0.387700	0.411980	0.033376	0.154205	0.012740
2	0.012158	0.550599	0.428711	0.000538	0.007993
3	0.445239	0.553779	0.000023	0.000569	0.000390
4	0.794709	0.202732	0.002232	0.000275	0.000052
5	0.005825	0.000013	0.989615	0.003901	0.000645
6	0.184931	0.785534	0.011032	0.013554	0.004949
7	0.019693	0.245931	0.428533	0.301920	0.003924
8	0.000000	0.491405	0.429800	0.063614	0.015181
9	0.453722	0.250043	0.099600	0.181161	0.015473
10	0.292867	0.320293	0.003560	0.018367	0.364913
11	0.000000	0.757083	0.124464	0.093504	0.024949
12	0.167354	0.828988	0.002539	0.000433	0.000687
13	0.025033	0.869325	0.099302	0.005868	0.000472
14	0.039429	0.387406	0.538707	0.014654	0.019804
15	0.001096	0.050976	0.807589	0.139336	0.001004
16	0.363109	0.611370	0.003274	0.015520	0.006728
17	0.025773	0.506068	0.403201	0.039701	0.025257
18	0.512593	0.000806	0.167584	0.186718	0.132299
19	0.000000	0.738179	0.118537	0.137337	0.005946
20	0.954254	0.045002	0.000339	0.000178	0.000226
21	0.267411	0.551135	0.065313	0.072396	0.043745
22	0.073742	0.260598	0.343999	0.288743	0.032917
23	0.000000	0.404730	0.378511	0.145621	0.071138
24	0.330312	0.245210	0.154760	0.208719	0.060999
25	0.283873	0.296868	0.031297	0.071090	0.316872
26	0.000000	0.515881	0.209171	0.181298	0.093650
27	0.288704	0.642554	0.035560	0.014683	0.018500
28	0.105194	0.619911	0.209516	0.050930	0.014449
29	0.109300	0.342603	0.404003	0.066633	0.077461
30	0.021185	0.144497	0.575139	0.238896	0.020282

Table A.1 Random Power Profiles For Downtown San Francisco

Profile Index	P_0	P_1	P_2	P_3	P_4
1	0.999278	0.000722	0.000000	0.000000	0.000000
2	0.036354	0.728033	0.000000	0.037319	0.198295
3	0.988448	0.007361	0.004191	0.000000	0.000000
4	0.995510	0.004050	0.000000	0.000440	0.000000
5	0.447209	0.367056	0.185735	0.000000	0.000000
6	0.999932	0.000022	0.000000	0.000046	0.000000
7	0.934035	0.058425	0.002662	0.000965	0.003914
8	0.997072	0.002576	0.000317	0.000000	0.000036
9	0.552111	0.447889	0.000000	0.000000	0.000000
10	0.866455	0.133545	0.000000	0.000000	0.000000
11	0.968046	0.031954	0.000000	0.000000	0.000000
12	0.998573	0.000142	0.001169	0.000116	0.000000
13	0.968498	0.031502	0.000000	0.000000	0.000000
14	0.999180	0.000394	0.000426	0.000000	0.000000
15	0.730959	0.264512	0.004530	0.000000	0.000000
16	0.795965	0.200980	0.003055	0.000000	0.000000
17	0.643736	0.310501	0.031010	0.000000	0.014753
18	0.474367	0.013694	0.170887	0.341052	0.000000
19	0.986637	0.013347	0.000016	0.000000	0.000000
20	0.998958	0.000442	0.000600	0.000000	0.000000
21	0.143857	0.708566	0.147577	0.000000	0.000000
22	0.892614	0.071881	0.001513	0.033555	0.000437
23	0.999911	0.000052	0.000037	0.000000	0.000000
24	0.937213	0.018942	0.000905	0.000130	0.042810
25	0.623496	0.376060	0.000136	0.000308	0.000000
26	0.996984	0.000189	0.002268	0.000558	0.000000
27	0.996996	0.000000	0.002879	0.000126	0.000000
28	0.906916	0.093084	0.000000	0.000000	0.000000
29	0.998392	0.001378	0.000230	0.000000	0.000000
30	0.672476	0.327477	0.000000	0.000000	0.000047

Table A.2 Random Power Profiles For Downtown Oakland

Profile Index	P_0	P_1	P_2	P_3	P_4
1	0.998315	0.001685	0.000000	0.000000	0.000000
2	0.947526	0.052391	0.000000	0.000083	0.000000
3	0.999691	0.000291	0.000018	0.000000	0.000000
4	0.803435	0.191866	0.004299	0.000000	0.000400
5	0.008633	0.991367	0.000000	0.000000	0.000000
6	0.999798	0.000051	0.000151	0.000000	0.000000
7	0.999902	0.000029	0.000023	0.000045	0.000000
8	0.999365	0.000628	0.000007	0.000000	0.000000
9	0.003268	0.995917	0.000816	0.000000	0.000000
10	0.999345	0.000655	0.000000	0.000000	0.000000
11	0.987766	0.012049	0.000184	0.000000	0.000000
12	0.000000	0.998490	0.001510	0.000000	0.000000
13	0.997133	0.002867	0.000000	0.000000	0.000000
14	0.999031	0.000915	0.000055	0.000000	0.000000
15	0.772079	0.206470	0.021451	0.000000	0.000000
16	0.995994	0.003895	0.000111	0.000000	0.000000
17	0.103960	0.790611	0.000000	0.105429	0.000000
18	0.995461	0.004539	0.000000	0.000000	0.000000
19	0.999408	0.000592	0.000000	0.000000	0.000000
20	0.998829	0.001171	0.000000	0.000000	0.000000
21	0.999665	0.000308	0.000027	0.000000	0.000000
22	0.987470	0.004929	0.007587	0.000014	0.000000
23	0.072576	0.927412	0.000012	0.000000	0.000000
24	0.980707	0.019283	0.000010	0.000000	0.000000
25	0.967901	0.032099	0.000000	0.000000	0.000000
26	0.991188	0.008808	0.000003	0.000000	0.000000
27	0.999807	0.000189	0.000003	0.000000	0.000000
28	0.183768	0.697157	0.119075	0.000000	0.000000
29	0.999981	0.000000	0.000005	0.000013	0.000000
30	0.999998	0.000002	0.000000	0.000000	0.000000

Table A.3 Random Power Profiles For Downtown Berkeley

Profile Index	P ₀	P ₁	P ₂	P ₃	P ₄
1	0.999985	0.000015	0.000000	0.000000	0.000000
2	0.141830	0.856831	0.001229	0.000080	0.000031
3	1.000000	0.000000	0.000000	0.000000	0.000000
4	0.999897	0.000085	0.000018	0.000000	0.000000
5	0.998895	0.001105	0.000000	0.000000	0.000000
6	0.000000	0.999247	0.000753	0.000000	0.000000
7	0.999892	0.000104	0.000004	0.000000	0.000000
8	0.737902	0.262075	0.000023	0.000000	0.000000
9	0.962433	0.037288	0.000279	0.000000	0.000000
10	0.931004	0.068844	0.000152	0.000000	0.000000
11	0.999999	0.000001	0.000000	0.000000	0.000000
12	0.999967	0.000033	0.000000	0.000000	0.000000
13	0.999930	0.000066	0.000003	0.000000	0.000000
14	0.899572	0.100346	0.000083	0.000000	0.000000
15	0.999275	0.000725	0.000000	0.000000	0.000000
16	0.032032	0.967263	0.000705	0.000000	0.000000
17	0.995229	0.004767	0.000001	0.000002	0.000001
18	0.965803	0.016605	0.000000	0.017592	0.000000
19	0.984703	0.015281	0.000016	0.000000	0.000000
20	0.999752	0.000248	0.000000	0.000000	0.000000
21	0.181756	0.818104	0.000077	0.000063	0.000000
22	0.999691	0.000308	0.000000	0.000000	0.000000
23	0.999973	0.000004	0.000023	0.000000	0.000000
24	0.999999	0.000001	0.000000	0.000000	0.000000
25	0.950224	0.049774	0.000003	0.000000	0.000000
26	0.999109	0.000724	0.000166	0.000001	0.000000
27	0.999998	0.000002	0.000000	0.000000	0.000000
28	0.997553	0.002434	0.000013	0.000000	0.000000
29	0.999955	0.000045	0.000000	0.000000	0.000000
30	0.999846	0.000005	0.000150	0.000000	0.000000

Table A.4 Random Power Profiles For Residential Berkeley

Appendix B. SIR Per Bit Thresholds for the Simulated Power Profiles

This appendix lists the E_b/I_0 thresholds simulated for the RAKE receiver with three combining fingers in the IS-95 BER performance model. The thresholds are the SIR requirements in order to maintain an average BER of 10^{-3} in the IS-95 downlink and uplink multipath Rayleigh faded channels for adequate digital communication quality. Each power profile contains three multipath signals with normalized power levels P_0 , P_1 and P_2 , and $P_0 + P_1 + P_2 = 1$. All combinations of the profiles with power levels being multiples of 0.02 are simulated, resulting in a total of 234 profiles.

Profile Index	P_0	P_1	P_2	Downlink E_b/I_0 Threshold (dB)	Uplink E_b/I_0 Threshold (dB)
1	1.00	0.00	0.00	5.68	3.90
2	0.98	0.02	0.00	5.52	3.99
3	0.96	0.04	0.00	5.46	4.08
4	0.96	0.02	0.02	5.36	4.07
5	0.94	0.06	0.00	5.28	4.16
6	0.94	0.04	0.02	5.26	4.16
7	0.92	0.08	0.00	5.16	4.26
8	0.92	0.06	0.02	5.16	4.25
9	0.92	0.04	0.04	5.13	4.26
10	0.90	0.10	0.00	5.08	4.36
11	0.90	0.08	0.02	5.06	4.35
12	0.90	0.06	0.04	5.05	4.35
13	0.88	0.12	0.00	5.00	4.43
14	0.88	0.10	0.02	4.96	4.44

Table B.1 E_b/I_0 Thresholds for the Simulated Power Profiles

Profile Index	P_0	P_1	P_2	Downlink E_b/I_0 Threshold (dB)	Uplink E_b/I_0 Threshold (dB)
15	0.88	0.08	0.04	4.95	4.45
16	0.88	0.06	0.06	4.96	4.45
17	0.86	0.14	0.00	4.93	4.53
18	0.86	0.12	0.02	4.89	4.54
19	0.86	0.10	0.04	4.89	4.54
20	0.86	0.08	0.06	4.87	4.54
21	0.84	0.16	0.00	4.86	4.60
22	0.84	0.14	0.02	4.82	4.63
23	0.84	0.12	0.04	4.81	4.63
24	0.84	0.10	0.06	4.79	4.63
25	0.84	0.08	0.08	4.80	4.64
26	0.82	0.18	0.00	4.78	4.68
27	0.82	0.16	0.02	4.77	4.70
28	0.82	0.14	0.04	4.73	4.72
29	0.82	0.12	0.06	4.73	4.73
30	0.82	0.10	0.08	4.72	4.75
31	0.80	0.20	0.00	4.73	4.75
32	0.80	0.18	0.02	4.73	4.78
33	0.80	0.16	0.04	4.67	4.81
34	0.80	0.14	0.06	4.66	4.84
35	0.80	0.12	0.08	4.64	4.83
36	0.80	0.10	0.10	4.65	4.85
37	0.78	0.22	0.00	4.70	4.81
38	0.78	0.20	0.02	4.65	4.85
39	0.78	0.18	0.04	4.62	4.88
40	0.78	0.16	0.06	4.60	4.91
41	0.78	0.14	0.08	4.58	4.92
42	0.78	0.12	0.10	4.59	4.94
43	0.76	0.24	0.00	4.65	4.88

Table B.1 E_b/I_0 Thresholds for the Simulated Power Profiles

Profile Index	P_0	P_1	P_2	Downlink E_b/I_0 Threshold (dB)	Uplink E_b/I_0 Threshold (dB)
44	0.76	0.22	0.02	4.59	4.93
45	0.76	0.20	0.04	4.59	4.96
46	0.76	0.18	0.06	4.55	4.98
47	0.76	0.16	0.08	4.53	5.02
48	0.76	0.14	0.10	4.53	5.02
49	0.76	0.12	0.12	4.53	5.03
50	0.74	0.26	0.00	4.60	4.93
51	0.74	0.24	0.02	4.58	4.98
52	0.74	0.22	0.04	4.53	5.02
53	0.74	0.20	0.06	4.52	5.06
54	0.74	0.18	0.08	4.49	5.10
55	0.74	0.16	0.10	4.46	5.13
56	0.74	0.14	0.12	4.49	5.14
57	0.72	0.28	0.00	4.57	4.98
58	0.72	0.26	0.02	4.52	5.03
59	0.72	0.24	0.04	4.48	5.08
60	0.72	0.22	0.06	4.46	5.12
61	0.72	0.20	0.08	4.46	5.16
62	0.72	0.18	0.10	4.43	5.20
63	0.72	0.16	0.12	4.42	5.22
64	0.72	0.14	0.14	4.42	5.22
65	0.70	0.30	0.00	4.53	5.02
66	0.70	0.28	0.02	4.49	5.08
67	0.70	0.26	0.04	4.46	5.13
68	0.70	0.24	0.06	4.44	5.19
69	0.70	0.22	0.08	4.40	5.24
70	0.70	0.20	0.10	4.40	5.27
71	0.70	0.18	0.12	4.37	5.30
72	0.70	0.16	0.14	4.39	5.31

Table B.1 E_b/I_0 Thresholds for the Simulated Power Profiles

Profile Index	P_0	P_1	P_2	Downlink E_b/I_0 Threshold (dB)	Uplink E_b/I_0 Threshold (dB)
73	0.68	0.32	0.00	4.51	5.06
74	0.68	0.30	0.02	4.47	5.12
75	0.68	0.28	0.04	4.42	5.18
76	0.68	0.26	0.06	4.39	5.24
77	0.68	0.24	0.08	4.38	5.30
78	0.68	0.22	0.10	4.34	5.33
79	0.68	0.20	0.12	4.33	5.37
80	0.68	0.18	0.14	4.34	5.40
81	0.68	0.16	0.16	4.34	5.40
82	0.66	0.34	0.00	4.49	5.09
83	0.66	0.32	0.02	4.45	5.15
84	0.66	0.30	0.04	4.40	5.23
85	0.66	0.28	0.06	4.36	5.28
86	0.66	0.26	0.08	4.34	5.34
87	0.66	0.24	0.10	4.33	5.39
88	0.66	0.22	0.12	4.30	5.43
89	0.66	0.20	0.14	4.29	5.47
90	0.66	0.18	0.16	4.29	5.48
91	0.64	0.36	0.00	4.47	5.12
92	0.64	0.34	0.02	4.42	5.19
93	0.64	0.32	0.04	4.38	5.26
94	0.64	0.30	0.06	4.37	5.33
95	0.64	0.28	0.08	4.32	5.39
96	0.64	0.26	0.10	4.28	5.45
97	0.64	0.24	0.12	4.27	5.49
98	0.64	0.22	0.14	4.27	5.53
99	0.64	0.20	0.16	4.25	5.55
100	0.64	0.18	0.18	4.26	5.56
101	0.62	0.38	0.00	4.44	5.15

Table B.1 E_b/I_0 Thresholds for the Simulated Power Profiles

Profile Index	P_0	P_1	P_2	Downlink E_b/I_0 Threshold (dB)	Uplink E_b/I_0 Threshold (dB)
102	0.62	0.36	0.02	4.38	5.22
103	0.62	0.34	0.04	4.36	5.29
104	0.62	0.32	0.06	4.32	5.36
105	0.62	0.30	0.08	4.29	5.43
106	0.62	0.28	0.10	4.26	5.49
107	0.62	0.26	0.12	4.25	5.55
108	0.62	0.24	0.14	4.23	5.59
109	0.62	0.22	0.16	4.23	5.62
110	0.62	0.20	0.18	4.21	5.64
111	0.60	0.40	0.00	4.42	5.16
112	0.60	0.38	0.02	4.37	5.24
113	0.60	0.36	0.04	4.35	5.32
114	0.60	0.34	0.06	4.31	5.39
115	0.60	0.32	0.08	4.26	5.46
116	0.60	0.30	0.10	4.26	5.54
117	0.60	0.28	0.12	4.21	5.59
118	0.60	0.26	0.14	4.21	5.63
119	0.60	0.24	0.16	4.18	5.68
120	0.60	0.22	0.18	4.17	5.70
121	0.60	0.20	0.20	4.19	5.71
122	0.58	0.42	0.00	4.43	5.17
123	0.58	0.40	0.02	4.36	5.25
124	0.58	0.38	0.04	4.31	5.34
125	0.58	0.36	0.06	4.29	5.41
126	0.58	0.34	0.08	4.24	5.49
127	0.58	0.32	0.10	4.22	5.57
128	0.58	0.30	0.12	4.19	5.62
129	0.58	0.28	0.14	4.17	5.68
130	0.58	0.26	0.16	4.17	5.73

Table B.1 E_b/I_0 Thresholds for the Simulated Power Profiles

Profile Index	P_0	P_1	P_2	Downlink E_b/I_0 Threshold (dB)	Uplink E_b/I_0 Threshold (dB)
131	0.58	0.24	0.18	4.16	5.76
132	0.58	0.22	0.20	4.16	5.77
133	0.56	0.44	0.00	4.42	5.19
134	0.56	0.42	0.02	4.35	5.27
135	0.56	0.40	0.04	4.33	5.35
136	0.56	0.38	0.06	4.27	5.43
137	0.56	0.36	0.08	4.24	5.52
138	0.56	0.34	0.10	4.20	5.59
139	0.56	0.32	0.12	4.18	5.66
140	0.56	0.30	0.14	4.16	5.72
141	0.56	0.28	0.16	4.14	5.76
142	0.56	0.26	0.18	4.14	5.80
143	0.56	0.24	0.20	4.12	5.82
144	0.56	0.22	0.22	4.13	5.83
145	0.54	0.46	0.00	4.38	5.19
146	0.54	0.44	0.02	4.35	5.28
147	0.54	0.42	0.04	4.29	5.37
148	0.54	0.40	0.06	4.25	5.45
149	0.54	0.38	0.08	4.22	5.53
150	0.54	0.36	0.10	4.19	5.61
151	0.54	0.34	0.12	4.18	5.68
152	0.54	0.32	0.14	4.15	5.75
153	0.54	0.30	0.16	4.12	5.80
154	0.54	0.28	0.18	4.13	5.85
155	0.54	0.26	0.20	4.11	5.87
156	0.54	0.24	0.22	4.12	5.89
157	0.52	0.48	0.00	4.39	5.20
158	0.52	0.46	0.02	4.34	5.29
159	0.52	0.44	0.04	4.30	5.37

Table B.1 E_b/I_0 Thresholds for the Simulated Power Profiles

Profile Index	P_0	P_1	P_2	Downlink E_b/I_0 Threshold (dB)	Uplink E_b/I_0 Threshold (dB)
160	0.52	0.42	0.06	4.24	5.46
161	0.52	0.40	0.08	4.21	5.54
162	0.52	0.38	0.10	4.17	5.63
163	0.52	0.36	0.12	4.15	5.70
164	0.52	0.34	0.14	4.16	5.78
165	0.52	0.32	0.16	4.12	5.82
166	0.52	0.30	0.18	4.12	5.88
167	0.52	0.28	0.20	4.09	5.91
168	0.52	0.26	0.22	4.09	5.93
169	0.52	0.24	0.24	4.08	5.94
170	0.50	0.50	0.00	4.39	5.21
171	0.50	0.48	0.02	4.34	5.29
172	0.50	0.46	0.04	4.27	5.38
173	0.50	0.44	0.06	4.24	5.46
174	0.50	0.42	0.08	4.20	5.55
175	0.50	0.40	0.10	4.16	5.64
176	0.50	0.38	0.12	4.15	5.71
177	0.50	0.36	0.14	4.13	5.79
178	0.50	0.34	0.16	4.09	5.85
179	0.50	0.32	0.18	4.09	5.90
180	0.50	0.30	0.20	4.07	5.94
181	0.50	0.28	0.22	4.07	5.97
182	0.50	0.26	0.24	4.07	5.98
183	0.48	0.48	0.04	4.28	5.38
184	0.48	0.46	0.06	4.23	5.47
185	0.48	0.44	0.08	4.20	5.56
186	0.48	0.42	0.10	4.17	5.64
187	0.48	0.40	0.12	4.13	5.73
188	0.48	0.38	0.14	4.11	5.80

Table B.1 E_b/I_0 Thresholds for the Simulated Power Profiles

Profile Index	P_0	P_1	P_2	Downlink E_b/I_0 Threshold (dB)	Uplink E_b/I_0 Threshold (dB)
189	0.48	0.36	0.16	4.09	5.86
190	0.48	0.34	0.18	4.07	5.92
191	0.48	0.32	0.20	4.07	5.96
192	0.48	0.30	0.22	4.05	5.99
193	0.48	0.28	0.24	4.05	6.02
194	0.48	0.26	0.26	4.06	6.02
195	0.46	0.46	0.08	4.21	5.55
196	0.46	0.44	0.10	4.16	5.65
197	0.46	0.42	0.12	4.14	5.74
198	0.46	0.40	0.14	4.11	5.81
199	0.46	0.38	0.16	4.07	5.88
200	0.46	0.36	0.18	4.06	5.93
201	0.46	0.34	0.20	4.06	5.98
202	0.46	0.32	0.22	4.05	6.02
203	0.46	0.30	0.24	4.04	6.05
204	0.46	0.28	0.26	4.02	6.06
205	0.44	0.44	0.12	4.14	5.75
206	0.44	0.42	0.14	4.12	5.81
207	0.44	0.40	0.16	4.08	5.89
208	0.44	0.38	0.18	4.07	5.95
209	0.44	0.36	0.20	4.04	6.00
210	0.44	0.34	0.22	4.02	6.04
211	0.44	0.32	0.24	4.03	6.07
212	0.44	0.30	0.26	4.03	6.08
213	0.44	0.28	0.28	4.02	6.09
214	0.42	0.42	0.16	4.08	5.89
215	0.42	0.40	0.18	4.05	5.96
216	0.42	0.38	0.20	4.05	6.01
217	0.42	0.36	0.22	4.02	6.05

Table B.1 E_b/I_0 Thresholds for the Simulated Power Profiles

Profile Index	P_0	P_1	P_2	Downlink E_b/I_0 Threshold (dB)	Uplink E_b/I_0 Threshold (dB)
218	0.42	0.34	0.24	4.00	6.09
219	0.42	0.32	0.26	4.01	6.11
220	0.42	0.30	0.28	4.00	6.12
221	0.40	0.40	0.20	4.05	6.01
222	0.40	0.38	0.22	4.02	6.06
223	0.40	0.36	0.24	4.02	6.09
224	0.40	0.34	0.26	3.99	6.12
225	0.40	0.32	0.28	4.00	6.13
226	0.40	0.30	0.30	3.98	6.14
227	0.38	0.38	0.24	4.01	6.10
228	0.38	0.36	0.26	3.99	6.13
229	0.38	0.34	0.28	4.00	6.14
230	0.38	0.32	0.30	4.00	6.16
231	0.36	0.36	0.28	4.00	6.14
232	0.36	0.34	0.30	3.99	6.16
233	0.36	0.32	0.32	3.99	6.17
234	0.34	0.34	0.32	3.97	6.17

Table B.1 E_b/I_0 Thresholds for the Simulated Power Profiles